Development and Implementation of Quadratically Distorted (QD) Grating and Grisms System for 4D Multi-Colour Microscopy Imaging (MCMI)

Yan Feng

A dissertation submitted for the degree of Doctor of Philosophy

Heriot-Watt University

School of Engineering and Physical Sciences

October 2016

Abstract

The recent emergence of super-resolution microscopy imaging techniques has surpassed the diffraction limit to improve image resolution. Contrary to the breakthroughs of spatial resolution, high temporal resolution remains a challenge. This dissertation demonstrates a simple, on axis, 4D (3D + time) multi-colour microscopy imaging (MCMI) technology that delivers simultaneous 3D broadband imaging over cellular volumes, which is especially applicable to the real-time imaging of fast moving biospecimens. Quadratically distorted (QD) grating, in the form of an off axis-Fresnel zone plate, images multiple object planes simultaneously on a single image plane. A delicate mathematical model of 2D QD grating has been established and implemented in the design and optimization of QD grating. Grism, a blazed grating and prism combination, achieves chromatic control in the 4D multi-plane imaging. A pair of grisms, whose separation can be varied, provide a collimated beam with a tuneable chromatic shear from a collimated polychromatic input. The optical system based on QD grating and grisms has been simply appended to the camera port of a commercial microscope, and a few bioimaging tests have been performed, i.e. the 4D chromatically corrected imaging of fluorescence microspheres, MCF-7 and HeLa cells. Further investigation of bioimaging problems is still in progress.

Acknowledgements

First and foremost, I would like to express my great appreciation to the PhD project itself, which is the most beautiful work I have ever met and constantly offers me confidence, perseverance and courage.

My deepest gratitude goes to the three supervisors during my PhD period. Prof. Alan Greenaway led me to a new earth of optics, shared his brilliant ideas and inspired me to catch up with brain storms. Deeply influenced by Alan, I love my current work so much and will endeavour to promote it in the future. Prof. Will Shu took over the supervision after Alan's retirement in July 2014. I am very thankful to have Will's kind consideration and nice help; otherwise I would have failed to complete this dissertation. Prof. Jiaru Chu of University of Science and Technology of China showed me how fantastic the scientific work is as well as how to behave as a qualified researcher. With Jiaru's endless support, I obtained my first PhD degree in 'Precision Instruments and Machinery' in 2013.

A pretty special thank must be delivered to Prof. Xiaohong Fang of Institute of Chemistry, Chinese Academy of Sciences, for her generous funding and elaborate guidance on bioimaging during my postdoctoral period from November 2013 to July 2016, with which I get the opportunity to restart my work and make 'unrealistic' things come true.

I would give appreciations to my friends, colleagues and collaborators, especially Ms. Ying Liu for her emotional support, Dr. Yuewei Liu for his collaboration in mathematical modelling, and Dr. Zhengkun Liu for the fabrication of key optical elements.

My sincere thanks also go to Scottish Universities Physics Alliance (SUPA), Overseas Research Students Awards Scheme (ORSAS) and China Scholarship Council (CSC) for their financial support throughout my two PhD courses.

Finally and ultimately I acknowledge my parents and sister for their constant love and support.

Table of Contents

Contents

Lists of Tables and Figures

List of Publications by the Candidate

Journal Papers:

[1] **Y. Feng**, L. Scholz, D. Lee, H. Dalgarno, D. Foo, L. Yang, W. Lu and A. Greenaway, Multi-mode microscopy using diffractive optical elements. *Engineering Review* **31**(2), 133-139 (2011).

[2] **Y. Feng**, P. A. Dalgarno, D. Lee, Y. Yang, R. R. Thomson and A. H. Greenaway, Chromatically-corrected, high-efficiency, multi-colour, multi-plane 3D imaging. *Optics Express* **20**(18), 20705-20714 (2012).

Patent:

Y. Feng, P. A. Dalgarno, D. Lee, A. H. Greenaway, Y. Yang and R. R. Thomson, Optical system. *UK Intellectual Property Office*. UK Patent Application No. GB2504188-A, (Marks & Clerk LLP Edinburgh Office, United Kingdom, 2013).

Ph.D. Dissertation:

Y. Feng, Optimization of phase gratings with applications to 3D microscopy imaging, A dissertation for the degree of Doctor of Philosophy, Precision Instruments and Machinery, University of Science and Technology of China, Hefei, China (2013).

Chapter 1

Introduction

Preface

Currently super-resolution optical microscopy imaging techniques focus primarily on breaking the limit of spatial resolution, and there is comparatively little work on the improvement of temporal resolution. In this dissertation we develop a novel approach to a high temporal resolution technique by simultaneous multi-plane, multi-colour imaging based on commercial optical microscopes and standard camera systems, which we refer to as '4D multi-colour microscopy imaging (MCMI)'. This chapter begins with an outline of super-resolution optical microscopy and basic principles of diffraction grating. Followed by this background information, we show a short history of our quadratically distorted (QD) grating based 4D imaging technique and some similar methods which may obtain comparable 4D bioimages. Finally the content of this dissertation is briefly interpreted.

1.1 Super-resolution optical microscopy

1.1.1 Spatial resolution limit and super-resolution imaging

The optical microscope has become a ubiquitous tool in biological research, which utilizes visible light and a set of lenses to magnify images of biospecimen. Since the 17th century, bioimaging microscopy has undergone significant advances in improving sample resolution. Using the visible light, however, we can hardly observe sub-wavelength structures with these optical microscopes due to the *Abbe diffraction limit* [1]. Let a light beam with wavelength λ travel in a medium with refractive index n and converge to a spot with angle α, then a spot with radius $d_{xy} = \frac{\lambda}{2NA}$ will occur, where $NA = n\sin\alpha$ represents the *numerical aperture* and can reach about 1.4~1.6 in modern optics. And the axial resolution $d_z = \frac{2\lambda}{NA^2}$ is lower due to geometry. Accordingly, structures as small as ~200nm can be resolved laterally (in the *xy*-plane) and ~500nm axially (in the *z* direction).

Over the past few decades, the optical imaging techniques have been developed to provide unprecedented spatial resolution beyond the diffraction limit. The Nobel Prize in Chemistry of 2014 was awarded to Eric Betzig [2], William Moerner [3] and Stefan Hell [4] for the development of super-resolution fluorescence microscopy [5] which brings optical microscopy into the nanodimension. Some well-established super-resolution fluorescence microscopy techniques, *stimulated emission depletion (STED)* [6-8] which enhances the resolution by selectively deactivating some fluorophores and thus minimise the area of illumination at the focal point, *(fluorescence) photo activated localization microscopy (fPALM/PALM)* [2, 9] which utilizes sequential activation and time-resolved localization of photoswitchable fluorophores to create high resolution images, and *saturated structured illumination microscopy (SSIM)* [10-12] which improves spatial resolution by collecting information from frequency space using very photostable fluorophores, are in principle capable of a few nanometers spatial resolution. A typical true subwavelength imaging technology, *near-field scanning optical microscopy (NSOM)*, exploits the properties of evanescent waves and has demonstrated the lateral resolution of 20nm and vertical resolution of 2~5nm [13, 14].

1.1.2 High temporal resolution imaging techniques

Although these microscopy techniques have achieved considerable high spatial resolution, the images are taken from one focal plane which is 2-dimensional (2D). However, biological samples, i.e. living cells, are three-dimensional (3D) and constantly changing, there has been an increased demand for imaging tools that can be used for analysing volume structures. Most of current 3D microscopy techniques rely on time-consuming methods by scanning the depth of a sample, leading to severe limitations for optically sensitive samples and good understanding of biosamples dynamics. Therefore new temporal resolution imaging techniques are required in order to record 3D dynamics in high temporal frame rates.

Two of current 3D optical imaging techniques are *confocal laser scanning microscopy (CLSM or LSCM)* and *wide-field imaging* [15]. Like a process known as *optical sectioning* [16], in CLSM a specimen is illuminated by a point laser source and the 3D imaging is achieved by scanning the laser spot, which gives excellent sectioning properties by obstructing out-of-focus light but the mechanical scanning operation is often time consuming thus limiting the imaging speed and making in vivo imaging difficult [17]. A successful CLSM product, Olympus FV3000, can support the so-called

live cell 2D-6D (x,y,λ,z,t,p) imaging and snapshot calcium sparks and waves at speeds up to 438 frames per second in a restrictive field of view. But its scanning speed will be much lower when examining volume structure in a reasonable large field of view, which could hardly record fast-changing process [18]. Wide-field microscopy uses diffraction, reflection, or refraction of radiation incident upon the sample with the subsequent collection of this scattered radiation to build up an image, which provides real-time 2D imaging but z-scanning or holographic imaging may be required for constructing 3D images through complicated data analysis [19, 20]. Although modern microscopy benefits a lot from the development of high-sensitivity array detectors, the limitations above make it difficult to image relatively rapid intracellular trafficking processes that might be of central interest to biologists and clinicians.

A commercial simultaneous 3D imaging product, InSight3D of PhaseView [21], enables real-time 3D acquisition using a scanless method based on microlens array. But this lenslet system may introduce a few inherent optical aberrations and the imaging processing software could be considerable complicated, thus may hinder the versatile applications under different imaging conditions.

We have seen that the conflict between spatial and temporal resolution always exists, especially when the biosample moves so fast that only one exposure could be recorded at each time point and thus a 3D focal stack can hardly be created in the classical manner. To achieve higher spatiotemporal resolution, a few 3D imaging techniques, including the so-called *multifocal plane microscopy (MUM)* [22] and *light-sheet microscopy (LSM)* [23], have been developed. MUM allows simultaneous imaging of different focal planes within the specimen, and the simplest setup can be formed by placing one or several dichroic mirrors in the infinity-beam of the light path to separate the sample emission light onto different cameras or different parts of the same camera chip [24]. Take a recent case for example, MUM enables rapid 3D tracking of several molecules at the same time across a depth of 10 μm as well as multicolor imaging, which has played a significant role in exploring the 3D trafficking pathways in epithelial cell barriers [25]. However, as Fig. 1.1 shown, the fluorescence light emitted from the specimen is equally split into many 50:50 beams by a set of beam splitters [25], so that substantial luminous flux might be lost and rigorous calibration is required for the (a bit) unwieldy optical layout. The traditional multiple light-sheets microscope unfolds the beam path and creates multiple copies of Gaussian beams using the

diffraction grating and the cylindrical lens [26], which allows simultaneous illumination of multiple specimen planes. But the narrowband imaging properties and the non-uniform energy distribution in each light sheet may restrict practical application(s) in 3D bioimaging especially when the light power is insufficient to avoid bleaching, cell damage and other problems induced by over-exposure.

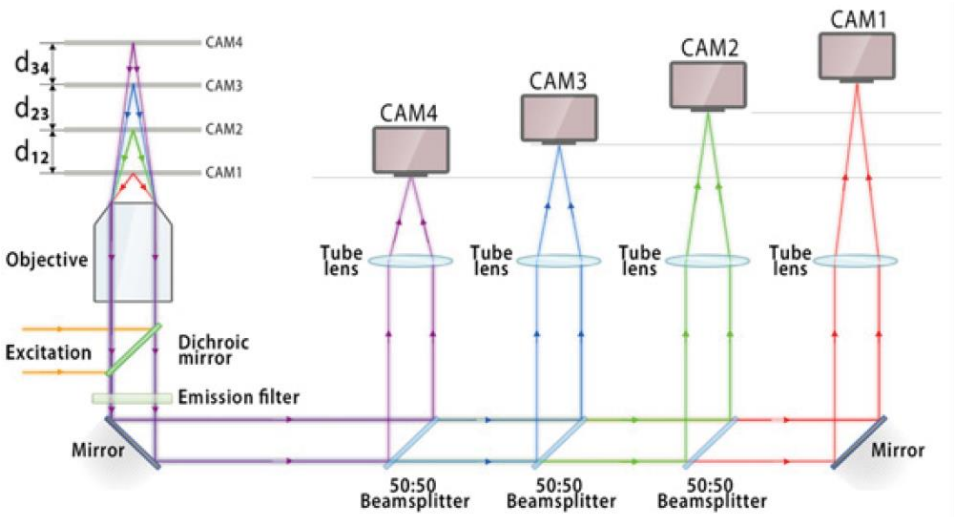

Fig. 1.1 The schematic optical layout of multifocal plane microscopy (MUM) [25].

Real-time 3D (thus 4D) optical imaging technique, which can yield a 4D image of the continuously changing cell, is distinct among 3D imaging tools in its ability to record in vivo dynamics of living cell. In this dissertation, we will demonstrate 4D multi-colour microscopy imaging (4D MCMI) in the context of biological fluorescence microscopy. Our relay system consisting of a quadratically distorted (QD) diffraction grating and lens can be simply attached to the camera port of microscope [27, 28]. In addition, a pair of grisms (a grating combined with a prism) are applied for correcting the chromatic smearing induced by the non-zero diffraction orders of QD grating [29, 30]. Such an approach offers all of the advantages of multi-plane imaging performed by beam splitters and multiple light-sheets with the additional advantages of simplicity, low cost and full compatibility with commercial microscopes.

1.2 Basic principles of the diffraction grating and its applications in imaging

The diffractive optical element (DOE), which behaves as an optical signal converter such as diffraction grating, beam splitter, focusing device, diffuser, special filter and so on, is designed based on the efficient use of the diffraction phenomenon for imposing on an incident wave a functional variation of amplitude or phase, or both. Being

constructed from specially designed micro-structure patterns, DOE may enable the light manipulation to almost any desired profile by means of altering the phase of input beam. Of our particular interest is the transmission diffraction grating, which is, in the simplest and practical form, a set of slits distributed in accordance with a specific law on an optically transparent substrate. Take a one-dimensional binary phase grating illuminated by a monochromatic scalar light wave for example, it may be characterized by its transmission function in the complex form [31],

$$F(x) = e^{i\phi(x)} \tag{1.1}$$

where the phase $\phi(x)$ is a real periodic function, whose period (say d) is equal to the period of the grating.

Proceeding now with the theory of the diffraction grating on the basis of the derivations of *'Born and Wolf'* [31], we consider a grating consisting of a succession of long equidistant slits, in which two corresponding points A and B locate in arbitrary neighbouring slits, to explore the significance of the phase difference and its underlying principles, as Fig. 1.2 shown.

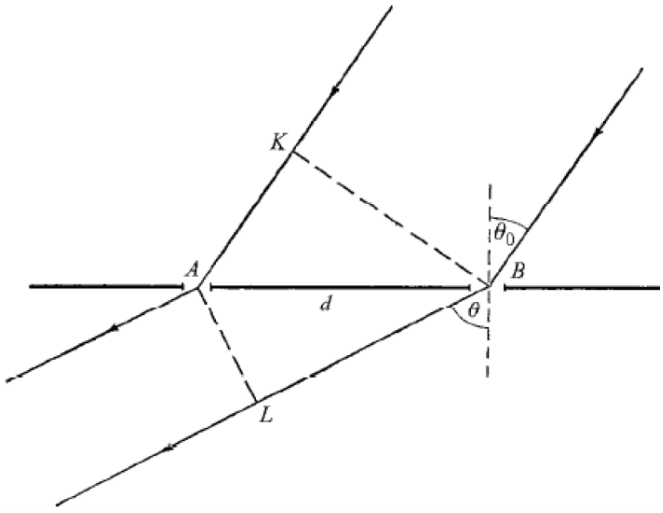

Fig. 1.2 Illustrating the theory of the diffraction grating [31].

From the geometry in Fig. 1.2 we find that the total path difference between light arriving at the distant point of observation from corresponding points in two neighbouring slits is,

$$BL - AK = d(\sin\theta - \sin\theta_0) = dp \tag{1.2}$$

where *K* and *L* denote the foots of the perpendicular from *B* on to the ray incident at *A* and from *A* on to the ray diffracted at *B* in the direction θ, respectively; θ_0 and θ are the angles of incidence and diffraction measured from the normal to the grating outer face, respectively; *d* is the period of grating and *p* is set to be $(\sin\theta - \sin\theta_0)$.

Hence the corresponding phase difference is given by,

$$\frac{2\pi dp}{\lambda} = kdp \tag{1.3}$$

where $k = \frac{2\pi}{\lambda}$ is termed the *wave number* and λ the incident wavelength.

From the principles of *Fraunhofer diffraction* the normalized intensity function of a grating consisting of *N* similar equidistant parallel slits may be written as [31],

$$\frac{1}{N^2} I(p) = \left[\frac{\sin(Nkdp/2)}{N\sin(kdp/2)} \right]^2 \left[\frac{\sin(ksp/2)}{ksp/2} \right]^2 \tag{1.4}$$

where *s* is the width of each slit.

Eq. (1.4) appears in the form of the product of two factors. The first factor is the normalized interference function which indicates the effect of interference of light from different periods. We see that this function has maxima at all points where the denominator $N^2 \sin^2(kdp/2)$ vanishes, i.e. where $kdp/2$ is zero or an integral multiple of π, and these maxima are separated by points of zero intensity at $kdp/2 = \pm n\pi/N$ (the case where n/N is an integer being excluded). And the second factor is the normalized intensity function of a single slit which represents the effect of a single period of the grating and depends on the form of the slits. Suppose that this function has a principal maximum for some direction and that on both sides of the maximum it falls off slowly in comparison with the interference function. Then $I(p)$ will have the general form of the first factor, but will be 'modulated' by the second one. In conclusion, $I(p)$ will still have fairly sharp maxima when,

$$p = \sin\theta - \sin\theta_0 = \frac{m\lambda}{d} \qquad (m = 0, \pm 1, \pm 2, ...) \tag{1.5}$$

which is the well-known *grating equation*. In this dissertation we call the integer *m* the *order of diffraction*, which represents the path difference in wavelengths between light diffracted in the direction of the maximum, from corresponding points in two neighbouring slits. A negative sign of θ_o might be set when a reflection grating is applied. Furthermore, most of the light may be directed into one particular order (usually lower orders such as the first or second) if a *blazed angle* is introduced to each slit, which is the so-called *blazed grating*.

By now we have modelled one-dimensional gratings, and the analysis may be extended to two- and three-dimensional periodic arrangements of diffracting bodies. Seen from Eq. (1.5), the diffraction directions (except for *m*=0) is dependent on the period of grating and the incident wavelength, so that the grating will decompose a beam of polychromatic incident light into spectral orders. Consequently, acting as the dispersive elements, the diffraction gratings are commonly used in spectrometers and monochromators.

However, it is more than just obtaining a separated monochromatic spectrum in practical applications. Nowadays the diffraction grating (or say DOE) has come to be used in a wider sense, i.e. formation of laser beam(s) for specific optical manipulation [32-34]. Let us take a recent successful application for example. The *lattice light sheet microscopy* developed by Eric Betzig's group of Howard Hughes Medical Institute, USA, is a novel combination of techniques from *light sheet fluorescence microscopy* [23, 35-37], *Bessel beam microscopy* [32] and *structured illumination microscopy (SIM)* [11, 38, 39], in which, as illustrated in Fig. 1.3, a linearly polarized circular input beam is processed to a thin sheet of light using two pairs of cylindrical lenses (in the *x* and *z* directions respectively) successively, a binary ferroelectric spatial light modulator (SLM) then modulates the wavefront of this light, and an opaque mask containing a transparent annulus filters out unwanted diffraction orders and enforces maximum and minimum NA of illumination that dictate the *y* extent of the eventual lattice light sheet [40]. Here the lattice light sheet introduced by the transparent annular ring is two or three dimensional interference pattern.

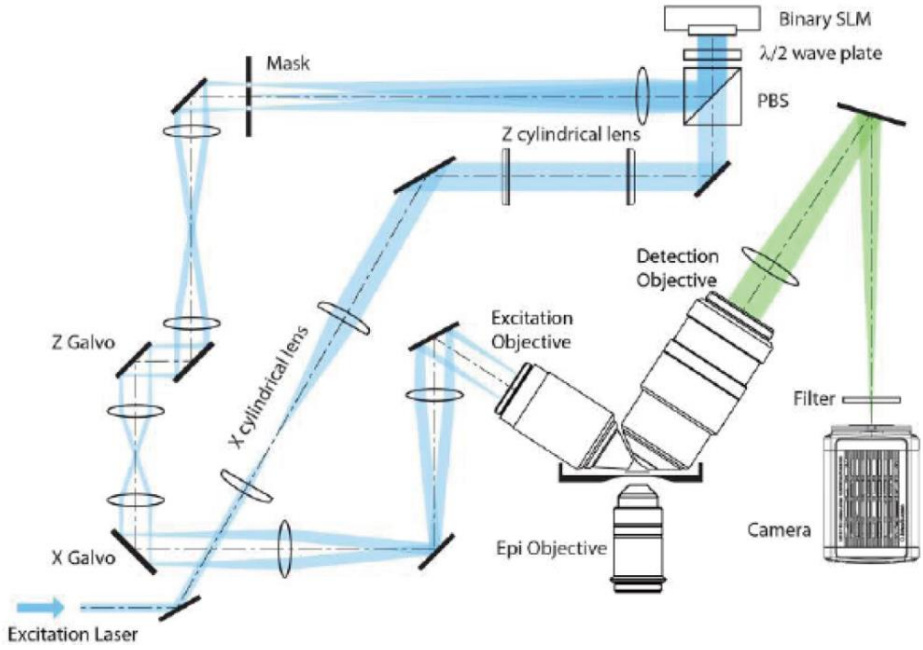

Fig. 1.3 Schematic of the optical path of the lattice light sheet microscope [40].

At this stage we concentrate more on the function of the SLM and the mask rather than the overall principles of the microscopy. In our point of view, these optical elements may be regarded as the specially designed gratings, which indicate that the diffractive optical element (thus customized grating) is also versatile in the optical modulation of the light field and has vast potential for further applications in imaging technology. In this dissertation we will demonstrate a so-called 'quadratically distorted (QD) grating' comprising of a series of concentric arcs with varying radii, which (de)focuses light using diffraction instead of refraction for 4D microscopy imaging.

1.3 4D imaging: from astronomy to bioimaging

Images of stars, planets and other astronomical objects are now routinely sharpened using 'adaptive optics' (AO) [41] techniques that remove the distorting effect of the Earth's atmosphere [42]. Borrowing various principles from AO, My PhD supervisor Alan H. Greenaway (who has retired in July, 2014) and his colleague Paul M. Blanchard developed a novel 4D imaging technique based on the QD grating in the mid-1990s, which was originally designed for photonic-crystal-fibre strain sensors (funded by the UK Ministry of Defence) and could be used in astronomy (funded by the Science and Technology Facilities Council) [27, 28, 43-45]. By introducing a detour phase term, the QD grating imparts an equal but opposing focal power in the positive and negative diffracted orders [28, 46]. When combined with a lens, such a QD grating provides simultaneous multi-plane imaging: i.e. the ability simultaneously to image

different object planes on a single camera. All in one go, this imaging technique provides a simple, versatile avenue for implementing different imaging modes in optical imaging systems from astronomy to cellular biology. *Strange as it may seem, the very same gratings and mirrors that are used in telescopes to correct for the effects of turbulence can also be used to image biological samples [42]*. My former group had developed such a QD grating based device using commercial optical components which can be simply bolted on to a conventional microscope to allow cells to be investigated in 4D. One of the applications is the exploration of male infertility problems by examining the 4D dynamics of sperm tails, which was in collaboration with Jackson Kirkman-Brown of Womens' NHT Foundation Trust and colleagues of Birmingham University. Part of a single frame from a movie of swimming human sperms [47] is shown in Fig. 1.4, in which the three images represent a single sperm cell focused at different depths (the separation of these in-focus planes is 14.6μm).

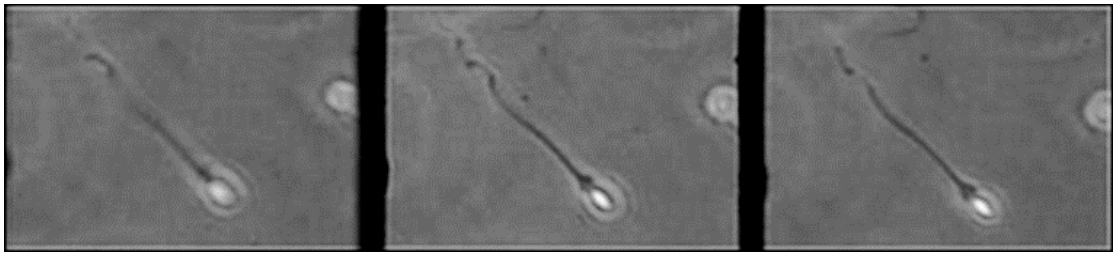

Fig. 1.4 4D phase contrast imaging of a swimming human sperm.

A QD grating, which is made by etching slits into a thin fused-silica substrate with a fraction of a wavelength deep, brings the three object planes simultaneously into focus on the same image plane. From Fig. 1.4 the biologist may find spatial localizations of both the sperm's head and tail according to their focus conditions shown in each image. Since conventional imaging methods would capture only one of these images, our technique offers new insights into sperm dynamics that could help bioscientists to screen new drugs to improve fertility. In conclusion, our QD grating based imaging technique has direct applications for studies of rapidly-changing objects in cell-biology (e.g. organelle and flagella dynamics), fluid-flow and high-speed, 3D tracking, and many imaging modes can be realised with a simple optical attachment fully compatible with commercial microscopes and standard camera systems [48].

More recently a different implementation of similar principles has been investigated by Sara Abrahamsson and her colleagues [49]. Named as the *aberration-corrected*

multifocus microscopy (MFM), it is capable of producing an instant focal stack of nine 2D images in multiple colours [49], and can be extended to image up to 25 focal planes under some circumstance [50]. As illustrated in Fig. 1.5, the key optical elements of the imaging system should be the multifocus grating (MFG) and the combination of chromatic correction grating (CCG) and prism, which are utilized to provide a variety of focal lengths (like QD grating) and correct chromatic smearing introduced by the MFG (like our grism which will be demonstrated in Chapter 4), respectively.

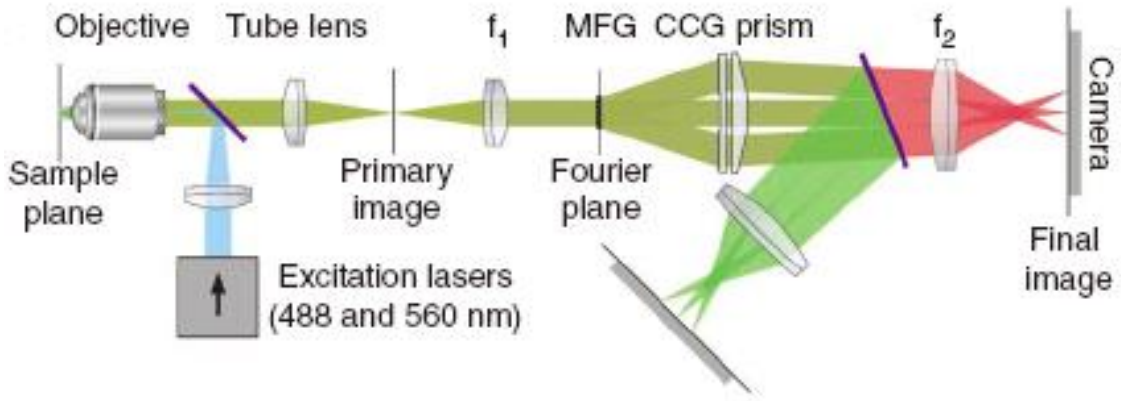

Fig. 1.5 Schematic of the optical path of the aberration-corrected multifocus microscopy (MFM) when the optical elements are appended to a wide-field fluorescence microscope [49].

It is definitely a really-swish system, boxed and with simple controls, and has been successfully applied in a few biological explorations [51, 52]. However, since the MFG patterns are calculated by the Matlab fft2 function [49], we may conclude that the design and optimization of both MFG and the imaging system are performed in an unknown 'black box' based on computer programming. It can be seen from Fig. 1.6 that the MFG patterns are very specially figured out and this unique design may only be appropriate for limited applications, thus hindering its practical usefulness.

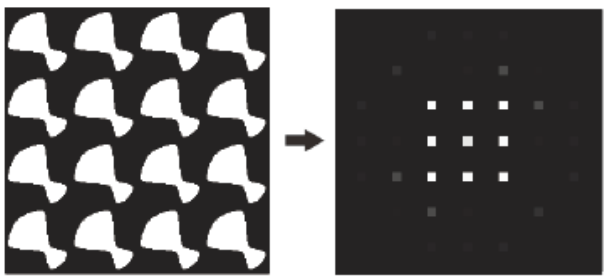

Fig. 1.6 The MFG grating function pattern (left) and the corresponding energy distribution (right) [49].

With increasingly breakthroughs in biological microscopy imaging, it is particularly important to analytically and systematically develop an imaging technique based on physics principles. In this dissertation we will endeavour to explore the content of the 'black box', i.e. fundamental optical principles of the QD grating and the design and application of our 4D MCMI technique. Distinct from Sara's specific design [49], our 4D MCMI system could be adjusted to meet versatile requirements, such as variable separations between focused planes and comparable broad bandwidth of incident light. We can also design/adjust the etch depth of QD grating to achieve balanced energy of the first three diffraction orders.

1.4 Dissertation overview

The main objective of this work is to develop a scanless 4D multi-colour microscopy imaging (4D MCMI) technique to improve the temporal resolution without compromising spatial resolution of microscopes. In this dissertation we represent a microscope attachment which can simultaneously record images from several object planes. By introducing a quadratically distorted (QD) diffraction grating into the optical system, an order-dependent focussing power is established in order to generate several (2~9) images, each arising from a different object plane. A pair of grisms is also applied for the correction of chromatic aberration induced by QD grating. This 4D MCMI technique is exploited for real-time 3D bioimaging, especially for the imaging of live cells which are constantly changing.

Chapter 2 reviews the background of the QD grating based 4D imaging technique, including both the basic principles developed by Paul Blanchard and Alan Greenaway [28], and some primary work about optical efficiency and error budget which has been submitted in my first PhD dissertation but link to the work of this dissertation [47]. Then a few problems are addressed, such as the rough 1D mathematical model of QD grating and the inherent chromatic smearing of non-zero diffraction orders, for further investigation.

Based on the *Fraunhofer diffraction theory* [31], Chapter 3 covers the definition, deviation, numerical calculation and final verifications of an elaborate mathematical model of QD grating. The numerical solution of *Fourier spectra* [53], thus the 'working phase' of QD grating [48, 54], can be straightforwardly regarded as the fabrication guide in etch depth.

To correct the chromatic aberration induced by grating, Chapter 4 considers the chromatic control of QD grating based 4D imaging system. Utilizing the combination of QD grating, a pair of grisms and a conventional microscope (Olympus IX73 in our case), chromatically-corrected and high-efficiency 4D MCMI could be achieved. A few simulated eGFP fluorophore imaging tests are also demonstrated to compare the chromatic smearing with and without grisms correction.

Since the problems proposed in Chapter 2 have been solved in Chapter 3 and Chapter 4 respectively, attention is turned to the practical applications in Chapter 5 — 4D biological microscopy imaging. The bioimaging tests start off with the basic fluorescence microspheres imaging and then applied the same experimental setup in live cell imaging, where MCF-7 and HeLa cells have been used as initial trials. Biological process, such as TGF β II containing vesicles in living cells, has been a popular topic of biochemists, and we are endeavouring to 'see' more details for assisting the bio-mechanism research in the near future.

The final chapter is devoted to summarize the work of this dissertation as well as draw a picture of future work.

1.5 References

[1] H. Helmholtz and H. E. Fripp, *On the limits of the optical capacity of the microscope*. The Monthly Microscopical Journal **16**(1), 15-39 (1876).

[2] E. Betzig, G. H. Patterson, R. Sougrat, O. W. Lindwasser, S. Olenych, J. S. Bonifacino, M. W. Davidson, J. Lippincott-Schwartz and H. F. Hess, *Imaging intracellular fluorescent proteins at nanometer resolution*. Science **313**(5793), 1642-1645 (2006).

[3] A. Gräslund, R. Rudolf and W. Jerker, *Single molecule spectroscopy in chemistry, physics and biology: Nobel symposium number 138*. Springer Series in Chemical Physics, Springer, Heidelberg, Germany, (2010) vol. 96, pp. 572.

[4] S. W. Hell and J. Wichmann, *Breaking the diffraction resolution limit by stimulated emission: stimulated-emission-depletion fluorescence microscopy*. Optics Letters **19**(11), 780-782 (1994).

[5] K. R. Spring and M. W. Davidson, *Introduction to fluorescence microscopy*, http://www.microscopyu.com/articles/fluorescence/fluorescenceintro.html, Nikon MicroscopyU, Access date: 06 Nov., 2015.

[6] V. Westphal, S. O. Rizzoli, M. A. Lauterbach, D. Kamin, R. Jahn and S. W. Hell, *Video-rate far-field optical nanoscopy dissects synaptic vesicle movement*. Science **320**(5873), 246-249 (2008).

[7] S. W. Hell and J. Wichmann, *Breaking the diffraction resolution limit by stimulated emission: stimulated-emission-depletion fluorescence microscopy*. Optics Letters **19**(11), 780-782 (1994).

[8] T. A. Klar and S. W. Hell, *Subdiffraction resolution in far-field fluorescence microscopy*. Optics Letters **24**(14), 954-956 (1999).
[9] S. T. Hess, T. P. K. Girirajan and M. D. Mason, *Ultra-high resolution imaging by fluorescence photoactivation localization microscopy*. Biophysical Journal **91**(11), 4258--4272 (2006).
[10] M. G. L. Gustafsson, *Surpassing the lateral resolution limit by a factor of two using structured illumination microscopy*. Journal of Microscopy **198**(2), 82-87 (2000).
[11] D. Li, L. Shao, B.-C. Chen, X. Zhang, M. Zhang, B. Moses, D. E. Milkie, J. R. Beach, J. A. Hammer and M. Pasham, *Extended-resolution structured illumination imaging of endocytic and cytoskeletal dynamics*. Science **349,** , (2015).
[12] M. G. Gustafsson, *Nonlinear structured-illumination microscopy: wide-field fluorescence imaging with theoretically unlimited resolution*. Proceedings of the National Academy of Sciences of the United States of America **102**(37), 13081-13086 (2005).
[13] Y. Oshikane, T. Kataoka and M. Okuda, *Observation of nanostructure by scanning near-field optical microscope with small sphere probe*. Science & Technology of Advanced Materials **8**(3), 181–185 (2007).
[14] U. Dürig, D. W. Pohl and F. Rohner, *Near field optical scanning microscopy*. Journal of Applied Physics **59**(10), 3318 - 3327 (1986).
[15] D. J. Stephens and J. Victoria, *Light microscopy techniques for live cell imaging*. Journal of the Graduates Sun Yat-Sen University(Natural Sciences、Medicine) **300**(5616), 82-87 (2008).
[16] J. A. Conchello and J. W. Lichtman, *Optical sectioning microscopy*. Nature Methods **2**(03), 920-931 (2005).
[17] J. B. Pawley, *Handbook of biological confocal microscopy*. Springer, Berlin, 3rd ed., (2006).
[18] OLYMPUS, *Product details of confocal laser scanning microscope FV3000*, http://www.olympus-lifescience.com/en/laser-scanning/fv3000/, Access date: 15 September, 2016.
[19] W. Xu, ., M. H. Jericho, H. J. Kreuzer and I. A. Meinertzhagen, *Tracking particles in four dimensions with in-line holographic microscopy*. Optics Letters **28**(3), 164-166 (2003).
[20] J. Rosen and G. Brooker, *Non-scanning motionless fluorescence three-dimensional holographic microscopy*. Nature Photonics **2**(3), 190-195 (2008).
[21] PhaseView, *Product details of InSight3D*, http://phaseview.com/3d-digital-imaging/insight3d/, Access date: 21 November, 2015.
[22] P. Prabhat, S. Ram, E. S. Ward and R. J. Ober, *Simultaneous imaging of different focal planes in fluorescence microscopy for the study of cellular dynamics in three dimensions*. IEEE Trans. Nanobioscience **3**(4), 237-242 (2004).
[23] R. Tomer, K. Khairy, F. Amat and P. J. Keller, *Quantitative high-speed imaging of entire developing embryos with simultaneous multiview light-sheet microscopy*. Nature Methods **9**(7), 755-763 (2012).
[24] S. Abrahamsson, *Multi-focus microscopy for aberration-corrected multi-color three-dimensional imaging*, A dissertation for the degree of Doctor of Philosophy, University of California, San Francisco and University of California, Berkeley, (2012).
[25] S. Ram, D. Kim, R. Ober and E. S. Ward, *3D single molecule tracking with multifocal plane microscopy reveals rapid intercellular transferrin transport at epithelial cell barriers*. Biophysical Journal **103**(7), 1594–1603 (2012).

[26] P. P. Mondal, S. Dilipkumar and K. Mohan, *Efficient generation of diffraction-limited multi-sheet pattern for biological imaging*. Optics Letters **40**(4), 609-612 (2015).
[27] A. H. Greenaway and P. M. Blanchard, *Three-dimensional imaging system*. in United States Patent No. 6,975,457 B1. Application No. 09/622,405, (QinetiQ Limited, London, 2005).
[28] P. M. Blanchard and A. H. Greenaway, *Simultaneous multiplane imaging with a distorted diffraction grating*. Applied Optics **38**(32), 6692-6699 (1999).
[29] Y. Feng, P. A. Dalgarno, D. Lee, A. H. Greenaway, Y. Yang and R. R. Thomson, *Optical system*. in UK Intellectual Property Office. UK Patent Application No. GB2504188-A, (Marks & Clerk LLP Edinburgh Office, United Kingdom, 2013).
[30] Y. Feng, P. A. Dalgarno, D. Lee, Y. Yang, R. R. Thomson and A. H. Greenaway, *Chromatically-corrected, high-efficiency, multi-colour, multi-plane 3D imaging*. Optics Express **20**(18), 20705-20714 (2012).
[31] M. Born and E. Wolf, *Principles of optics*. Cambridge University Press, Cambridge, Corrected reprint of the 7th edition, (2001).
[32] T. A. Planchon, G. Liang, D. E. Milkie, M. W. Davidson, J. A. Galbraith, C. G. Galbraith and E. Betzig, *Rapid three-dimensional isotropic imaging of living cells using Bessel beam plane illumination*. Nature Methods **8**(5), 417-423 (2011).
[33] V. Garcés-Chávez, ., D. Mcgloin, ., H. Melville, ., W. Sibbett, . and K. Dholakia, . *Simultaneous micromanipulation in multiple planes using a self-reconstructing light beam*. Nature International Weekly Journal of Science **419**(6903), 145-147 (2002).
[34] J. D. Joannopoulos, *Self-assembly lights up*. Nature **414**(6861), 257-258 (2001).
[35] A. H. Voie, D. H. Burns and F. A. Spelman, *Orthogonal-plane fluorescence optical sectioning: three-dimensional imaging of macroscopic biological specimens*. Journal of Microscopy **170**(3), 229-236 (1993).
[36] H. Jan, S. Jim, D. B. Filippo, W. Joachim and E. H. K. Stelzer, *Optical sectioning deep inside live embryos by selective plane illumination microscopy*. Science **305**(5686), 1007-1009 (2004).
[37] J. Huisken and D. Y. Stainier, *Selective plane illumination microscopy techniques in developmental biology*. Development **136**(12), 1963-1975 (2009).
[38] M. G. L. Gustafsson, S. Lin, P. M. Carlton, C. J. R. Wang, I. N. Golubovskaya, C. W Zacheus, D. A. Agard and J. W. Sedat, *Three-dimensional resolution doubling in wide-field fluorescence microscopy by structured illumination*. Biophysical Journal **94**(12), 4957–4970 (2008).
[39] G. Liang, S. Lin, C. D. Higgins, J. S. Poulton, P. Mark, M. W. Davidson, W. Xufeng, G. Bob and B. Eric, *Noninvasive imaging beyond the diffraction limit of 3D dynamics in thickly fluorescent specimens*. Cell **151**(6), 1370-1385 (2012).
[40] B.-C. Chen, W. R. Legant, K. Wang, L. Shao, D. E. Milkie, M. W. Davidson, C. Janetopoulos, X. S. Wu, J. A. H. III, L. Zhe, B. P. English, Y. Mimori-Kiyosue, D. P. Romero, A. T. Ritter, J. Lippincott-Schwartz, L. Fritz-Laylin, R. D. Mullins, D. M. Mitchell, J. N. Bembenek, A.-C. Reymann, R. Böhme, S. W. Grill, J. T. Wang, G. Seydoux, U. S. Tulu, D. P. Kiehart and E. Betzig, *Lattice light-sheet microscopy: imaging molecules to embryos at high spatiotemporal resolution*. Science **346**(6208), 1257998-1257998 (2014).
[41] J. M. Beckers, *Adaptive optics for astronomy: principles, performance, and applications*. Annual Review of Astronomy & Astrophysics **31**(1), 13-62 (2003).
[42] A. Greenaway, *Seeing more clearly*. Physics World **23**(8), 33-36 (2010).

[43] P. M. Blanchard, D. J. Fisher, S. C. Woods and A. H. Greenaway, *Phase-diversity wave-front sensing with a distorted diffraction grating*. Applied Optics **39**(35), 6649-6655 (2000).

[44] P. M. Blanchard and A. H. Greenaway, *Multiplane imaging and wavefront sensing using distorted diffraction gratings*. Paper presented at Trends in Optics and Photonics. Diffractive Optics and Micro-Optics. Vol.41. Technical Digest. Postconference Edition, Quebec City, Canada:Opt. Soc. America. p. 250-252, 18-22 June (2000).

[45] P. M. Blanchard and A. H. Greenaway, *Broadband simultaneous multiplane imaging*. Optics Communications **183**(1), 29-36 (2000).

[46] J. Bucklew and N. Gallagher Jr, *Detour phase error in the Lohmann hologram*. Applied Optics **18**(4), 575-580 (1979).

[47] Y. Feng, *Optimization of phase gratings with applications to 3D microscopy imaging*, A dissertation for the degree of Doctor of Philosophy, Precision Instruments and Machinery, University of Science and Technology of China, Hefei, China (2013).

[48] Y. Feng, L. Scholz, D. Lee, H. Dalgarno, D. Foo, L. Yang, W. Lu and A. Greenaway, *Multi-mode microscopy using diffractive optical elements*. Engineering Review **31**(2), 133-139 (2011).

[49] S. Abrahamsson, J. Chen, B. Hajj, S. Stallinga, A. Y. Katsov, J. Wisniewski, G. Mizuguchi, P. Soule, F. Mueller and C. D. Darzacq, *Fast multicolor 3D imaging using aberration-corrected multifocus microscopy*. Nature Methods **10**(1), 60-63 (2013).

[50] S. Abrahamsson, M. Mcquilken, S. B. Mehta, A. Verma, J. Larsch, R. Ilic, R. Heintzmann, C. I. Bargmann, A. S. Gladfelter and R. Oldenbourg, *MultiFocus Polarization Microscope (MF-PolScope) for 3D polarization imaging of up to 25 focal planes simultaneously*. Optics Express **23**(6), 7734-7754 (2015).

[51] C. S. Smith, S. Preibisch, A. Joseph, S. Abrahamsson, B. Rieger, E. Myers, R. H. Singer and D. Grunwald, *Nuclear accessibility of β-actin mRNA is measured by 3D single-molecule real-time tracking*. Journal of Cell Biology **209**(4), 609-619 (2015).

[52] J. Chen, Z. Zhang, L. Li, B.-C. Chen, A. Revyakin, B. Hajj, W. Legant, M. Dahan, T. Lionnet, E. Betzig, R. Tjian and Z. Liu, *Single-molecule dynamics of enhanceosome assembly in embryonic stem cells*. Cell **156**(6), 1274-1285 (2014).

[53] J. W. Goodman, *Introduction to Fourier optics*. Roberts and Company Publishers, 3rd edition, (2005).

[54] Y. Feng, H. I. C. Dalgarno, P. Dalgarno and A. H. Greenaway, *High efficiency 3D imaging using diffractive optical elements*. Paper presented at The 15th European Microscopy Congress, Manchester, 16th - 21st September (2012).

Chapter 2

Principles of QD grating and 4D imaging system

Preface

This chapter reviews principles of QD grating and 4D imaging system. We begin with the theory of QD grating and its application in 4D imaging system, which were first developed by Paul Blanchard and Alan Greenaway [1-5]. This theory underlines my current work in all the following chapters. Then we discuss my previous work about optical efficiency optimization and error budget. To estimate and optimize the optical efficiency of QD grating, a rough 1D mathematical model is built up and the intensity distribution of first three diffraction orders can be obtained. For precisely describing the properties of QD grating, a delicate 2D mathematical model is established in Chapter 3. The error budget reveals that the dominant error of optical system is chromatic smearing, accordingly we develop a new scheme of chromatic correction using a pair of grisms which will be illustrated in Chapter 4.

We note that the purpose for presenting my previous work which has been submitted to my first PhD dissertation [6] is to provide a base for the further work undertaken in this dissertation.

2.1 How a QD grating works in 4D imaging system?

QD grating is the abbreviation of quadratically distorted grating, which is also called curved grating. The main difference between QD grating and general grating is the shape of grooves. The general grating is comprised of many straight equidistant slits whereas the QD grating is formed by the arcs of a series of concentric circles with varying radii (left picture in Fig. 2.1). As demonstrated on the right of Fig. 2.1, QD grating can also be described as an off-axis Fresnel Zone Plate (FZP) [7], which behaves like a lens but utilizes principle of diffraction instead of refraction.

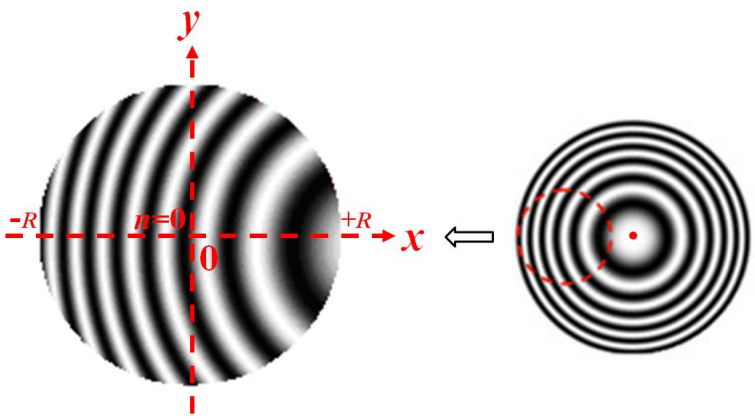

Fig. 2.1 A demonstration of the structure of QD grating in an x-y Cartesian coordinate system.

Due to the characteristic shape of grooves, the QD grating leads to an additional phase term to light which passes through it. Since this phase term is produced by the detour of grating grooves rather than the etch depth phase term which is produced by a normal phase grating, it is the so called *detour phase*. Therefore the form of detour phase term is determined by the way in which the grating grooves are distorted. In this section, we will explore the principle of QD grating and how it works in 4D imaging system. To make the following description clear and concise, I declare that most of the content introduced in this section is based on the work of my supervisor Alan H. Greenaway and his colleague Paul M. Blanchard [1-5], and these references will not be repeatedly cited.

2.1.1 Principle of QD grating

Fresnel zone plate (FZP) is a classical diffractive optical element (DOE), which serves as a flat lens but focuses light using diffraction rather than refraction or reflection. The FZP consists of a set of radially symmetric rings that alternate between either opaque/transparent (in an amplitude way) or different optical thickness (in a phase way). And the zones can be spaced so that the diffracted light constructively interferes at the desired focus, creating an image there [8]. The QD grating, which is also known as an *off-axis FZP*, can create multiple copies of the focussed image distributed along the axis of the plate. In an alternative way, QD grating can be used to image multiple object planes onto a single image plane.

Differing from most other uses of DOEs, which make practical use of only a single diffraction order, the QD grating discussed here makes simultaneous use of the zeroth,

the first, and potentially higher diffraction orders. A quadratic displacement function is used to alter the optical transfer function associated with each diffraction order such that each order has a different degree of defocus. The level of a phase shift, which is introduced by the displacement of the grating grooves in a direction perpendicular to the long grating lines, is dependent on the amount of local distortion of the grating relative to its undistorted form. Considering a binary QD grating, we define an X-Y Cartesian coordinate system in which the *x* axis is perpendicular to the grooves and the *y* axis is parallel to the grooves in the grating, as shown in Fig. 2.2. Thus the local phase shift for each diffraction order could be described as,

$$\phi_m(x,y) = \frac{2\pi m \Delta_x(x,y)}{d} \tag{2.1}$$

where $\Delta_x(x,y)$ is the displacement of the grating grooves relative to its undistorted position, thus $\phi_m(x,y)$ is the phase shift applied to diffraction order *m* in a grating of period *d*.

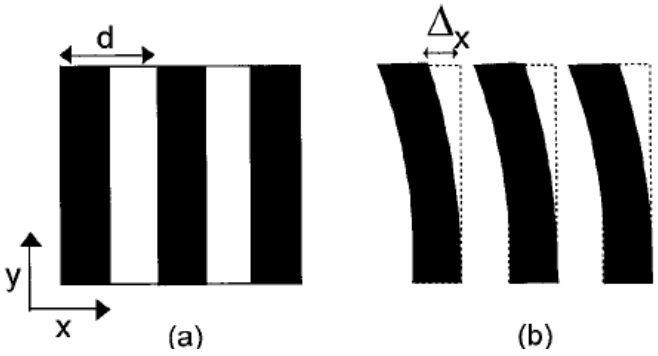

Fig. 2.2 Schematic of grating grooves: (a) undistorted grooves with period d; (b) distorted grooves with amount of local shift Δ_x [3].

To explore the different levels of defocus that are diffracted into each order, the phase profile which modifies the wavefront curvature should also be considered. The phase profile of a QD grating that imparts a spherical phase delay could be written as,

$$\phi(r) = \frac{2\pi}{\lambda}[f - (f^2 - r^2)^{1/2}] \tag{2.2}$$

where λ is the incident wavelength, *f* is the element focal length (or radius of curvature introduced) and *r* is a radial coordinate. Eq. (2.2) can be expanded as,

$$\phi(r) = \frac{2\pi}{\lambda}[\frac{r^2}{2f} + \frac{r^4}{8f^3} + \frac{r^6}{16f^5} + ...] \tag{2.3}$$

The complete grating incorporates both defocus and spherical aberration correction and will be distorted according to,

$$\Delta_x(x,y) = \frac{d}{\lambda}[\frac{(x-x_0)^2 + (y-y_0)^2}{R^2}W_{20} + \frac{(x^2+y^2)^2}{R^4}W_{40} + \frac{(x^2+y^2)^3}{R^6}W_{60} + \text{higher order terms}] \tag{2.4}$$

where R is the radius of the grating aperture, x and y are Cartesian coordinates relative to an origin on the optical axis in the plane of the grating, x_0 and y_0 are the offsets of the origin of the quadratic distortion function from the optical axis of the system, W_{20} is the standard coefficient of defocus and is equivalent to the extra path length introduced at the edge of the aperture (in this case for the wave front diffracted into the +1 order), and W_{40} and W_{60} represent the spherical aberration terms. Since the spherical aberration should be centred on the optical axis, the offsets of these terms (W_{40}, W_{60} and higher terms) are not exploited in Eq. (2.4). In the paraxial approximation case, only the first terms of Eq. (2.3)-(2.4) are being considered. So combining the grating equation Eq. (1.5) and Eq. (2.1), when W_{20} is non-zero the expansion of the defocus (first) term in Eq. (2.4) produces a phase shift given by,

$$\phi(x,y) = W_{20}[\frac{2\pi m}{R^2\lambda}(x^2+y^2) - \frac{4\pi m x_0}{R^2\lambda}x - \frac{4\pi m y_0}{R^2\lambda}y + \frac{2\pi m}{R^2\lambda}(x_0^2+y_0^2)] \tag{2.5}$$

When the quadratic function centred on the optical axis, the defocus phase term can be written as,

$$\phi(x,y) = m\frac{2\pi W_{20}}{\lambda R^2}(x^2+y^2) \tag{2.6}$$

which shows that shifting the origin of the quadratic function has no effect on the level of defocus introduced into each diffraction order.

The second term in Eq. (2.5),

$$\phi(x,y) = -\frac{4m\pi}{\lambda R^2}W_{20}x_0 x \tag{2.7}$$

represents a linear increase in phase across the x-axis of the grating plane. If x_0 is chosen to have a value of,

$$x_0 = \frac{\lambda R^2}{2 d_0 W_{20}} \tag{2.8}$$

then Eq. (2.7) becomes equal to,

$$\phi(x, y) = -\frac{2\pi m x}{d} \tag{2.9}$$

This phase tilt is equal and opposite in sign to that introduced into light scattered from the grating structure (Eq.(2.1)). The cancellation of these two terms for each order causes the diffraction order spacing to become zero in a plane perpendicular to the optical axis, corresponding to all of the orders lying along the optical axis of the system. The diffraction orders remain spatially separated along the optical axis according to the level of defocus within the distorted grating. The shift of the origin of the quadratic function to that defined in Eq. (2.8) leads to a grating structure consisting of concentric circular fringes, like that demonstrated in Fig. 2.1.

The third term in Eq. (2.5) causes the diffraction orders (except the zeroth order) to move along the y-direction in the image plane, which has the similar effect on the phase of grating to Eq. (2.7). And the final term in Eq. (2.5) has no effect on the wavefront shape diffracted into each order. Therefore the position of a particular diffraction order in the image plane can be controlled through choice of x_0 and y_0, whilst leaving the level of defocus unchanged. Hence the distortion of QD grating can be described as,

$$\Delta_x(x, y) = \frac{W_{20} d}{\lambda R^2}(x^2 + y^2) \tag{2.10}$$

And the equation of the grating arcs is,

$$\frac{x}{d_0} + \frac{W_{20}(x^2 + y^2)}{\lambda R^2} = n \tag{2.11}$$

where d_0 is the grating period at the aperture centre, and the integer values of n are the loci of each grating arc — $n = 0$ corresponds to a grating arc that passes through the

mask centre and the values of n are opposite in sign to the x-direction (see Fig. 2.1). Thus the radii of the concentric grating arcs C_n can be written as,

$$C_n = [\frac{n\lambda R^2}{W_{20}} + (\frac{\lambda R^2}{2d_0 W_{20}})^2]^{1/2} \tag{2.12}$$

Since the grating period across the aperture is not constant, the grating period d at a distance x from the origin along the x axis can be given by,

$$d = \frac{d_0 \lambda R^2}{\lambda R^2 - 2d_0 W_{20} x} \tag{2.13}$$

Therefore when $x = -R$ the minimum grating period d_{min} is,

$$d_{\min} = \frac{d_0 \lambda R}{\lambda R + 2d_0 W_{20}} \tag{2.14}$$

Eq. (2.14) determines the accuracy of mask plotting in grating fabrication, from which we can see that for very high W_{20} values the period may become too fine to plot at the edge of aperture. Normally we work on the basis that the minimum period is not less than 2 μm. And the error budget of mask plotting will be discussed in the following section (Chapter 2.3). We note that the equation (7) in reference [3] is wrong in sign when the coordinate of minimum grating period in equation (10) corresponds to $x = -R$ (which is the same with my definition, as Fig. 2.1 shown).

2.1.2 Multi-plane 4D imaging by QD grating

The quadratic phase function Eq. (2.6) imparts a phase delay on wavefronts scattered into the nonzero diffraction orders such that the wavefront curvature is altered. Therefore the QD grating has focusing power in the nonzero orders, and an equivalent focal length f_m can be calculated for these orders. Comparison of Eqs. (2.3), (2.5) and (2.6) yields,

$$f_m = \frac{R^2 - (mW_{20})^2}{2mW_{20}} \tag{2.15}$$

where mW_{20} is the path length difference introduced at the edge of the aperture in the mth order. Here R is much greater than mW_{20}, thus Eq. (2.15) can be approximated by,

$$f_m = \frac{R^2}{2mW_{20}} \tag{2.16}$$

Since the QD grating is designed with defocus represented by $W_{20} = n\lambda$ (normally $n > 0$), f_m in the ±1st orders is typically not less than 500mm. Moreover, there is no real image in the negative orders so that QD grating is always applied as part of an optical system which provides the majority focussing power. In principle, the QD grating could be placed anywhere within a multielement optical system for effectively modifying the focal length of the system in each diffraction order. This grating-multielement combination can be used for imaging either a single object plane onto multiple image planes or multiple object planes onto a single image plane. In practice, a grating-lens combination is generally utilized for multi-focal imaging, in which a variable slit is used to ensure that the separate z-plane images do not overlap (see Fig. 2.3).

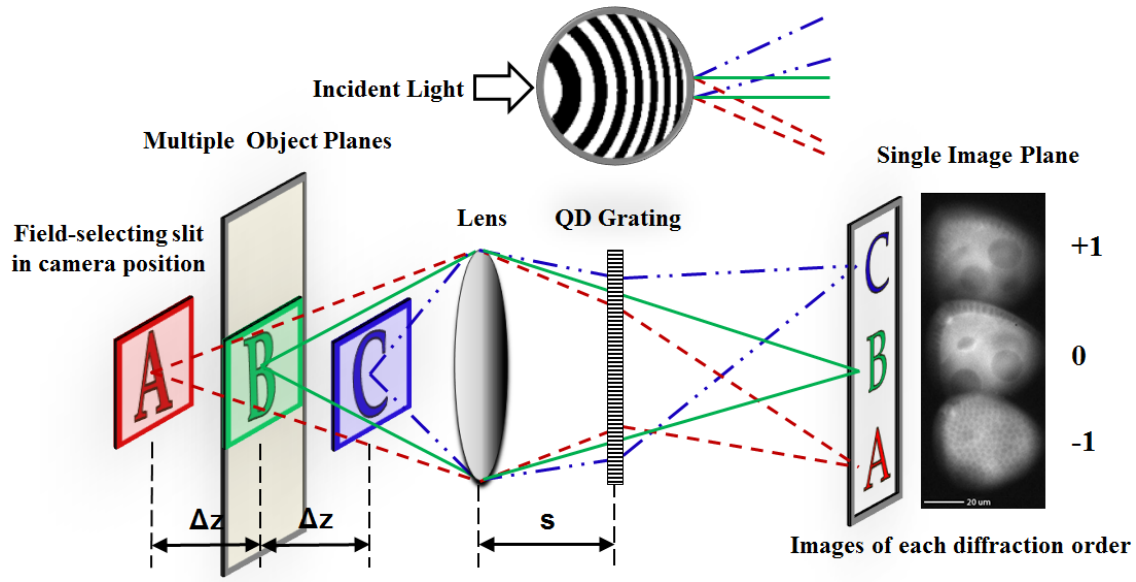

Fig. 2.3 Schematic of a QD grating based 4D imaging system.

Fig. 2.3 shows that objects A, B and C located at different distances from QD grating are imaged simultaneously and spatially separated on a single image plane and the biological images on the right side are the partial view of a stage 8 drosophila egg chamber (the separation of object planes Δz is about 7.3 μm in this case). It is clear that the small dark spheres in bottom image are the follicle cells and the large dark spheres in both top and central images are two nurse cell nuclei, whilst the oocyte in the central image is focussed well. This work was in collaboration with Prof. Ilan Davis of Oxford University.

The effective focal length of the combination (Fig. 2.3) in each diffraction order can be given by (from the thin lens approximation),

$$f_{meff} = \frac{f_L f_m}{f_L + f_m - s} \tag{2.17}$$

where f_L is the focal length of the lens and s is the separation between the lens and QD grating.

In practice we often set s to be equal to f_L then the magnification of the images of each diffraction order will be identical, and this condition is described as 'telecentric'. By setting up such a system, we do not need to re-scale the images of each layer when reconstructing the 3-dimensional object, which effectively avoids some possibilities of error(s) and makes image postprocessing easier.

The object planes are separated along the z-axis by [9],

$$\Delta z = \frac{f_L^2}{M^2 f_m} \tag{2.18}$$

where M is the total magnification of the system (normally the objective magnification in the telecentric case), and f_L could be replaced by the effective focal length of the lenses when a lens compound system is applied.

Due to the diffraction properties of QD grating and the energy limit of optical system, only the images of first 3 orders could be utilized. Thus the separation of object planes we are interested in is simply Δz, rather than the separations between objects/images of higher diffraction orders. Normally Δz should be chosen to meet the research requirement of biologists, whilst the separation of the images on the camera can be calculated using basic trigonometry. Here the physical size of the sensitive chip of the camera should be considered carefully so that the images may fit well onto the chip and make the best possible use of the whole area (see section 5.2.1 for details).

To set up a working system, there are still quite a lot of practical things to consider, and most of them involve a trade-off of some sort, i.e. the light efficiency in each image,

the bandpass effect on the image quality, the optimization of both QD grating and optical system, etc.

2.2 Optimization of optical efficiency by multi-etch of grating

As described in section 2.1, we have demonstrated a real-time 3D (thus 4D) imaging technology based on the QD grating, in which the transmission grating, in the form of an off-axis Fresnel zone plate, works as key element to image multiple object planes simultaneously on a single image plane. For the transmission QD grating we are using, efficiency is defined as the energy flow of light diffracted into the order being measured, relative to the energy flow of the incident light [10]. A grating with high efficiency is desirable for 4D imaging, especially in measuring/tracking rapidly moving live cells, with either weak signal or noisy background.

As early as 1874, Lord Rayleigh recognized that the energy flow distribution (by wavelength) of a diffraction grating could be altered by modifying the shape of the grating grooves [11]. Our grating is generated by dry etch, during which the AutoCAD/GDSII files of plotting mask are used to produce chrome on fused silica, and after that the fused silica is etched where there is no chrome and the chrome is then removed to leave a fused silica substrate with the phase grating in relief. Therefore we may evaluate the optical efficiency from controlling groove shape in the following aspects:

1. Line width and pitch

Present gratings are binary (i.e. two-level) structures and plotted with the mark to space ratio of 1:1. The present etch is a dry etch and we aim to get etch profiles with sides as vertical as possible. However, since the current fabrication of grating appears to produce acceptable results and we are not really able to measure the etch profile at the moment, we assume that the vertical edges have been produced. Another point to consider is that the production of gratings with different mark to space ratio might be advantageous in some applications. We may therefore simulate the effect and optimize the mark to space ratio in Mathematica software in the near future.

2. Etch depth

We use the etch depth to control the energy scattered into each diffraction order and we are generally interested only in the zero, +1 and -1 diffraction orders. We would generally etch to produce equal intensity in these 3 diffraction orders. In principle, increasing the number of levels etched beyond 2 can improve the optical efficiency [12, 13], thus we may need to develop our designs to write gratings with at least 3 levels (thus two etches).

3. Surface profile

The mean–surface profile cannot be straightforwardly measured as our assessment of the results of the etching process has only been made using a stylus probe and that cannot really give us accurate information. Actually, a comprehensive budget of the fabrication errors, including surface roughness error, should be implemented in order to find the factor(s) which has (have) significant impact on the optical efficiency of grating (see details in section 2.3.1). So we briefly assume that the etched-surface is perfect in this case.

However, it is difficult to separate the estimation of etch depth levels and the mark to space ratio, so a properly-evaluated grating model will need to take both into account. There are several ways in which we can try to achieve multilevel: the easiest (taking 3 levels for example) in terms of alignment is to etch two binary gratings of different etch depths, either on opposite sides of the substrate or (preferably) on the same side. If the etches are on the same side of the substrate, some areas would be etched twice or more. Here we will build a principal grating model on the basis of same sided multi-etch (up to 3 etches). In this section, full mathematical details with suitable commentary on the logical steps will be demonstrated and the principles can be expanded to higher etch levels. Since we just need to check the improvement of efficiency with increase of etch levels, a 1D phase grating model might be enough to illustrate the principle [14].

2.2.1 1D mathematical model of single-etch grating

Let us start off with the simplest grating model – single etch grating (i.e. two-level) with the mark to space ratio of 1:1. The grating consists of a unit cell of length $2L$ of which the interval $-\frac{L}{2} \leq x < \frac{L}{2}$ has the value unity and the interval $\frac{L}{2} \leq x < \frac{3L}{2}$ has the value A, where A is a complex, unimodular constant (Fig. 2.4).

So the definition of single-etch grating is,

$$f(x)=\begin{cases}1 & -\frac{L}{2}\le x<\frac{L}{2}\\ A & \frac{L}{2}\le x<\frac{3L}{2}\end{cases} \tag{2.19}$$

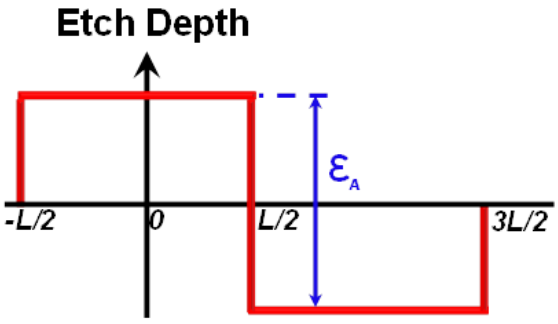

Fig. 2.4 Schematic of unit cell of single etch grating structure.

where $A = e^{i\phi_A}$, $\phi_A = \frac{2\pi\varepsilon_A(n-1)}{\lambda}$ is the phase step of grating, λ the wavelength, ε_A the etch depth and n the refractive index.

The extended grating is a convolution of the unit cell and a set of delta functions, with spacing $2L$. The Fourier Transform (FT) of the unit cell is the sum of the FT of the two unit-cell components. So if the FT is defined by $\int_{-\infty}^{\infty} \mathrm{d}x\, f(x)\exp(-ix\xi)$ [15], the FT of the unit cell is,

$$F(\xi)=\frac{2}{\xi}\sin(\frac{\xi L}{2})+\frac{2A}{\xi}\sin(\frac{\xi L}{2})\exp(-iL\xi) \tag{2.20}$$

where the exponent represents the phase shift due to the displaced position of the segment having complex transmittance.

The positions in ξ-space for the diffraction order n is $\xi = n\frac{\pi}{L}$. Thus the scattered intensity in ξ-space is the modulus squared of

$$F(\xi)=\frac{2\pi}{\xi L}\sin\left(\frac{\xi L}{2}\right)(1+A\exp(-iL\xi)) \tag{2.21}$$

where the $\frac{\pi}{L}$ comes from the FT of the array of delta functions.

For $n = 0$ we have $\xi = 0$, and thus for the zero-order,

$$\begin{aligned} F(0) &= \frac{2\pi}{\xi L}\sin\left(\frac{\xi L}{2}\right)(1+A) \\ &= \lim_{\xi\to 0}\left(\frac{2\pi}{\xi L}\cdot\frac{\xi L}{2}(1+A)\right) \\ &= \pi(1+A) \end{aligned} \tag{2.22}$$

For $n = \pm 1$ we have $\xi = \pm\frac{\pi}{L}$, and thus for the first-orders,

$$\begin{aligned} F\left(\frac{\pi}{L}\right) &= \frac{2\pi}{\frac{\pi}{L}L}\sin\left(\frac{\frac{\pi}{L}L}{2}\right)\left(1+A\exp(-iL\frac{\pi}{L})\right) \\ &= 2(1-A) \end{aligned} \tag{2.23}$$

Therefore the scattered intensities are,

$$\begin{aligned} I_0 &= \left|F(0)\right|^2 \\ &= 4\pi^2\cos^2(\frac{\phi}{2}) \end{aligned} \tag{2.24}$$

and

$$\begin{aligned} I_{\pm 1} &= \left|F(\frac{\pi}{L})\right|^2 \\ &= 16\sin^2(\frac{\phi}{2}) \end{aligned} \tag{2.25}$$

If the intensity is normalized such that a grating for which $A = 1$ (i.e. no grating) gives unit amplitude in the zero order, we can write,

$$I_0 = \cos^2(\frac{\phi}{2}) \tag{2.26}$$

and

$$I_{\pm 1} = \frac{4}{\pi^2}\sin^2(\frac{\phi}{2}) \tag{2.27}$$

Clearly, the fraction of incident energy scattered other diffraction orders is,

$$I_{\text{lost}} = (1-\frac{8}{\pi^2})\sin^2\left(\frac{\phi}{2}\right) \le 0.19 \tag{2.28}$$

Thus, there is always more than 81% of the incident flux detected in the 3 images in the 0^{th} and $\pm 1^{st}$ orders, this minimum being reached when the etch is of a depth to delete the zero order.

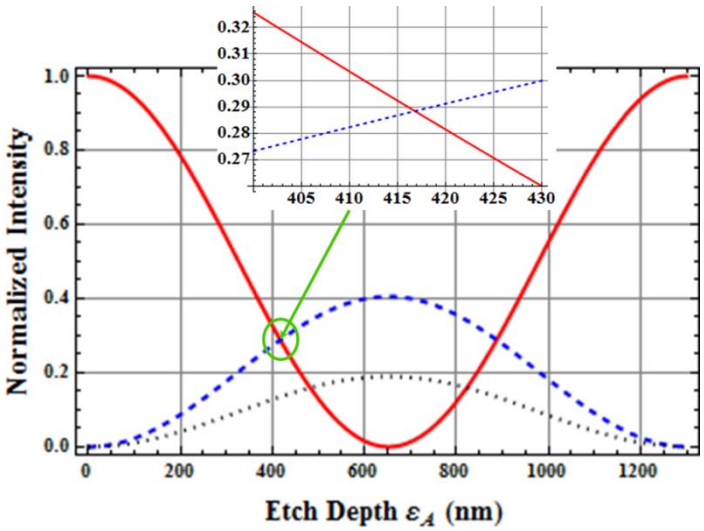

Fig. 2.5 In terms of single-etch grating, the energy can balance in the 0^{th} (solid red line) and $\pm 1^{st}$ (dashed blue) diffraction orders, and the fraction of the flux lost goes into higher diffraction orders (black dots).

The energy fraction in each order is plotted as Fig. 2.5, where the red line represents the zero order and the blue the $\pm 1^{st}$ orders. Solving for the intersections of the energy in the zero and $\pm 1^{st}$ order curves gives $\phi_A = 2.00777\,\text{rad}$ or $\phi_A = 4.27542\,\text{rad}$ when $0 < \phi_A \le 2\pi$. The corresponding etch depths are $\varepsilon_A = 416.8\text{nm}$ or $\varepsilon_A = 887.5\text{nm}$, if we choose $n = 1.46$ and $\lambda = 600\text{nm}$. The energy lost into higher diffraction orders at these values of $\phi < 13.45\%$. The zero and first diffraction orders each have 28.84%.

2.2.2 Efficiency optimization by double-etch of grating

Similar with the mathematical model of single-etch grating, the first layer of double-etch grating consists of a unit cell of length $2L$ of which the interval $-\frac{L}{2} \le x < \frac{L}{2}$ has the value unity and the interval $\frac{L}{2} \le x < \frac{3L}{2}$ has value A. Moreover, the real number 'y' indicates the fraction of the DOE exposed to the second etch, thus the intervals of the

second etch layer can be demonstrated as Fig. 2.6, which has the value B. Here A, B and AB are complex, unimodular constant, separately.

So the definition of double-etch grating is,

$$f(x)=\begin{cases} B & -\frac{L}{2}\le x_1<-y \\ 1 & -y\le x_2<y \\ B & y\le x_3<\frac{L}{2} \\ A & \frac{L}{2}\le x_4<L-y \\ AB & L-y\le x_5<L+y \\ A & L+y\le x_6<\frac{3L}{2} \end{cases} \tag{2.29}$$

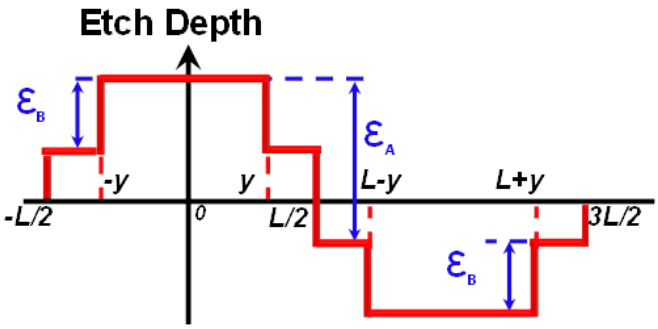

Fig. 2.6 Schematic of unit cell of double-etch grating structure (0<y<L/2).

where $A=e^{i\phi_A}$, $B=e^{i\phi_B}$; $\phi_A=\frac{2\pi\varepsilon_A(n-1)}{\lambda}$ and $\phi_B=\frac{2\pi\varepsilon_B(n-1)}{\lambda}$ are the phase steps of first and second etch layers separately, λ the wavelength, n the refractive index, ε_A and ε_B the etch depths of first and second etch layers separately.

Similarly with Eq. (2.21), the scattered intensity in ξ-space is the modulus squared of

$$F(\xi)=\frac{2\pi}{\xi L}\left(B+Ae^{-i\xi L}\right)\left[\sin\left(\xi\frac{L}{2}\right)-\sin(\xi y)\right]+\frac{2\pi}{\xi L}\left(1+ABe^{-i\xi L}\right)\sin(\xi y) \tag{2.30}$$

thus

$$F(0)=\pi(A+B)+\frac{2\pi y}{L}(1-A-B+AB) \tag{2.31}$$

$$F\left(\frac{\pi}{L}\right)=2\left(B-A\right)+2(1+A-B-AB)\sin\left(\frac{\pi}{L}y\right) \tag{2.32}$$

Then the amount of light diffracted into first 3 diffraction orders for a 2-bit etch phase grating can be given by,

$$I_0=[\cos(\frac{\phi_A-\phi_B}{2})-4y\sin(\frac{\phi_A}{2})\sin(\frac{\phi_B}{2})]^2 \tag{2.33}$$

$$I_{\pm1}=\frac{4}{\pi^2}[sin\left(\frac{\phi_A-\phi_B}{2}\right)+2\cos(\frac{\phi_A}{2})\sin(\frac{\phi_B}{2})\sin\left(\pi y\right)]^2 \tag{2.34}$$

To achieve 'highest' efficiency and intensity balance in first 3 orders, we need to find the 'working' phase of each etch and the interval of grating. Here we would like to calculate the conditional extreme value of total intensity $\mathrm{Max}[I_0+2I_{\pm1}]$ in first 3 orders with condition,

$$I_0-I_{\pm1}=0 \tag{2.35}$$

The calculation results show that optimizing the phase terms for balanced intensity in each order occurs when $\phi_A=1.60\mathrm{rad}$, $\phi_B=0.64\mathrm{rad}$ (i.e. $\varepsilon_A=332.8\mathrm{nm}$, $\varepsilon_B=132.5\mathrm{nm}$ if $\lambda=600\mathrm{nm}$ and $n=1.46$) and y=0.37. Under these conditions, the photon flux per order increases to 30.3%, and the remaining 9.1% is lost into higher diffraction orders, see Fig. 2.7.

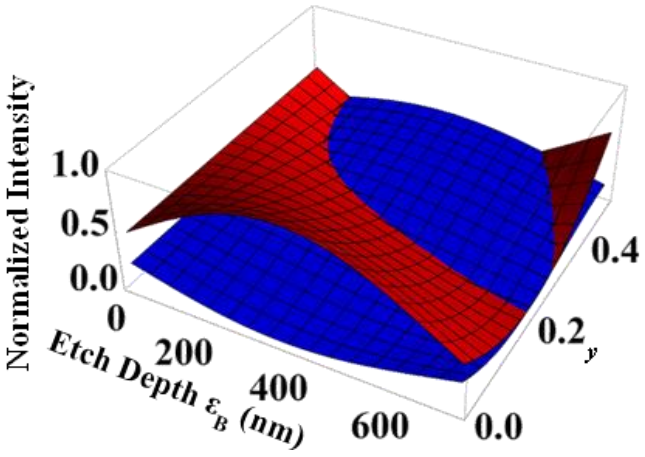

Fig. 2.7 3D Plot showing the energy distribution of double-etch grating in the 0th (red) and ±1st diffraction orders (blue).

Thus, we obtain 91% intensity in first 3 orders, increasing up to 92% by tolerating just 1% variation in the image energy in each order, see Fig. 2.8.

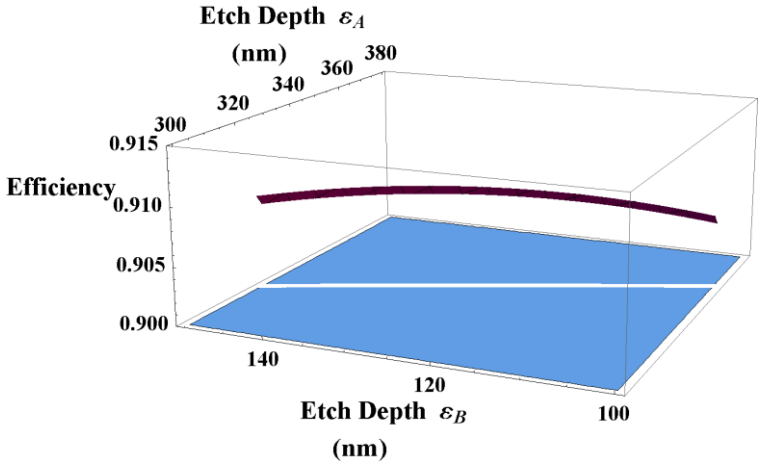

Fig. 2.8 The efficiency with balanced energies of first 3 orders is up to 92% if 1% variation of the image energy allowed.

The results are particularly beneficial when using multiple QD gratings, where diffraction losses cumulate. For example, 9-plane simultaneously imaging, using dual back-to-back QD gratings would result in higher order losses of 25.14% for single-etch grating compared to 17.37% for double-etch grating.

2.2.3 Efficiency optimization by triple-etch of grating

Similar with the definition of principal grating model above, the triple-etch grating can be expressed as following: the first layer of grating consists of a unit cell of length $2L$ of which the interval $-\frac{L}{2} \leq x < \frac{L}{2}$ has the value unity and the interval $\frac{L}{2} \leq x < \frac{3L}{2}$ has value A; the real number 'y' and 't' indicate the fraction of the grating exposed to the second and third etches separately. So the intervals of the second and third etch layers can be demonstrated as Fig. 2.9, which has the value B and C, separately. Here A, B, AB and ABC are complex, unimodular constant, separately.

So the definition of triple-etch grating is,

$$f(x)=\begin{cases} B & -\frac{L}{2}\le x_1<-y \\ C & -y\le x_2<-t \\ 1 & -t\le x_3<t \\ C & t\le x_4<y \\ B & y\le x_5<\frac{L}{2} \\ A & \frac{L}{2}\le x_6<L-y \\ AB & L-y\le x_7<L-t \\ ABC & L-t\le x_8<L+t \\ AB & L+t\le x_9<L+y \\ A & L+y\le x_{10}<\frac{3L}{2} \end{cases} \tag{2.36}$$

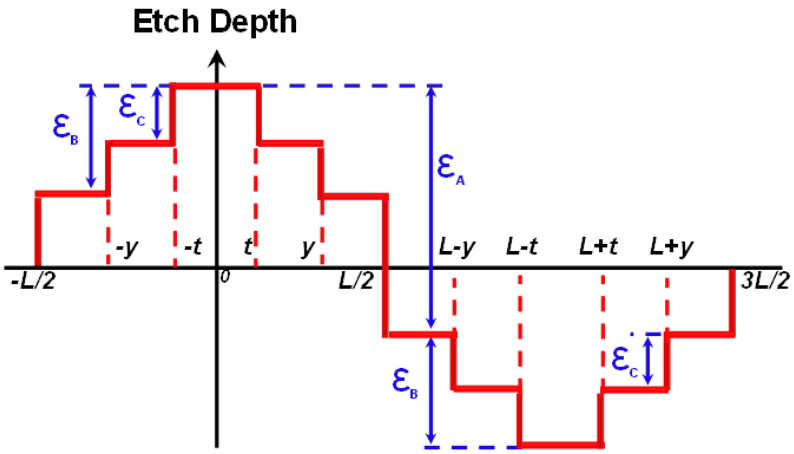

Fig. 2.9 Schematic of unit cell of triple-etch grating structure (0<y<L/2 & 0<t<y).

where $A=e^{i\phi_A}$, $B=e^{i\phi_B}$, $C=e^{i\phi_C}$; $\phi_A=\frac{2\pi\varepsilon_A(n-1)}{\lambda}$, $\phi_B=\frac{2\pi\varepsilon_B(n-1)}{\lambda}$ and $\phi_C=\frac{2\pi\varepsilon_C(n-1)}{\lambda}$ are the phase steps of first, second and third etch layers separately, λ the wavelength, n the refractive index, ε_A, ε_B and ε_C the etch depths of first, second and third etch layers separately.

Again, similar with the mathematical process in foregoing sections, we could work out the normalized energy distribution in 0^{th} and $\pm1^{st}$ orders as following,

$$
\begin{aligned}
I_0 &= \cos^2\left(\frac{\phi_A-\phi_B}{2}\right) \\
&-4y\cos\left(\frac{\phi_A-\phi_B}{2}\right)\left[\cos\left(\frac{\phi_A-\phi_B}{2}\right)-\cos\frac{\phi_C}{2}\cos\left(\frac{\phi_A+\phi_B-\phi_C}{2}\right)\right] \\
&-4t\cos\left(\frac{\phi_A-\phi_B}{2}\right)\sin\left(\frac{\phi_A+\phi_B}{2}\right)\sin\phi_C \\
&+4y^2\left[\cos^2\left(\frac{\phi_A-\phi_B}{2}\right)-2\cos\left(\frac{\phi_A-\phi_B}{2}\right)\cos\left(\frac{\phi_A+\phi_B-\phi_C}{2}\right)\cos\frac{\phi_C}{2}+\cos^2\left(\frac{\phi_A+\phi_B-\phi_C}{2}\right)\right] \\
&+16yt\sin\left(\frac{\phi_A+\phi_B}{2}\right)\sin\frac{\phi_C}{2}\left[\cos\left(\frac{\phi_A-\phi_B}{2}\right)\cos\frac{\phi_C}{2}-\cos\left(\frac{\phi_A+\phi_B-\phi_C}{2}\right)\right] \\
&+16t^2\sin^2\left(\frac{\phi_A+\phi_B}{2}\right)\sin^2\frac{\phi_C}{2}
\end{aligned}
\tag{2.37}
$$

$$
\begin{aligned}
I_{\pm1} &= \frac{4}{\pi^2}\{\sin^2\left(\frac{\phi_A-\phi_B}{2}\right) \\
&+\sin^2(\pi y)\left[\sin^2\left(\frac{\phi_A-\phi_B}{2}\right)+\sin^2\left(\frac{\phi_A+\phi_B-\phi_C}{2}\right)-2\sin\left(\frac{\phi_A-\phi_B}{2}\right)\cos\frac{\phi_C}{2}\sin\left(\frac{\phi_A+\phi_B-\phi_C}{2}\right)\right] \\
&+4\sin^2(\pi t)\cos^2\left(\frac{\phi_A+\phi_B}{2}\right)\sin^2\frac{\phi_C}{2} \\
&+2\sin(\pi y)\sin\left(\frac{\phi_A-\phi_B}{2}\right)\left[\cos\left(\frac{\phi_A-\phi_C}{2}\right)\sin\left(\frac{\phi_B-\phi_C}{2}\right)+\cos\left(\frac{\phi_A}{2}\right)\sin\left(\frac{\phi_B}{2}\right)\right] \\
&+2\sin(\pi t)\sin\phi_C\cos\left(\frac{\phi_A+\phi_B}{2}\right)\sin\left(\frac{\phi_A-\phi_B}{2}\right) \\
&+4\sin(\pi y)\sin(\pi t)\sin\frac{\phi_C}{2}\cos\left(\frac{\phi_A+\phi_B}{2}\right)\left[\cos\left(\frac{\phi_A}{2}\right)\sin\left(\frac{\phi_B-\phi_C}{2}\right)+\sin\frac{\phi_B}{2}\cos\left(\frac{\phi_A-\phi_C}{2}\right)\right]\}
\end{aligned}
\tag{2.38}
$$

The analytic expressions of I_0 and $I_{\pm1}$ (equations (2.37) and (2.38)) are so complicated that we tried a few algorithms to work out the global maximum or conditional extreme values. However, quite a few of classic statistic models seem not applicable in this case. Monte Carlo algorithm is always used for obtaining numerical solutions to problems too complicated to be solved analytically, but it is a stochastic technique based on the use of random numbers and probability statistics which might not be appropriate for our case [16]. Genetic algorithm is often applied as an approach to solve global optimization problems, which is actually a search technique to find exact or approximate solutions to optimization and search problems [17]. However, the stop criterion is not clear in each problem as a result of that the so-called 'better' solution is only in comparison to other solutions. On the other hand, we also attempted to utilize

some optimization algorithms to see if better solution(s) could be found. One of them is simulated annealing, which was developed in 1983 and originally used to deal with highly nonlinear problems [18]. Since the calculation starts off with a random point and may find a local maximum as the final result rapidly, the global maximum is rarely to be found, whilst the related convergence analysis and potential period of computation could be painful [19].

So we got back to the similar solution as illustrated in section 2.2.2, but calculated by Mathematica software with rigorous constraints. We found that the conditional extreme value of efficiency could reach to 91.36% if the parameters $\phi_A = 7.821\text{rad}$, $\phi_\text{B} = 0.671\text{rad}$, $\phi_\text{C} = 0.103\text{rad}$, $y = 0.386$ and $t = 0.201$ were selected, subject to $0<y<0.39$ and $0<t<y$ constraints. It shows that efficiency of triple-etch grating is only 0.4% higher than that of double-etch grating, so multi-etch (>3) may deliver nominal improvement.

2.2.4 Conclusions

It is demonstrated that grating efficiency could be improved by multi-etch fabrication, using theoretical models of gratings based on an analytical solution to the optimization of the multi-level phase conditions. Under the conditions of refractive index n=1.46 (fused silica) and wavelength of incident light λ=600nm, a set of optimized parameters of grating structure are obtained, which achieve a balanced intensity distribution between diffraction orders and maximum value of grating efficiency. The results show that each order contains 28.84%, 30.3% and 30.45% of the flux, when the grating is single, double and triple etched, respectively. For higher etch levels, we can set up an iterative (i.e. simply numerical) solution to investigate whether a more complex structure than we can easily model would give a superior solution. Using Mathematica software, we made an iterative loop to code the grating in real space, Fourier transform, modulus square, compare peak heights and the energy in the first 3 orders, retain the phase of the grating FT but set the first 3 orders to be equal in strength (mod squared).

Here we may conclude that double-etch is good enough because few efficiency gain would be obtained in 3 and higher etch levels. Thus we will concentrate on the fabrication of double-etch grating in the near future and some grating fabrication methods are explored. Actually the fabrication methods should be similar for all etch levels, which fall into two categories: etching the substrate material away, and

depositing/casting the material onto substrate. We have had focused on each of them respectively and tried to find an improved method which could be an appropriate fabrication technique for our grating. Film deposition might be a potential way due to the high accuracy of film thickness, although few promising result has been obtained yet [6]. And concerning the alignment, the two grating masks involved should be oriented at 90 degrees to each other with this angle as accurate as possible, but errors of even a few degrees would not seriously impede operation (at least in test measurements). The lateral displacements of the grating centres should, again, be as accurate as possible, but alignment errors of up to 100 microns should not obstruct test measurements.

2.3 Error budget — limitations of QD grating based 4D imaging system

Errors affecting the accuracy of QD grating based 4D imaging can be treated under two convenient headings – those arising from defects in the grating structures (say *fabrication error*) and those arising from conventional optics (say *optical system error*). Experimentally, all of the QD grating-based schemes discussed here are used with an imaging system based on an optical relay between the usual microscope detector port and the image plane (to which the users' chosen camera is displaced) [20].

2.3.1 Fabrication errors of grating

The fabrication work will be assessed through accurate measurement of the diffraction of a laser beam by the gratings – any errors in the fabrication will be revealed by an imbalance in the energy scattered into each diffraction order. Relating this to a model (as illustrated in section 2.2.1) can give an indication of the accuracy of the etch (provided that the refractive index of the material is reliable). Measurement of higher diffraction orders can provide additional verification of the model. Asymmetries in the pattern of scattered intensity will reveal any accidental blaze produced during the fabrication, and relating the measurements to the model can produce an assessment of the blaze produced. Measurement of the diffuse scatter will provide information on the surface roughness and the accuracy of the vertical edges, although it may prove difficult to separate these influences.

In this subsection, we will explore some principal sources of fabrication error, i.e. etch depth, surface roughness and plotting, and find the dominant error(s) to guide the practice.

2.3.1.1 Etch depth error

The accuracy in etch depth determines the percentage of the incident light that is directed into each order. The energy balance between different diffraction orders is, as shown in Fig. 2.5, dependent on the phase-profile of grating. To achieve the desired intensity balance between the images in each diffraction order it is important to control the etch depth. We design the gratings but these are etched into a fused silica substrate commercially. The etch depth is reasonably uniform across each set of 16 gratings that are etched together, but it is important to know how precisely a target etch depth can be achieved in order to determine the energy imbalance between the images.

To model the effect of such error we assume that the etch-depth, ζ, is Normally distributed with the target mean and a given standard deviation. Eqs. (2.26) and (2.27) then allow us to estimate the energy balance. Both analytical and numerical integrals were performed [6], but will not be elaborated here due to the parallel deducing process with that illustrated in section 2.2.1. The results indicate that the energy balance between zero and first diffraction orders is less than 4%, with a 95% probability, if the standard deviation on the etch depth error is less than 2nm.

For a fused silica substrate (refractive index 1.46) we would aim for an etch depth of about 361nm if working at a wavelength of 520nm. On a relatively small sample of etch runs the depth error appears to be typically ~2nm with just one example exceeding 7nm error. The experimental results indicate about 5% variation in the energy balance between the diffraction orders and we have been able to work with that variability. The accuracy with which our former supplier (Photronics Inc) has etched the gratings has been about ±3nm. It seems that we can use a single etch with a high certainty of getting the correct energy balance for the selected wavelength.

2.3.1.2 Surface roughness

The surface roughness contains all spectral scales and leads to scattering of light out of the useful images to all angles. The effect of residual roughness in the grating etch can be analysed using the Maréchal approximation [21] to assess its effect on the Strehl ratio, whilst Strehl ratio is defined as the ratio of the observed peak intensity at detection compared to the theoretical maximum peak intensity of a perfect imaging system working at the diffraction limit [22, 23].

The residual roughness can be measured by stylus contact and, in the examples fabricated thus far, has an rms amplitude of ~3nm. The effect on the optical wavefront also depends on the scale length of the error, since roughness with a scale length significantly below one wavelength will tend to be averaged, but we assume that the rms roughness applies equally at all lateral scales. A plot of the Strehl for small errors is shown in Fig. 2.10.

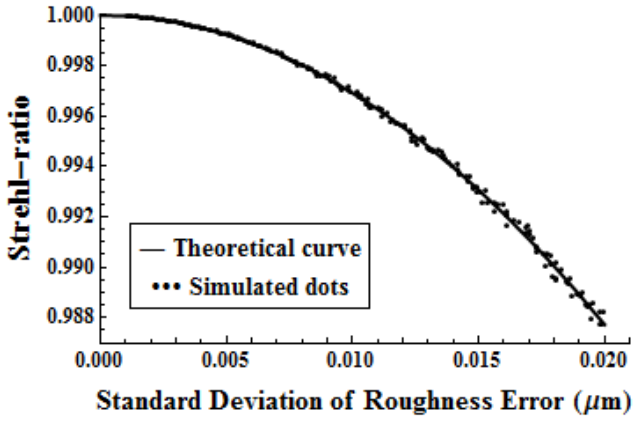

Fig. 2.10 The Strehl ratio as a function of the roughness error standard deviation.

The Maréchal approximation gives the Strehl ratio as the negative exponential of the phase variance $S = \exp(-\sigma_\phi^2)$, which is easily calculated. As Fig. 2.10 shows, the Strehl remains >0.99 provided that $\sigma_\varepsilon < 20\text{nm}$, so the roughness does not present a problem in terms of system performance.

Provided that the mean etch depth is accurate, a very-crude Strehl-ratio based estimation would suggest that we could tolerate up to 20nm random surface roughness before the random scattering errors exceeded 1%, so performance is driven by the accuracy of the mean etch depth and the flatness of the mean –surface profiles (any mean-value slopes would imply a grating blaze).

2.3.1.3 Plotting error

Our gratings are designed using AutoCAD/GDSII (see details in section 2.1.1) and the etch masks are made using a laser plotter, followed by a dry-etch of the fused silica. The binary masks are plotted with a 1μm resolution and typical grating periods are 25μm. Particularly in the case of the zone plates used to produce multi-focus images,

the curved features in the zone-plate are plotted in straight-line segments, which is a source of error.

Again we set up a mathematical model of the grating with plotting error (ignoring all the other errors here). The ideal grating consists of phase steps of a height characterized by a complex, unimodular number ε with an equal mark to space ratio. There are two transitions between mark and space per grating period – let odd-numbered transitions be from space to mark and even numbered transitions from mark to space. At each transition a plotting error takes the form of a top-hat function of width δ_j, centre $t_j + \frac{\delta_j}{2}$ and height $\varepsilon(-1)^j \operatorname{sgn}(\delta_j)$. Assume that δ_j is taken from a Normal distribution of zero mean and standard deviation σ.

Then the plotting error function is,

$$e(x) = \sum_j (-1)^j \operatorname{sgn}(\delta_j) \operatorname{rect}\left(x, jp, \frac{\delta_j}{2}\right) \tag{2.39}$$

where

$$\operatorname{rect}\left(x, jp, \frac{\delta_j}{2}\right) = \begin{cases} \varepsilon & \forall\ jp - \frac{\delta_j}{2} \le x < jp + \frac{\delta_j}{2} \\ 1 & \text{otherwise} \end{cases} \tag{2.40}$$

The length of the unit cell is $2p$, of which the interval $0 \le x < p$ has the value ε and the interval $p \le x < 2p$ has the value unity. The error function ensures that plotting errors with a mark are negative valued (eroding the mark) whilst those with a space are positive valued (augmenting the mark).

To analyse the effects of this we model the grating as the sum of an idealized phase grating plus an array of 'top hat' functions located at the transitions between the etched and un-etched regions and of positive- or negative-going nature dependent on whether the error represents an erosion of, or augments, the width of an etched region. The ideal grating structure and the error function are each Fourier transformed, summed and modulus squared in order to assess the effects of the plotting error. This model is amenable to numerical evaluation and for comparison with a computer simulation.

Similar to Eqs. (2.24) and (2.25), the scattered intensities of first 3 orders can be described as [6],

$$I_0 = \left|F(0)\right|^2 = \sum_j \mathrm{sgn}\left(\delta_j\right)\cdot\varepsilon^2{\delta_j}^2 \tag{2.41}$$

$$\begin{aligned} I_{\pm 1} &= \left|F\left(\frac{\pi}{p}\right)\right|^2 \\ &= \sum_j \mathrm{sgn}\left(\delta_j\right)\cdot\frac{\varepsilon^2 p^2}{\pi^2}\cdot\left(e^{-i\frac{\pi\delta_j}{p}}-1\right)^2 \\ &= \sum_j \mathrm{sgn}\left(\delta_j\right)\cdot\frac{\varepsilon^2 p^2}{\pi^2}\cdot\left(-i\frac{\pi\delta_j}{p}+\frac{\left(-i\frac{\pi\delta_j}{p}\right)^2}{2!}+\ldots\right)^2 \end{aligned} \tag{2.42}$$

Thus

$$\left|F\left(\frac{\pi}{p}\right)\right|^2 \sim \sum_j \mathrm{sgn}\left(\delta_j\right)\cdot\varepsilon^2{\delta_j}^2 \tag{2.43}$$

Please note that $\mathrm{sgn}(\delta_j)$ is just a sign label thus has no effect in the calculation (except in summing). For example, there is no phase shift in Fourier transform (or else $\mathcal{F}\{\mathrm{sgn}(x)\} = \frac{1}{j\pi f_x}$)

The results indicate that for a 25 μm period grating a 1 μm (or 0.5 μm) plotting error will lead to a variation of the relative energy scattered into each diffraction order with an average rms of 6.2% (or 1.6%). This error can be reduced by plotting the masks with higher precision, e.g. using electron-beam lithography. However, that is significantly more expensive than the laser-plotting here.

2.3.2 Optical system errors

As demonstrated in section 2.1.2, combining a QD grating with a conventional positive lens achieves multi-mode imaging by exploiting the well-known detour phase principle, i.e. that radiation scattered from a distorted diffraction grating suffers a phase change dependent on the local distortion of the grating and the diffraction order considered [24]. Each of the diffraction orders forms an image by virtue of the conventional lens.

The use of a QD grating to achieve simultaneous in-focus images of many specimen planes is greatly beneficial in terms of both imaging and photometric efficiency (see Fig. 2.3 and Fig. 2.5), but the related optical system errors induced from the grating are supposed to be investigated in order to find the crucial one(s) and therefore optimize it (them). Some of the typical system errors are explored in this subsection.

Fig. 2.3 shows a schematic of the optical relay. As discussed before, the QD grating is positioned one focal length behind the lens to form a 'telecentric' system so that all images have identical magnification without re-scaling. Here we use a re-imaging lens of f ~75mm focal length, so the total optical length of this system is ~300mm. Varying the grating period changes the separation of the images thus allowing full exploitation of any camera format. The ray-tracing work in this subsection was in collaboration with Dr. David Lee of UK Astronomy Technology Centre.

2.3.2.1 Mis-placing the QD grating

For 4D imaging, placing the QD grating one focal length behind the lens (Fig. 2.3) ensures that the images in all diffraction orders have equal magnification. The optics were modeled (Fig. 2.11) with Zemax ray-tracing software and include a bandpass filter limiting the wavelength range to 530±5nm, two 150mm achromatic lenses acting as a 1:1 relay, and the quadratically curved grating. The QD grating has a 1mm thick fused silica substrate, period 20μm, and a focal length of ±2m for diffraction orders ±1. The model includes an NA=0.6, ×40 microscope objective and tube lens not shown in Fig. 2.11. The object plane separation caused by the QD grating is ±2.9mm at the entrance to the relay optics equivalent to -1.86μm and +1.80μm at the specimen. For a 40x microscope objective, the beam entering the relay optics has a focal ratio of F/26. The predicted P-V wavefront error in the relay optics is less than 0.01 waves on-axis (zeroth order), and ~0.12 waves at the edges of the detector (±1st orders). The system is thus diffraction limited, with an Airy disk at focus ~34μm diameter (~5 Nyquist-spaced detector pixels). Magnification differences ~.25% between the images in the 3 diffraction orders are achievable experimentally using test objects on the microscope [20].

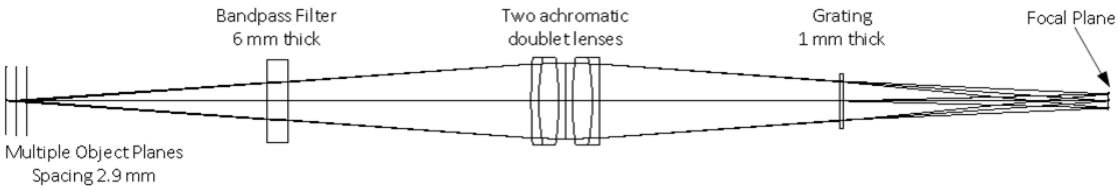

Fig. 2.11 Optical ray-trace diagram of the 4D imaging system.

2.3.2.2 Dispersion

The diffraction gratings are dispersive, i.e. the diffraction angle is wavelength dependent (see Eq. (1.5)), so chromatic effects degrade performance in the ±1st order images. Fig. 2.12 shows that the non-zero diffraction order images appear to be severely smeared laterally across the camera when a white light source from an unfiltered halogen bulb was used [4].

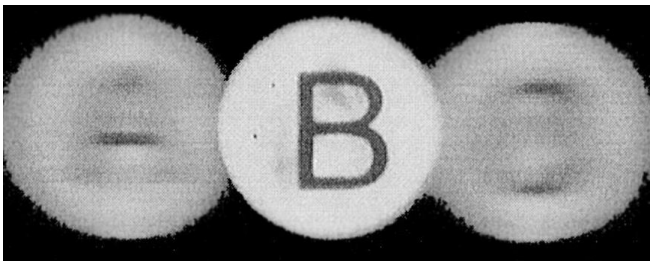

Fig. 2.12 Images of three object planes (as Fig. 2.3 demonstrated), where chromatic smearing of non-zero diffraction orders destroys the images of planes A and C [4].

The QD grating we use to perform multi-focus imaging has the property that the period varies across the transverse of the grating. The period that a beam 'goes through' is the grating period at the centre of the beam. To quantify the chromatic smearing effect we consider the case of two discrete wavelengths λ_1 and λ_2, where the grating periods at each beam centre are $d_{\lambda 1}$ and $d_{\lambda 2}$. We therefore can equalise the diffraction angle at these wavelengths (thus eliminate transverse smearing) when the following ratio yields [4],

$$\frac{d_{\lambda 1}}{\lambda_1} = \frac{d_{\lambda 2}}{\lambda_2} \tag{2.44}$$

Then we need to spectrally separate the input beam into its component wavelengths and spread these individual beams across the QD grating following the relationship

described as Eq. (2.44). Based on Eqs. (2.13) and (2.44), the separation between the two beams across the grating should be,

$$\Delta x = \frac{R^2}{2mW_{20}d_0}\left|\lambda_1 - \lambda_2\right| \tag{2.45}$$

Hence all wavelengths within a broadband beam dispersed across the QD grating can be re-arranged according to Eq. (2.45), such that the images at each wavelength will be accurately centred.

In practical use, over a 10nm bandwidth the peak position for the ±1st order images can move by one half of the width of a diffraction-limited spot (2-3 pixels for the system in Fig. 2.11). This chromatic smearing depends on the grating period, the focal length of the re-imaging lenses and the spectral profile used. In phase-contrast imaging, DIC (differential interference contrast) and dark-field imaging modes one can use a sufficiently-narrow band illumination that chromatic effects are negligible [20]. For fluorescent imaging the fluorophore bandpass may reach 30-50nm, and use of the full fluorescence spectrum is important to minimize photo-damage, so chromatic correction is required. For the instantaneous z-stack images the changing period of the QD grating structure may be used to correct the chromatic effects due to the wavelength-dependent angle of the diffraction orders.

Pre-dispersion of the light before it is incident on the QD grating can correct this chromatic smearing, even for unfiltered white light illumination, and a correction scheme has been demonstrated much earlier [4]. But this method used a pair of reflective gratings and a folded optical path to compensate for the chromatic distortion by introducing an opposing chromatic shear. The amount of chromatic shear is controlled by changing the distance between the gratings but, because of the folded path, changing the grating separation necessitates adjustments of the angle and/or position of various optical components. Adjusting these additional parameters complicates the control system, making it harder to integrate into user instrumentation and restricting practical application. Work is continuing to effect this chromatic correction in telecentric imaging and with high efficiency, and we have been exploring an optically and ergonomically-efficient correction, the details of which will be illustrated in Chapter 4.

2.3.2.3 Assessing focus

The Strehl ratio and the image sharpness [25] are both maximum for a diffraction - limited image. The Strehl is hard to measure experimentally but, as shown in Fig. 2.13, the Strehl and image sharpness maxima coincide accurately. In our experiments [5,6] we use the maximum image sharpness (equally applicable to extended incoherent sources) as an indicator of 'best focus'.

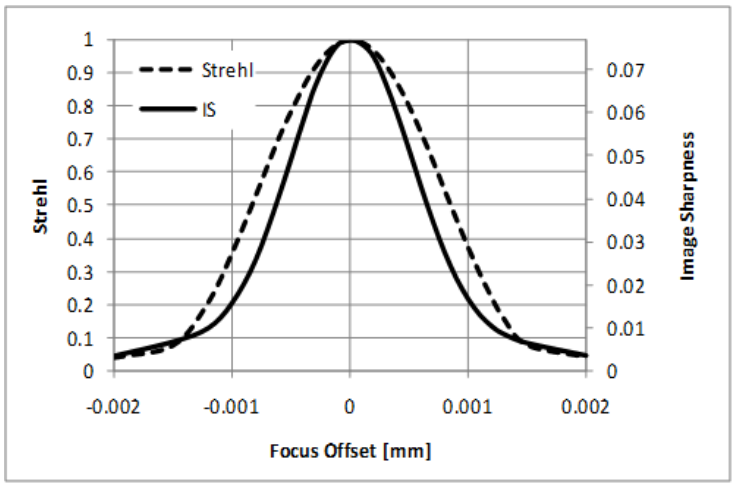

Fig. 2.13 Plot showing the through focus variation in Strehl ratio (dashed line) and image sharpness (IS - solid line) versus defocus at the microscope image plane.

These curves are produced from the Zemax software and model a displaced point source. The peak Strehl and image sharpness values occur at the optimum focus where the wavefront error is minimized. The image sharpness falls to 50% of its peak value when the P-V wavefront aberration reaches 0.34 waves – in this example at 0.65µm focus offset. This work was in collaboration with Dr. David Lee of UK Astronomy Technology Centre.

2.3.2.4 Spacing of the z-stack

The spacing of the axial foci is measured using the image sharpness and related back to a microscope specimen using the square of the magnification. Ray-tracing for catalogue lenses gives image-plane z-separation exceeding thin-lens calculations [3, 4, 9] by ~3.6%.

2.3.2.5 Image z-plane intensity variation

The QD grating moves the principal plane of the objective lens in the diffraction orders [9], slightly changing the numerical aperture (NA) for each plane in the 4D imaging

mode (objects closer to the objective are imaged with a slightly-higher NA). This effect was noted experimentally, and the observed changes are consistent with ray-tracing analysis. The induced flux variation in the multi-focal images can be ~4% percent, but is easily assessed from measurements.

2.3.2.6 Aberrations induced by optics

Deviations in the thickness of the cover slip from that for which the microscope objective was designed is the principal source of spherical aberration, but small amounts of additional spherical aberration and defocus are due to the interference filter and the substrate into which the QD grating has been etched. In addition, the use of diffraction by the QD grating to separate the images recorded in different image modes means that the images in the ±1st diffraction orders strike the camera at slight angles, and this breaking of the axial symmetry induces small amounts of coma aberration [3]. Ray-tracing analysis indicates that these effects reduce the Strehl in the ±1 diffraction-order images by less than 1% for monochromatic imaging.

2.3.3 Conclusions

We have discussed the principal sources of error and have assessed their significance using ray-tracing, theoretical analyses and computer simulations. The analysis presented shows that with achievable accuracies, the plotting error, the residual surface roughness, the thickness of the spectral filters and QD grating substrate, the misplacing of the grating and the delivery of images in the ±1st diffraction order do not produce significant image defects. We also find that the image sharpness is a good experimental measure to characterize 'best focus'. And the axial spacing and location of the in-focus images are altered slightly by the use of thick lenses and the aberrations introduced by other optics. The principal influence on the ability to balance the energy in the multi-focal images arises from the slight change in the NA of the imaging system between diffraction orders of the QD grating. For narrow-spectral bands the etch depth error dominates other errors, but the analysis here was in 1D and we expect this effect to be less in 2D QD gratings. The most serious error in fluorescence imaging arises from the wavelength-dependent diffraction angle of the ±1st diffraction orders. In multi-focal imaging this effect may be largely corrected by pre-dispersing the light before it strikes the QD grating, however work at this stage continues to find a telecentric and high-efficiency implementation of this.

2.4 Summary

In this chapter we have demonstrated that a QD grating in the form of an off-axis zone-plate imposes a different curvature on the incident wavefront in each diffraction order. Combined with a conventional positive lens, this provides multiple in-focus images on a single detector in which each diffraction order focuses on a different specimen depth. The system thus provides a 'z-stack' with no need for mechanical scanning and with the advantage that images at all depths are recorded during a single integration time.

However, maximizing the optical efficiency and improving the image quality are crucial in most modern microscope imaging applications. When using QD grating, the first challenge is to maximize photometric efficiency in the usable diffraction orders, by reducing the intensity in the unused higher orders, without compromising QD grating performance or functionality; the second challenge is to diminish chromatic aberration induced in non-zero diffraction orders of QD grating.

Based on principles of Fourier optics, it has been proved that the grating efficiency could be optimized by multi-etch fabrication. 1D mathematical models of multi-level phase grating with balanced intensity distribution between first 3 diffraction orders have been established, which illustrate that 4.4% efficiency gain is obtained by double-etch than that of single etch grating. However, efficiency gain from a third etch is only 0.4%, which looks sufficiently surprising that some more investigation about the efficiency of multi-etch grating should be essential. Hence we may say that improved efficiency is desirable (the efficiency of single etch grating is about 84% in practical experiments) but not essential at present, and it should not worth doing more than 2 etches for a 4D imaging system. For the long term, any process that allows the production of a continuous surface profile (grey level rather than discrete levels), or very precise alignment of etches on the same side of the substrate (alignment better than about 2 microns), would offer new opportunities, but we presently have no plans to attempt this level of sophistication.

In order to assess the influence of errors and thus find significant ones to mitigate a comprehensive error budget, in the form of theoretical analyses, computer simulations and ray-tracing, has been established. It seems that etch depth error dominates other fabrication errors, yet only a very rough 1D mathematical model of phase grating (which is similar with Fig. 2.4) was built. In my practice of telecentric cases, the

relative positions of in-focus object planes in each diffraction order, i.e. Δz value between A, B and B, C separately (see Fig. 2.3), are never identical (sometimes even not close enough) and considerably deviate from the theoretical value (see Eqs. (2.15), (2.16) and (2.18)). Prof. Greenaway, who is the co-inventor of the QD grating-based optical system, supposed that that might be induced by system error(s), i.e. spherical aberration and/or misplacing the QD grating such that a nominal telecentric relay was delivered. Actually, besides the significance of Δz values for the reconstruction of 4D images, there should be a few other parameters to be carefully considered. Therefore the ultimate approach to estimate and/or eliminate the theoretical error(s) is formulating an ideal 2D grating model with more details in terms of the quadratic curvature and gradually varied periods. In this dissertation, we first develop a 2D theoretical model of QD grating, which will be demonstrated in Chapter 3. And this delicate 2D model may be applied in more sophisticated design of both (crossed) QD grating and 4D imaging system in the future.

In addition to the fabrication error, the chromatic aberration generated by the QD grating has been proved to be the significant error in 4D imaging system. We have had found that grisms, a grating and prism combination, are a simple way to achieve chromatic control in 4D imaging [6, 26]. However, the whole imaging system was ~1.3 metres long and, the imaging system was quite difficult to align and thus not compatible with microscope. Accordingly only the image of a single diffraction order can be recorded in each snapshot. Having identified and quantified the properties and/or defects of our current grisms, my work continues to optimize the design of grism, by means of geometrical optics analyses, minor changes of the grism structure, customization of new grisms as well as their mounts, etc. Some simulated experiments are also followed to assess the practical capacities of new grisms. The full details will be provided in Chapter 4.

2.5 References

[1] P. M. Blanchard, D. J. Fisher, S. C. Woods and A. H. Greenaway, *Phase-diversity wave-front sensing with a distorted diffraction grating*. Applied Optics **39**(35), 6649-6655 (2000).

[2] P. M. Blanchard and A. H. Greenaway, *Multiplane imaging and wavefront sensing using distorted diffraction gratings*. Paper presented at Trends in Optics and Photonics. Diffractive Optics and Micro-Optics. Vol.41. Technical Digest. Postconference Edition, Quebec City, Canada:Opt. Soc. America. p. 250-252, 18-22 June (2000).

[3] P. M. Blanchard and A. H. Greenaway, *Simultaneous multiplane imaging with a distorted diffraction grating*. Applied Optics **38**(32), 6692-6699 (1999).
[4] P. M. Blanchard and A. H. Greenaway, *Broadband simultaneous multiplane imaging*. Optics Communications **183**(1), 29-36 (2000).
[5] A. H. Greenaway and P. M. Blanchard, *Three-dimensional imaging system*. in United States Patent No. 6,975,457 B1. Application No. 09/622,405, (QinetiQ Limited, London, 2005).
[6] Y. Feng, *Optimization of phase gratings with applications to 3D microscopy imaging*, A dissertation for the degree of Doctor of Philosophy, Precision Instruments and Machinery, University of Science and Technology of China, Hefei, China (2013).
[7] M. Born and E. Wolf, *Principles of optics*. Cambridge University Press, Cambridge, Corrected reprint of the 7th edition, (2001).
[8] E. Hecht, *Optics*. Pearson Education, Addison Wesley, San Francisco, 4th edition (International edition), (2002).
[9] S. Djidel, J. K. Gansel, H. I. Campbell and A. H. Greenaway, *High-speed, 3-dimensional, telecentric imaging*. Optics Express **14**(18), 8269-8277 (2006).
[10] C. A. Palmer, E. G. Loewen and R. Thermo, *Diffraction grating handbook*. Newport Corporation Springfield, OH, 6th edition, (2005).
[11] J. W. Strutt and L. Rayleigh, *XXV. On the manufacture and theory of diffraction-gratings*. Philosophical Magazine **47**(311), 193-205 (1874).
[12] K. M. Flood, J. M. Finlan and R. J. Bojko, *Multiple phase level computer-generated holograms etched in fused silica*. Paper presented at OE/LASE'89, Los Angeles CA, International Society for Optics and Photonics 15-20 January (1989).
[13] E. Hasman, N. Davidson and A. Friesem, *Heterostructure multilevel binary optics*. Optics Letters **16**(19), 1460-1462 (1991).
[14] Y. Feng, H. I. C. Dalgarno, P. Dalgarno and A. H. Greenaway, *High efficiency 3D imaging using diffractive optical elements*. Paper presented at The 15th European Microscopy Congress, Manchester, 16th - 21st September (2012).
[15] J. W. Goodman, *Introduction to Fourier optics*. Roberts and Company Publishers, 3rd edition, (2005).
[16] D. Rogers, *Fifty years of Monte Carlo simulations for medical physics*. Physics in Medicine and Biology **51**(13), R287 (2006).
[17] M. Kumar, M. Husian, N. Upreti and D. Gupta, *Genetic algorithm: Review and application*. International Journal of Information Technology and Knowledge Management **2**(2), 451-454 (2010).
[18] S. Kirkpatrick and M. Vecchi, *Optimization by simmulated annealing*. Science **220**(4598), 671-680 (1983).
[19] D. Bertsimas and J. Tsitsiklis, *Simulated annealing*. Statistical Science **8**(1), 10-15 (1993).
[20] Y. Feng, L. Scholz, D. Lee, H. Dalgarno, D. Foo, L. Yang, W. Lu and A. Greenaway, *Multi-mode microscopy using diffractive optical elements*. Engineering Review **31**(2), 133-139 (2011).
[21] T. S. Ross, *Limitations and applicability of the Maréchal approximation*. Applied Optics **48**(10), 1812-1818 (2009).
[22] D. J. Schroeder, *Astronomical optics*. Academic press, San Diego, 2nd edition, (2000).
[23] V. N. Mahajan, *Zernike annular polynomials for imaging systems with annular pupils*. Journal of the Optical Society of America **71**(1), 75-85 (1981).
[24] J. Bucklew and N. Gallagher Jr, *Detour phase error in the Lohmann hologram*. Applied Optics **18**(4), 575-580 (1979).

[25] R. A. Muller and A. Buffington, *Real-time correction of atmospherically degraded telescope images through image sharpening*. Journal of the Optical Society of America **64**(9), 1200-1210 (1974).

[26] Y. Feng, P. A. Dalgarno, D. Lee, Y. Yang, R. R. Thomson and A. H. Greenaway, *Chromatically-corrected, high-efficiency, multi-colour, multi-plane 3D imaging*. Optics Express **20**(18), 20705-20714 (2012).

Chapter 3

Fraunhofer diffraction at the two-dimensional QD grating

Preface

Due to the high level of sophistication in modelling the 2D QD grating, in the past a rough 1D model was applied for some basic design, i.e. the optimization of optical efficiency and estimation of etch depth error as illustrated in Chapter 2. In order to explore accurate properties of QD grating, the characteristic quadratic curvature and chirped-period should not be simplified as the 1D equidistant slits (see Fig. 2.4). In this chapter we establish a delicate mathematical model of 2D QD grating, derive the analytical expression of Fourier spectrum, and finally obtain the numerical solution of 'working' phase which is one of the key parameters in grating fabrication. Since the 2D QD grating model is first developed, a few verifications are performed. Based on this mathematical model, further investigations regarding to the design and optimization of both QD grating and 4D multi-colour microscopy imaging (MCMI) system will be considered in the future.

3.1 The analytical model of the 2D QD grating

It has been proved that the scalar diffraction theory can be utilized for evaluating the image formed with a source of natural light by an optical system of moderate numerical aperture, thus an approximate description in terms of a single complex scalar wave function is adequate to describe most problems encountered in optics [1]. The further approximations, which are referred to as *Fresnel* and *Fraunhofer* approximations, have greatly simplified the calculations of diffraction patterns under certain conditions. Before establishing the analytical model of the 2D QD grating, some initial diffraction theory derivations with respect to these approximations that form the basis of our mathematical model are introduced first. Please note that the content mentioned in subsection 3.1.1 is based on *'Born and Wolf'* [1] and this reference will not be frequently marked to make the context tidy.

3.1.1 Introduction to the derivation of Fraunhofer diffraction theory

Based on the scalar diffraction theory, a monochromatic scalar light can be described by the function of the complex amplitude $U(x, y, z)$ which satisfies the *Helmholtz equation*,

$$(\nabla^2 + k^2)U = 0 \tag{3.1}$$

where $k = \frac{2\pi}{\lambda}$ is the *wave number* and λ the incident wavelength.

Solving Eq. (3.1) by Green's theorem, we have a form of the *integral theorem of Helmholtz and Kirchhoff,*

$$U(P) = \frac{1}{4\pi}\iint_S \left[U \frac{\partial}{\partial n}\left(\frac{e^{iks}}{s}\right) - \frac{e^{iks}}{s}\frac{\partial U}{\partial n} \right] \mathrm{d}S \tag{3.2}$$

where P represents any point within a closed surface S, U is assumed to be continuous and partial differentiable up to the second order within and on S, $\frac{\partial}{\partial n}$ denotes differentiation along the inward normal to S, and s is the distance from P to the element dS.

According to *Kirchhoff's boundary conditions*, which are the basis of Kirchhoff's diffraction theory (see Eq.15-16 of Chapter 8.3.2 and Fig.8.3 in reference [1]), and abandoning the strict monochromaticity, the *Fresnel-Kirchhoff diffraction formula* can be obtained,

$$U(P) = -\frac{iA}{2\lambda}\iint_{\mathcal{A}} \frac{e^{ik(r+s)}}{rs}\left[\cos(n,r) - \cos(n,s)\right] \mathrm{d}S \tag{3.3}$$

where $\mathcal{A}$ could be any open surface, of which the rim coincides with the edge of the aperture; A is a constant, λ is the incident wavelength, r and s are the distances from a point Q in the aperture to the point source P_0 and observation point P respectively (see Fig. 3.1), n denotes the normal to the aperture.

A Cartesian system is then established, with origin in the aperture and the x- and y-axes in the plane of the aperture, and the positive z direction is chosen to point into the half-space that contains the observation point P, as shown in Fig. 3.1.

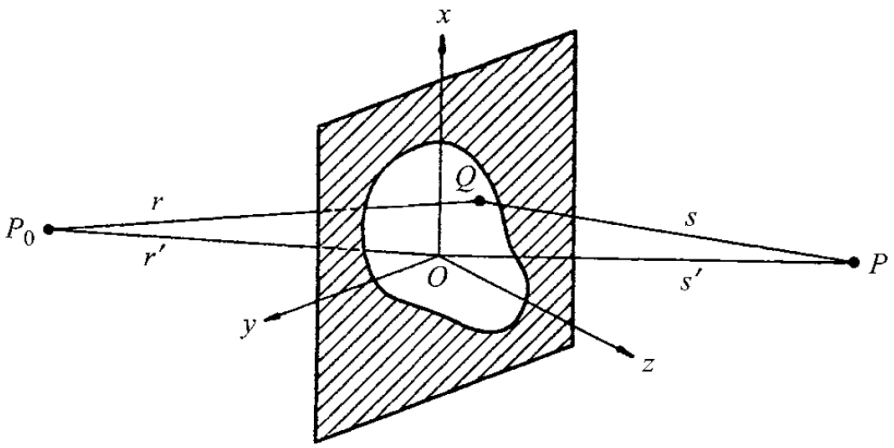

Fig. 3.1 Diffraction at an aperture in a plane screen [1].

With some reasonable approximations, $2\cos\delta$ could be applied instead of the factor $\left[\cos(n,r)-\cos(n,s)\right]$, where δ is the angle between the line P_0P and the normal to the screen; and the factor $1/rs$ could be replaced by $1/r's'$, where r' and s' are the distance of P_0 and P from the origin. Thus Eq. (3.3) reduces to,

$$U(P)\sim-\frac{Ai}{\lambda}\frac{\cos\delta}{r's'}\iint_{\mathcal{A}}e^{ik(r+s)}\,\mathrm{d}S \tag{3.4}$$

It is assumed that the linear dimensions of the aperture are small compared to both r' and s', then we may have,

$$\left.\begin{aligned} r &\sim r'-\frac{x_0\xi+y_0\eta}{r'}+\frac{\xi^2+\eta^2}{2r'}-\frac{\left(x_0\xi+y_0\eta\right)^2}{2r'^3}-\cdots,\\ s &\sim s'-\frac{x\xi+y\eta}{s'}+\frac{\xi^2+\eta^2}{2s'}-\frac{\left(x\xi+y\eta\right)^2}{2s'^3}-\cdots. \end{aligned}\right\} \tag{3.5}$$

where (x_0, y_0, z_0) and (x, y, z) are the coordinates of P_0 and of P respectively, and (ξ, η) the coordinates of a point Q in the aperture.

Substitution from Eq. (3.5) into Eq. (3.4) gives,

$$U(P)=-\frac{i\cos\delta}{\lambda}\frac{Ae^{ik(r'+s')}}{r's'}\iint_{\mathcal{A}}e^{ikf(\xi,\eta)}\,\mathrm{d}\xi\mathrm{d}\eta \tag{3.6}$$

where

$$f(\xi,\eta)=-\frac{x_0\xi+y_0\eta}{r'}-\frac{x\xi+y\eta}{s'}+\frac{\xi^2+\eta^2}{2r'}+\frac{\xi^2+\eta^2}{2s'}-\frac{\left(x_0\xi+y_0\eta\right)^2}{2r'^3}-\frac{\left(x\xi+y\eta\right)^2}{2s'^3}\cdots \quad (3.7)$$

If we denote by (l_0, m_0) and (l, m) the first two direction cosines,

$$\left.\begin{aligned} l_0&=-\frac{x_0}{r'},\ l=\frac{x}{s'},\\ m_0&=-\frac{y_0}{r'},\ m=\frac{y}{s'},\end{aligned}\right\} \quad (3.8)$$

So Eq. (3.7) can be written in the form,

$$f(\xi,\eta)=\left(l_0-l\right)\xi+\left(m_0-m\right)\eta+\frac{1}{2}\left[\left(\frac{1}{r'}+\frac{1}{s'}\right)\left(\xi^2+\eta^2\right)-\frac{\left(l_0\xi+m_0\eta\right)^2}{r'}-\frac{\left(l\xi+m\eta\right)^2}{s'}\right]\cdots \quad (3.9)$$

Then the problem of determining the light disturbance at P has been reduced to the evaluation of the integral (3.6). When the quadratic and higher-order terms in ξ and η could be neglected in f, the case is the so-called *Fraunhofer diffraction*; otherwise *Fresnel diffraction* would be performed when the quadratic terms cannot be neglected. Further investigations reveal the certain conditions of Fraunhofer diffraction,

$$|r'|\gg\frac{\left(\xi^2+\eta^2\right)_{\max}}{\lambda}\ \text{ and }\ |s'|\gg\frac{\left(\xi^2+\eta^2\right)_{\max}}{\lambda} \quad (3.10)$$

or

$$\frac{1}{r'}+\frac{1}{s'}=0\ \text{ and }\ l_0^2,m_0^2,l^2,m^2\ll\frac{|r'|\lambda}{\left(\xi^2+\eta^2\right)_{\max}} \quad (3.11)$$

Conditions (3.10) is used to estimate the distances r' and s' for determining whether the Fraunhofer diffraction could be applied, whereas conditions (3.11) imply that Fraunhofer diffraction could also occur when the observation point is situated in a plane parallel to that of the aperture, provided that both the observation point and the source are sufficiently close to the z-axis.

In the case of Fraunhofer diffraction, the factors, l_0, m_0, l and m, enter Eq. (3.9) only in the combinations,

$$p = l - l_0, \qquad q = m - m_0 \tag{3.12}$$

Hence the evaluation of Fraunhofer diffraction could be written as a Fourier integral,

$$U(p,q) = \iint G(\xi,\eta)\, e^{-\frac{2\pi i}{\lambda}(p\xi+q\eta)} \mathrm{d}\xi \mathrm{d}\eta \tag{3.13}$$

where the integral extends over the whole ξ-η plane, and $G(\xi, \eta)$ the pupil function is given by,

$$G(\xi,\eta) = \begin{cases} \text{constant} & \text{at points in the opening} \\ 0 & \text{at points outside the opening} \end{cases} \tag{3.14}$$

3.1.2 Definition of the analytical model of 2D QD grating

For a compound imaging system comprised of QD grating and 2*f*:2*f* relay lens discussed in Chapter 2 (see Fig. 2.3 and Fig. 2.11), the diffraction limited optical state is approaching the far-field conditions of Fraunhofer diffraction (Eq. (3.10)). Hence the complex field distribution across the Fraunhofer diffraction pattern can be simply obtained by the Fourier transform of the aperture distribution, i.e. the groove profile of QD grating, as implied by Eq. (3.13). And consequently, the scattered image intensity can be calculated by the modulus squared of the Fourier spectrum.

Now attention has been focused on the Fourier transform of the QD grating profile. As Fig. 2.1 shown, the QD grating is characterised by a diffractive structure with the quadratic curvature and gradually varied periodic phase relief. For simplicity, we designed the QD grating based on a very rough one-dimensional model as illustrated in section 2.2.1, in which a single period of grating unit (as shown in Fig. 2.4) was replicated in the calculation such that the period of the 1D grating remained unchanged instead of the chirped-period of QD grating. Moreover, the 1D model restricts the analysis of the effect(s) induced by the particular 2D profile such as quadratic grooves. Therefore an analytical 2D model of QD grating should be investigated, although it might seem of more theoretical than practical interest at the early stage.

Before presenting the analytical model of QD grating, at first glance, we consider a more straightforward and logical way to do the Fourier transform — taking the structure of QD grating as the pupil function $G(\xi, \eta)$ and working out the Fourier spectrum by Eq.

(3.13). In principle, we may produce a 'circular window' in a Fresnel zone plate (see Fig. 2.1 for details) to form a QD grating and the field strength caused by the QD grating would be obtained if both a high-performance computer and considerable running time were implemented. In practice, however, an alternative solution based on the Fourier transform of a single circular sector (as Fig. 3.4 shown) will be proposed.

To establish the analytical model of 2D QD grating described in Chapter 2 [2, 3], a set of concentric circular sectors with varied radii have been defined, thus a series of annular slits can be produced by the subtraction of adjacent sectors. Then the Fourier transform of the whole QD grating can be represented by summing up the Fourier spectra of annular slits according to the *Linearity theorem* of Fourier transform [4]. As shown in Fig. 3.2, the annular slits behave as a QD grating with radius R and, for the purpose of integral calculations, the wedge angle corresponding to each arc is denoted by δ_j, where j is an integer varies from negative to positive values which depends on the loci of each grating arc (see Eq. (2.11) for details). Consequently, the bounds of the Fourier integral (Eq. (3.13)), which may be regarded as one of the most complicated elements in the calculations, can be effectively replaced by much more general bounds of a single sector. Here we suppose that the effect of the marginal fractions, which is generated by the subtraction of adjacent sectors, could be neglected due to their limited contribution to the diffraction images. The detailed calculations will be demonstrated in the following sections.

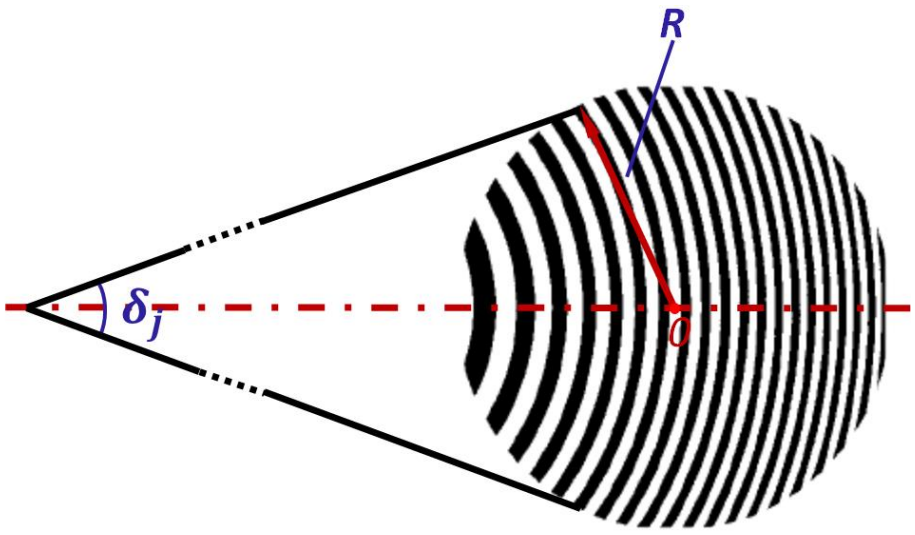

Fig. 3.2 Schematic of geometric model of QD grating comprising a series of annular slits, which covers a circular area with radius R.

As discussed above, the analytical process of modelling the 2D QD grating could be diagrammed as Fig.3.3 (excluding the phase set step, amplitude grating can be modelled following the same procedure). It should be pointed out that in the last step before obtaining the final spectrum of grating, the phase change between the adjacent zones can be easily modified, which allows us to explore the phase properties of QD grating more flexibly.

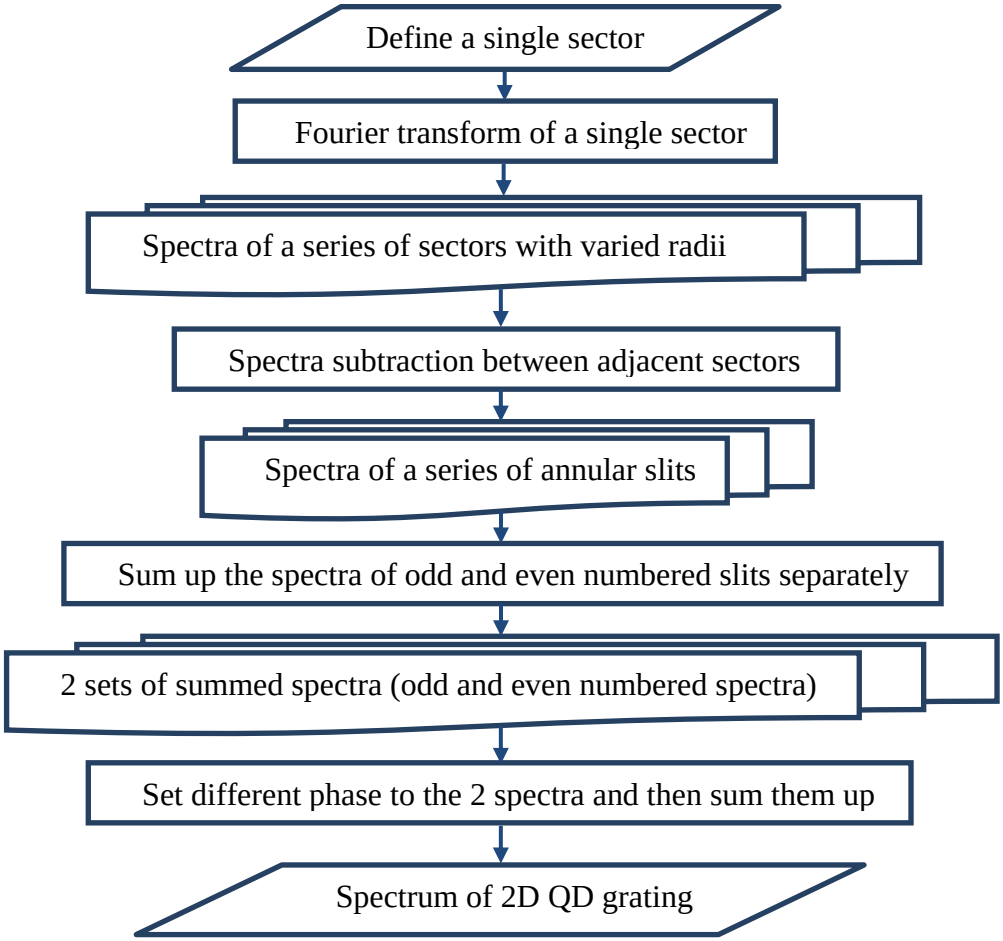

Fig.3.3 Analytical process of 2D QD phase grating modelling.

3.2 Two-dimensional Fraunhofer diffraction spectrum of the QD grating

3.2.1 Fraunhofer diffraction at a single circular sector

Eqs. (3.13) and (3.14) illustrate that the evaluation of Fraunhofer diffraction, which presents the total light disturbance at an arbitrary point (p, q), could be expressed as a Fourier integral. Attention is now turned to a certain pupil function, the single circular sector, as indicated in Fig. 3.4.

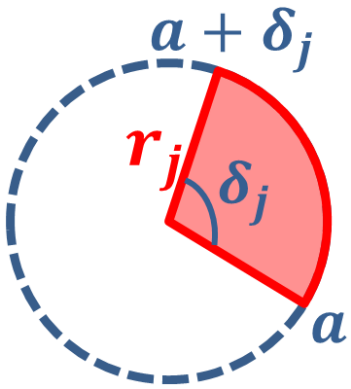

Fig. 3.4 A single circular sector.

Now we make a transformation to polar coordinate system in both the (ξ, η) and the (p, q) planes, and let (r, θ) and (ρ, φ) be the polar coordinates of a typical point in the aperture and diffraction pattern respectively as follows,

$$\begin{aligned} r &= \sqrt{\xi^2+\eta^2} & \xi &= r\cos\theta \\ \theta &= \arctan\left(\frac{\eta}{\xi}\right) & \eta &= r\sin\theta \\ \rho &= \sqrt{p^2+q^2} & p &= \rho\cos\varphi \\ \varphi &= \arctan\left(\frac{q}{p}\right) & q &= \rho\sin\varphi \end{aligned} \tag{3.15}$$

Aside from the constants preceding the integral, the Fraunhofer diffraction spectrum of a single circular sector (simply *'pie'* for short) could be expressed in the form of Fourier transform, thus in polar coordinates the Fraunhofer diffraction (3.13) can be written as [4],

$$\begin{aligned} \mathcal{F}\{pie\} &= \frac{e^{ikz}e^{i\frac{k}{2z}\rho^2}}{i\lambda z}\int_0^{+\infty}\int_a^{\delta_j+a}\text{sector}\left(r_j\right)e^{-i\frac{2\pi}{\lambda z}\rho r\cos(\theta-\varphi)}r\,dr\,d\theta \\ &= \frac{e^{ikz}e^{i\frac{k}{2z}\rho^2}}{i\lambda z}\int_0^{r_j}\int_a^{\delta_j+a}e^{i\frac{2\pi}{\lambda z}\rho r\sin(\theta-\varphi-\frac{\pi}{2})}r\,dr\,d\theta \end{aligned} \tag{3.16}$$

where $k=\dfrac{2\pi}{\lambda}$ is the number of waves, z the observation distance between aperture and image plane, a the start point of the sector, λ the wavelength of incident light, δ_j the wedge angle of the jth sector, r_j the varying radii, and as preceding notations, j an integer varies from negative to positive values which depends on the loci of each grating

arc (see Eq. (2.11) for details). Here the Fourier transform of the *'pie'* aperture distribution is evaluated at frequencies,

$$f_P = \frac{p}{\lambda z}, \quad f_Q = \frac{q}{\lambda z} \tag{3.17}$$

Noting that if the aperture is illuminated by a normally incident, unit-amplitude and monochromatic plane wave, then the field distribution across the aperture is equal to the transmittance function (a constant of 1 in this case).

To make the calculation process clearer, we devote special attention to work out the integral kernel (marked as 'ker') of Eq. (3.16) first,

$$\text{ker} = \int_0^{r_j} \int_a^{\delta_j + a} e^{i\frac{2\pi}{\lambda z}\rho r \sin(\theta - \varphi - \frac{\pi}{2})} r \mathrm{d}r\mathrm{d}\theta \tag{3.18}$$

This equation, which neglects the multiplicative phase factors preceding the integral (3.16), will serve as the base of our following calculation in this section.

Before solving Eq. (3.18), we may introduce the *Jacobi–Anger expansion*, which is an expansion of exponentials of trigonometric functions, as the following formula [5],

$$e^{i\beta \sin\theta} = \sum_{n=-\infty}^{+\infty} J_n(\beta) e^{in\theta} \tag{3.19}$$

where J_n is first kind *Bessel function* of order n.

Accordingly the integral kernel (3.18) is found to be,

$$\begin{aligned} \text{ker} &= \int_0^{r_j} \int_a^{\delta_j + a} \sum_{n=-\infty}^{+\infty} J_n\left(\frac{2\pi}{\lambda z}\rho r\right) e^{in(\theta - \varphi - \frac{\pi}{2})} r \mathrm{d}r\mathrm{d}\theta \\ &= \sum_{n=-\infty}^{+\infty} \int_0^{r_j} J_n\left(\frac{2\pi}{\lambda z}\rho r\right) r \mathrm{d}r \int_0^{\delta_j} e^{in(\theta + a - \varphi - \frac{\pi}{2})} \mathrm{d}\theta \end{aligned} \tag{3.20}$$

When $n = 0$, Eq. (3.20) can be simplified to,

$$\ker_{n=0} = \int_0^{r_j} J_0\left(\frac{2\pi}{\lambda z}\rho r\right) r\mathrm{d}r \cdot \delta_j \tag{3.21}$$

And according to the following property of first kind Bessel function,

$$\int_0^x \xi\ J_0(\xi)\mathrm{d}\xi = xJ_1(x) \tag{3.22}$$

we can derive the solution of integral kernel (3.20) under the condition of n=0,

$$\begin{aligned}\ker_{n=0} &= \frac{1}{\left(\frac{2\pi}{\lambda z}\rho\right)^2}\int_0^{\frac{2\pi}{\lambda z}\rho r_j} \frac{2\pi}{\lambda z}\rho r \cdot J_0\left(\frac{2\pi}{\lambda z}\rho r\right)\mathrm{d}\left(\frac{2\pi}{\lambda z}\rho r\right)\cdot\delta_j \\ &= \frac{\delta_j \lambda z r_j}{2\pi\rho} J_1\left(\frac{2\pi}{\lambda z}\rho r_j\right)\end{aligned} \tag{3.23}$$

An alternative, which should be more general, is the condition that n is a nonzero integer. Then Eq. (3.20) can be re-written as,

$$\begin{aligned}\ker_{n\neq 0} &= \sum_{n=-\infty, n\neq 0}^{+\infty}\int_0^{r_j} J_n\left(\frac{2\pi}{\lambda z}\rho r\right) r\mathrm{d}r \int_0^{\delta_j} e^{in(\theta+a-\varphi-\frac{\pi}{2})}\mathrm{d}\theta \\ &= \sum_{n=-\infty, n\neq 0}^{+\infty} \frac{1}{\left(\frac{2\pi}{\lambda z}\rho\right)^2}\int_0^{\frac{2\pi}{\lambda z}\rho r_j} rJ_n(r)\mathrm{d}r \cdot \int_0^{\delta_j} e^{in(\theta+a-\varphi-\frac{\pi}{2})}\mathrm{d}\theta\end{aligned} \tag{3.24}$$

For the first kind Bessel function of integer order n, we have the identity,

$$J_{-n}(t) = (-1)^n J_n(t) \tag{3.25}$$

Thus when n is a negative integer, the series (3.24) could be expressed as,

$$\begin{aligned}&\sum_{n=-\infty}^{-1} \frac{1}{\left(\frac{2\pi}{\lambda z}\rho\right)^2}\int_0^{\frac{2\pi}{\lambda z}\rho r_j} rJ_n(r)\mathrm{d}r \cdot \int_0^{\delta_j} e^{in(\theta+a-\varphi-\frac{\pi}{2})}\mathrm{d}\theta \\ &= \sum_{n=1}^{+\infty} \frac{1}{\left(\frac{2\pi}{\lambda z}\rho\right)^2}\int_0^{\frac{2\pi}{\lambda z}\rho r_j} rJ_n(r)\mathrm{d}r \cdot \int_0^{\delta_j} (-1)^n e^{-in(\theta+a-\varphi-\frac{\pi}{2})}\mathrm{d}\theta\end{aligned} \tag{3.26}$$

Therefore when n is a nonzero integer, our derivation of integral kernel (3.20) becomes,

$$\begin{aligned}
&\ker_{n\neq 0} \\
&= \sum_{n=-\infty}^{-1} \frac{1}{\left(\frac{2\pi}{\lambda z}\rho\right)^2} \int_0^{\frac{2\pi}{\lambda z}\rho r_j} rJ_n(r)\,\mathrm{d}r \cdot \int_0^{\delta_j} e^{in(\theta+a-\varphi-\frac{\pi}{2})}\,\mathrm{d}\theta + \sum_{n=1}^{+\infty} \frac{1}{\left(\frac{2\pi}{\lambda z}\rho\right)^2} \int_0^{\frac{2\pi}{\lambda z}\rho r_j} rJ_n(r)\,\mathrm{d}r \cdot \int_0^{\delta_j} e^{in(\theta+a-\varphi-\frac{\pi}{2})}\,\mathrm{d}\theta \\
&= \sum_{n=1}^{+\infty} \frac{1}{\left(\frac{2\pi}{\lambda z}\rho\right)^2} \int_0^{\frac{2\pi}{\lambda z}\rho r_j} rJ_n(r)\,\mathrm{d}r \cdot \int_0^{\delta_j} \left[e^{in(\theta+a-\varphi-\frac{\pi}{2})} + (-1)^n e^{-in(\theta+a-\varphi-\frac{\pi}{2})} \right] \mathrm{d}\theta
\end{aligned} \tag{3.27}$$

We now consider two cases —either n is even or odd number, to work out Eq. (3.27) separately. Let m denote an arbitrary non-zero integer, hence when n is an even number the integral (3.27) takes on the form,

$$\begin{aligned}
&\ker_{n=2m\ \&\ n\neq 0} \\
&= \sum_{m=1}^{+\infty} \frac{1}{\left(\frac{2\pi}{\lambda z}\rho\right)^2} \int_0^{\frac{2\pi}{\lambda z}\rho r_j} rJ_{2m}(r)\,\mathrm{d}r \cdot \int_0^{\delta_j} \left[e^{i2m(\theta+a-\varphi-\frac{\pi}{2})} + e^{-i2m(\theta+a-\varphi-\frac{\pi}{2})} \right] \mathrm{d}\theta \\
&= \sum_{m=1}^{+\infty} \frac{2\cdot(-1)^m}{m\cdot\left(\frac{2\pi}{\lambda z}\rho\right)^2} \sin(m\delta_j) \cos(m\delta_j - 2m\varphi + 2ma) \int_0^{\frac{2\pi}{\lambda z}\rho r_j} rJ_{2m}(r)\,\mathrm{d}r
\end{aligned} \tag{3.28}$$

Alternatively when n is an odd number,

$$\begin{aligned}
&\ker_{n=2m-1\ \&\ n\neq 0} \\
&= \sum_{m=1}^{+\infty} \frac{1}{\left(\frac{2\pi}{\lambda z}\rho\right)^2} \int_0^{\frac{2\pi}{\lambda z}\rho r_j} rJ_{2m-1}(r)\,\mathrm{d}r \cdot \int_0^{\delta_j} \left[e^{i(2m-1)(\theta+a-\varphi-\frac{\pi}{2})} - e^{-i(2m-1)(\theta+a-\varphi-\frac{\pi}{2})} \right] \mathrm{d}\theta \\
&= \sum_{m=1}^{+\infty} \frac{4\cdot(-1)^m\cdot i}{(2m-1)\left(\frac{2\pi}{\lambda z}\rho\right)^2} \sin\left[\frac{(2m-1)\delta_j}{2}\right] \cos\left[\frac{(2m-1)(\delta_j+2a-2\varphi)}{2}\right] \int_0^{\frac{2\pi}{\lambda z}\rho r_j} rJ_{2m-1}(r)\,\mathrm{d}r
\end{aligned} \tag{3.29}$$

The main problem accordingly turns to be resolving the integrals $\int_0^{\frac{2\pi}{\lambda z}\rho r_j} rJ_{2m}(r)\mathrm{d}r$ and $\int_0^{\frac{2\pi}{\lambda z}\rho r_j} rJ_{2m-1}(r)\mathrm{d}r$. It has been proved that [6],

$$\int_0^x t^{\mu}J_{\nu}(t)\mathrm{d}t = x^{\mu}\frac{\Gamma\left(\frac{1}{2}\nu+\frac{1}{2}\mu+\frac{1}{2}\right)}{\Gamma\left(\frac{1}{2}\nu-\frac{1}{2}\mu+\frac{1}{2}\right)}\sum_{k=0}^{+\infty}\frac{(\nu+2k+1)\Gamma\left(\frac{1}{2}\nu-\frac{1}{2}\mu+\frac{1}{2}+k\right)}{\Gamma\left(\frac{1}{2}\nu+\frac{1}{2}\mu+\frac{3}{2}+k\right)}J_{\nu+2k+1}(x) \quad (3.30)$$

which leads to the expressions as following,

$$\int_0^{\frac{2\pi}{\lambda z}\rho r_j} r\cdot J_{2m}(r)\mathrm{d}r = \frac{2\pi}{\lambda z}\rho r_j \cdot m\sum_{k=0}^{+\infty}\frac{2m+2k+1}{(m+k)(m+k+1)}J_{2m+2k+1}\left(\frac{2\pi}{\lambda z}\rho r_j\right) \quad (3.31)$$

and

$$\int_0^{\frac{2\pi}{\lambda z}\rho r_j} r\cdot J_{2m-1}(r)\mathrm{d}r = 2(2m-1)\frac{\pi}{\lambda z}\rho r_j\sum_{k=0}^{+\infty}\frac{m+k}{\left(m+k+\frac{1}{2}\right)\left(m+k-\frac{1}{2}\right)}J_{2m+2k}\left(\frac{2\pi}{\lambda z}\rho r_j\right) \quad (3.32)$$

where k is a nonnegative integer.

Substituting Eq. (3.31) into Eq. (3.28) we find,

$$\begin{aligned}\ker_{n=2m\ \&\ n\neq 0} = &\sum_{m=1}^{+\infty}\frac{(-1)^m\cdot\lambda z r_j}{\pi\rho}\sin(m\delta_j)\cos(m\delta_j-2m\varphi+2ma)\\ &\cdot\sum_{k=0}^{+\infty}\frac{2m+2k+1}{(m+k)(m+k+1)}J_{2m+2k+1}\left(\frac{2\pi}{\lambda z}\rho r_j\right)\end{aligned} \quad (3.33)$$

Similarly substituting Eq. (3.32) into Eq. (3.29) we have,

$$\ker_{n=2m-1\ \&\ n\neq 0} = \sum_{m=1}^{+\infty} \frac{2r_j \cdot (-1)^m \cdot \lambda z i}{\pi\rho} \sin\left[\frac{(2m-1)\delta_j}{2}\right] \cos\left[\frac{(2m-1)(\delta_j + 2a - 2\varphi)}{2}\right] \cdot \sum_{k=0}^{+\infty} \frac{m+k}{\left(m+k+\frac{1}{2}\right)\left(m+k-\frac{1}{2}\right)} J_{2m+2k}\left(\frac{2\pi}{\lambda z}\rho r_j\right) \tag{3.34}$$

Consequently, instead of the integral (3.18) we obtain the analytical solution of the kernel from Eqs. (3.23), (3.33) and (3.34),

$$\ker = \ker_{n=0} + \ker_{n=2m\ \&\ n\neq 0} + \ker_{n=2m-1\ \&\ n\neq 0} \tag{3.35}$$

And applying the linearity theorem, the Fourier transform of the whole '*pie*' (3.16) could be simply sum of the individual transforms,

$$\mathcal{F}\{pie\} = \frac{e^{ikz} e^{i\frac{k}{2z}\rho^2}}{i\lambda z} \cdot \ker \tag{3.36}$$

Finally the Fourier spectrum of a single circular sector can be explicitly expressed as,

$$\begin{aligned}\mathcal{F}\{pie\} = {} & \frac{e^{ikz} e^{i\frac{k}{2z}\rho^2}}{i\lambda z} \cdot \left\{ \frac{\delta_j \lambda z r_j}{2\pi\rho} J_1\left(\frac{2\pi}{\lambda z}\rho r_j\right) \right. \\ & + \sum_{m=1}^{+\infty} \frac{(-1)^m \cdot \lambda z r_j}{\pi\rho} \sin\left(m\delta_j\right) \cos\left(m\delta_j - 2m\varphi + 2ma\right) \\ & \cdot \sum_{k=0}^{+\infty} \frac{2m+2k+1}{\left(m+k\right)\left(m+k+1\right)} J_{2m+2k+1}\left(\frac{2\pi}{\lambda z}\rho r_j\right) \\ & + \sum_{m=1}^{+\infty} \frac{2r_j \cdot (-1)^m \cdot \lambda z i}{\pi\rho} \sin\left[\frac{(2m-1)\delta_j}{2}\right] \cos\left[\frac{(2m-1)\left(\delta_j + 2a - 2\varphi\right)}{2}\right] \\ & \left. \cdot \sum_{k=0}^{+\infty} \frac{m+k}{\left(m+k+\frac{1}{2}\right)\left(m+k-\frac{1}{2}\right)} J_{2m+2k}\left(\frac{2\pi}{\lambda z}\rho r_j\right) \right\}\end{aligned} \tag{3.37}$$

where J_{num} is a Bessel function of first kind, order num.

3.2.2 Fraunhofer diffraction spectrum of the 2D QD grating

To obtain the final spectrum of QD grating, we first consider the structure of grooves. In accord with the previous introduction of the QD grating principles (see section 2.1.1), the grating is plotted on rectangular (*x*-*y*) coordinates, in which the base point of the system corresponds to the centre of concentric annuli. Here only the grating profile along the *x* axis is taken into account.

The non-periodic varying radii r_j (Eq. (2.12)) can be re-written as,

$$r_j = \left[\frac{j\lambda R^2}{W_{20}} + \left(\frac{\lambda R^2}{2 d_0 W_{20}} \right)^2 \right]^{1/2} \tag{3.38}$$

Again, as preceding notations, λ is the wavelength of incident wave, R the radius of grating, d_0 the central period, W_{20} the defocus coefficient which is equivalent to the extra path length introduced at the edge of the aperture [7]. The integer j is equivalent to the numerical order of grating arcs in this calculation, where j=0 represents the grating centre (0, 0). Consequently j varies from negative to positive values (from left to right side of grating model as Fig. 3.2 shown).

In practical terms, we should also consider the extreme limits of j, which depends on the edges of aperture and can be described as,

$$j_{\text{limits}} = \pm \frac{R}{d_0} + \frac{W_{20}}{\lambda} \tag{3.39}$$

where the plus and minus sighs are included to allow for the maximum or minimum value of j, respectively.

Here we emphasize again that the minimum period of grating (Eq. (2.14)) should also be checked during the grating design, which is normally not less than 2 μm to meet the limitation(s) of grating fabrication [2].

Taking all the factors above into account, a set of parameters illustrated in Table 3.1 are applied to the analytical grating model for further calculations.

Table 3.1 Designed parameters of QD grating.

Parameter	*Value*
Central Period (d_0)	**50 μm**
Radius (R)	**10mm**
W_{20}	**50λ**
Wavelength (λ)	**532nm**

So the Eqs. (3.39) and (2.14) give the results that N, the total number of grating arcs, is 801 ($j_{\max}$-$j_{\min}$+1) and the minimum period is 40 μm. And, the wedge angles δ_j could be obtained by *cosine formula* in trigonometry as demonstrated in Fig. 3.2 and Fig. 3.4,

$$\delta_j = 2\arccos\left(\frac{r_0^{\,2} + r_j^{\,2} - R^2}{2r_0 r_j}\right) \tag{3.40}$$

where r_0 corresponds to the radius of the arc which is located at the centre of the QD grating.

Now we return to the spectrum calculation of the QD grating. Based on the discussions above, we can obtain the values of radii r_j and wedge angles δ_j, where j varies from $j_{\min}$ to $j_{\max}$ (Eq. (3.39)). Then these values are exported to a matrix for quantizing the Fourier spectra of circular sectors (expressed as Eq. (3.37)) later.

According to the linearity property of Fourier transform [4], the Fourier spectra of the 'concentric' sectors should be the linear superposition of Fourier spectrum of each sector. Especially in this case, the Fourier spectrum of an amplitude grating could be expressed as the sum of spectra of even/odd numbered slits (i.e. the even/odd numbered slits represent transparent/opaque regions, respectively). Let odd-numbered slits be transparent, and a positive integer N represents the total number of grating arcs. The Fourier spectrum of an arbitrary odd-numbered slit could be described as,

$$\mathcal{F}\{\text{transp-slit}\}_{N-2M-1} = \mathcal{F}\{pie\}_{N-2M} - \mathcal{F}\{pie\}_{N-2M-1} \tag{3.41}$$

where the integer $M = 0,1,\ldots,\text{Ceiling}[\frac{N}{2}-1]$. Note that $\text{Ceiling}[\frac{N}{2}-1]$ denotes the smallest integer greater than or equal to $\frac{N}{2}-1$.

Consequently the Fourier spectrum of the amplitude grating tends to the form,

$$\mathcal{F}\{\text{amplitude grating}\} = \sum_{M=0}^{\text{Ceiling}\left[\frac{N}{2}-1\right]} \mathcal{F}\{\text{transp-slit}\}_{N-2M-1} \tag{3.42}$$

Consider next a more complicated case. It is known that gratings could be categorised by the modification to incident light — the so called 'amplitude grating' consists of alternating transparent and opaque regions, whereas in a phase grating all regions are transparent so that the optical efficiency is higher. In order to explore the Fourier spectrum of the 2D QD phase grating, let us start off with the original integral (3.16). The only difference between the definitions of amplitude and phase gratings might be the additional phase shift ω, so that Eq. (3.16) may be expressed as,

$$\mathcal{F}\{pie^*\} = \frac{e^{jkz}e^{j\frac{k}{2z}\rho^2}}{j\lambda z}\cdot\int_0^{r_j}\int_a^{\delta_j+a} \mathrm{e}^{i\omega\cdot\text{bool}} e^{i\frac{2\pi}{\lambda z}\rho r\sin(\theta-\varphi-\frac{\pi}{2})} r\mathrm{d}r\mathrm{d}\theta \tag{3.43}$$

where the value of 'bool' alternates between 1 and 0 in accordance with whether a single grating slit is etched or not. Assuming that the phase shift ω is constant for a specific grating to ensure the intensity balance in first 3 diffraction orders, the phase factor $e^{i\omega\cdot\text{bool}}$ could accordingly be considered as a constant and taken out of the integral, by which Eq. (3.43) yields,

$$\begin{aligned}\mathcal{F}\{pie^*\} &= \mathrm{e}^{i\omega\cdot\text{bool}}\cdot\frac{e^{jkz}e^{j\frac{k}{2z}\rho^2}}{j\lambda z}\int_0^{r_j}\int_a^{\delta_j+a} e^{i\frac{2\pi}{\lambda z}\rho r\sin(\theta-\varphi-\frac{\pi}{2})} r\mathrm{d}r\mathrm{d}\theta \\ &= \mathrm{e}^{i\omega\cdot\text{bool}}\cdot\mathcal{F}\{pie\}\end{aligned} \tag{3.44}$$

We have briefly introduced that, as illustrated in section 2.2, the phase gratings we are currently using are single etched. Similar to the notations defined in Eq. (3.41), for the phase grating let odd-numbered slits be etched (bool=1) thus a constant phase delay ω has been produced. Therefore, for odd- and even- numbered slits, we have the Fourier spectra respectively,

$$\begin{aligned}\mathcal{F}\{\text{odd-slit}\}_{N-2M-1} &= \mathcal{F}\{pie^{*}\}_{N-2M} - \mathcal{F}\{pie^{*}\}_{N-2M-1} \\ &= \mathrm{e}^{i\omega}\cdot\left[\mathcal{F}\{pie\}_{N-2M} - \mathcal{F}\{pie\}_{N-2M-1}\right] \\ \mathcal{F}\{\text{even-slit}\}_{N-2M-2} &= \mathcal{F}\{pie^{*}\}_{N-2M-1} - \mathcal{F}\{pie^{*}\}_{N-2M-2} \\ &= \mathcal{F}\{pie\}_{N-2M-1} - \mathcal{F}\{pie\}_{N-2M-2}\end{aligned} \tag{3.45}$$

For the purpose of calculation, we set $\mathcal{F}\{pie\}_{0} = 0$.

Finally the Fourier spectrum of the phase grating can be described as,

$$\mathcal{F}\{\text{phase grating}\} = \sum_{M=0}^{\text{Ceiling}\left[\frac{N}{2}-1\right]} \mathcal{F}\{\text{odd-slit}\}_{N-2M-1} + \sum_{M=0}^{\text{Ceiling}\left[\frac{N}{2}-1\right]} \mathcal{F}\{\text{even-slit}\}_{N-2M-2} \tag{3.46}$$

Note that the effect of the marginal fractions generated by the subtraction of adjacent sectors (Eqs. (3.41) and (3.45)) may be neglected due to their nominal contribution to the calculation of Fourier integral and hence the image quality.

3.3 Numerical solution to the Fourier spectrum of 2D QD grating

We have obtained the analytical solution to the Fraunhofer diffraction spectrum of the 2D QD grating (Eqs. (3.37), (3.42) and (3.46)). However, due to the computational complexity of the high order Bessel functions and the tremendous series, it seems not practical to work out the numerical solution through the continuous analytic expression. Therefore an algorithmic method based on discrete arguments sampling is utilized, by which some points with identical intervals are selected from the spectra surface (Eq. (3.37)) for calculation, such that the spectrum/power curve can be fitted by the numerical function values at these points.

Of particular interest is the case when the energy is balanced in the first three diffraction orders, as section 2.2.1 represented. Although a ‘working’ phase of 2.00777rad (Fig. 2.5) had been obtained using the one-dimensional, period-fixed grating model under certain experimental conditions, an effective optimization based on the two-dimensional QD phase grating model should be of great assistance in the more precise grating design.

In this section we firstly show the design of the algorithm for calculating the Fourier spectrum of 2D QD grating, and the optimized working phase is therefore figured out using an iterative method; accordingly the Fraunhofer diffraction pattern at the 'working' point can finally be obtained.

3.3.1 Numerical computation of the Fourier spectrum of 2D QD grating

The theoretical model of 2D QD grating has been established in preceding sections, but the analytical results attract practically little attention. Hence we shall now extend this analysis to the numerical expressions, i.e. the final description of a specific diffraction pattern may therefore be the intensity distribution. To fully demonstrate the Matlab algorithm design, we will just focus on the 2D QD phase grating model and for simpler cases, such as QD amplitude grating, similar principle may be straightforwardly applied.

According to Eq. (3.46), it turns out that the Fourier spectrum of the QD phase grating is the sum of Fourier transform of all slits, so that we may start off with the calculation of Fourier transform of a single slit. To do so we now recall Eqs. (3.44) and (3.45) to compute the Fourier spectrum of a single 'pie'. Considering two neighbouring pies OBA and OCD, we set up an X-Y Cartesian coordinate system as shown in Fig. 3.5, in which the X axis is the horizontal symmetry axis of the QD grating and the coordinate origin O is the centre of the adjacent arcs $\widehat{BA}$ and $\widehat{CD}$. Following the preceding notation, let $\widehat{BA}$ and $\widehat{CD}$ be the j-th and (j+1)-th arcs, respectively, hence the Fourier transform of the j-th slit $\widehat{ABCD}$ can be given by,

$$\mathcal{F}\left\{\text{slit}_j\right\} = G(p,q) = \mathrm{e}^{i\omega\cdot\text{bool}} \cdot \oiint_S e^{-\frac{2\pi i}{\lambda}(p\xi+q\eta)}\,\mathrm{d}\xi\mathrm{d}\eta \tag{3.47}$$

where ω is the phase shift, and 'bool' alternates between 1 and 0 with respect to j is odd- and even- number respectively. In comparison with Eqs. (3.13) and (3.44), the integral extends over the closed boundary S which is surrounded by the arcs $\widehat{AB}$, $\widehat{BC}$, $\widehat{CD}$ and $\widehat{DA}$.

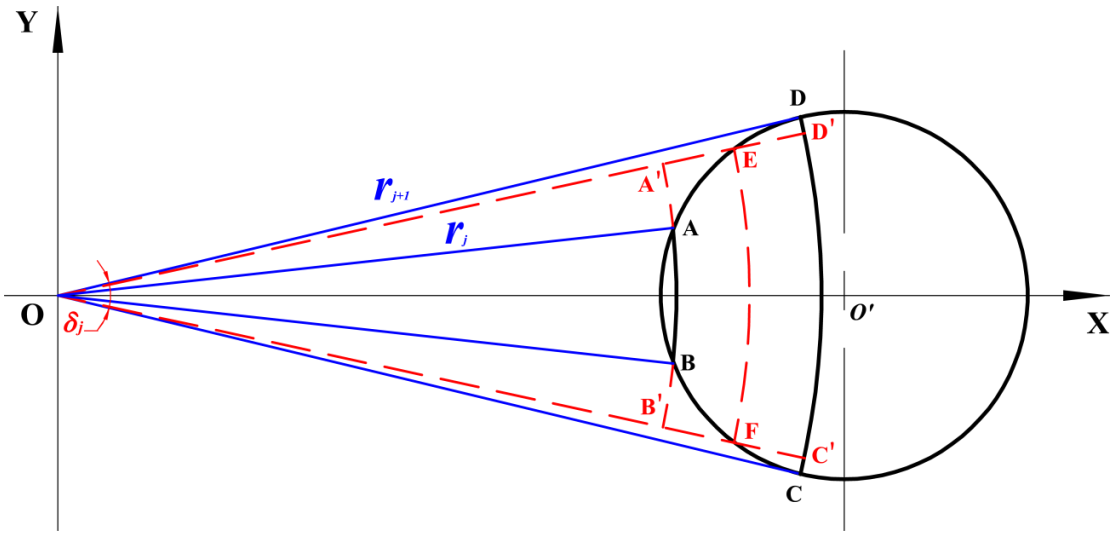

Fig. 3.5 Illustration of a single slit in 2D QD phase grating.

If a virtual arc $\widehat{EF}$, whose radius is the mid-value of that of arcs $\widehat{AB}$ and $\widehat{CD}$, is defined, hence A' denotes the intersection of OE and the extension of arc $\widehat{BA}$, B' the intersection of OF and the extension of arc $\widehat{AB}$, C' the intersection of arc $\widehat{CD}$ and the extension of OF, and D' the intersection of arc $\widehat{CD}$ and the extension of OE, as described in Fig. 3.5. In view of the fact that the width of a single slit is far smaller than the radius of concentric arcs, the Fourier transform of the slit may be approximated by the integral in an alternative domain S',

$$G(p,q) \approx G'(p,q) = \mathrm{e}^{i\omega\cdot\mathrm{bool}} \cdot \iint_{S'} e^{-\frac{2\pi i}{\lambda}(p\xi+q\eta)} \mathrm{d}\xi \mathrm{d}\eta \tag{3.48}$$

where S' is surrounded by the arcs $\widehat{A'B'}$, $\widehat{B'C'}$, $\widehat{C'D'}$ and $\widehat{D'A'}$.

To solve the integral above, we again transform current Cartesian system to polar coordinates, in which (r, θ) and (ρ, φ) imply a typical point in the aperture and diffraction pattern respectively (see Eq. (3.15) for details). For convenience the Fourier transform of a single pie can be characterized in terms of determinate parameters,

$$\mathcal{F}\{pie\}_j = \mathrm{pie}(\rho,\varphi;r_j,\delta_j,a_j,\lambda,z) \tag{3.49}$$

where r_j, δ_j and a_j have been defined in Fig. 3.4 (note that a_j was regarded as a constant in preceding calculation thus the abbreviation *'a'* was applied), λ the

wavelength, and *z* the image distance. Based on Fig. 3.4 and Fig. 3.5, we may rewrite Eq. (3.40),

$$\delta_j = 2\arccos\left(\frac{r_0^{\,2} + r_m^{\,2} - R^2}{2r_0 r_m}\right) \tag{3.50}$$

where r_0 is the radius of the arc which is located at the centre of the QD grating, $r_m = \frac{r_j + r_{j+1}}{2}$ the radius of the mid-arc and *R* the radius of QD grating.

And a_j, the start point of the *j*-th sector, can be expressed as,

$$a_j = -\frac{\delta_j}{2} \tag{3.51}$$

Under the certain conditions of Fraunhofer diffraction (Eq. (3.10)), a value of $z = \frac{10}{\lambda}$ is chosen for numerical test of Fourier spectrum calculation. Based on the numerical tests using Matlab, we may conclude that the smearing spots are axial symmetry (around φ=0 axis) and thus some basic information, i.e. size and position of the spots, could be roughly obtained. The initial results show that the pattern consists of a bright and sharp spot centred at the origin and a pair of conjugate smearing spots symmetrically located at both sides of the centre one (in principle there should be a series of smearing spots but we only focus on the ones correspond to ±1st orders). In this case, the radius of the sharp spot in the centre is about 0.4mm, whereas that of the smearing spots is about 6mm, with their centres at (ρ=20mm, φ=π) and (ρ=20mm, φ=0), respectively.

Now let us turn our attention to the calculation of the detailed Fourier spectrum of 2D QD grating. We have realized the huge complexity of solving the analytical solution (Eq. (3.37)) and thus would apply a discrete algorithm, which is based on the uniform sampling in the estimated distribution area of spots, to produce approximate numerical solution. So far we have assumed that the image distance *z* is $10/\lambda$, and we may sample ρ from 0 to 0.5 with the step of 0.001 and φ from 0 to 2π with the step of $\pi/90$.

This method of computing Fourier spectrum by means of discrete uniform sampling, which is of practical importance in attaining numerical solution, can be applied to search the optimized working phase and thus develop further design of QD grating with better performance.

3.3.2 Finding the optimized working phase by bisection method

Before discussing the working phase of the QD phase grating, we would like to say a few words about the *bisection method*, which is a root-finding algorithm for a given function *g*. It typically works when *g* is a continuous function and requires previous knowledge of two initial guesses, a_1 and a_2, such that $g(a_1)$ and $g(a_2)$ have opposite signs. And according to the *intermediate value theorem*, the continuous function *g* must have at least one root in the interval (a_1, a_2) [8].

In our case, since the Fraunhofer spectrum of the 2D QD phase grating (see Eqs. (3.37) and (3.46) for details) can be regarded as a continuous function of the phase ω, the bisection method is implemented to find the optimized 'working' phase of the QD grating, with which a balanced intensity distribution of Fraunhofer pattern in the first three diffraction orders could be achieved. Ideally, on the assumption that all the energy flux was focused only on the first three orders, the total intensity of the Fraunhofer pattern of the QD phase grating, which is denoted by $E_\omega\{\text{phase grating}\}$, could be approximated by the sum of the intensities in the zero and first orders. Then the energy in the zero order may be expressed as,

$$\begin{aligned} E_\omega^{(0)} &= \iint_{\Omega_0} \left|\mathcal{F}_\omega\{\text{phase grating}\}\right|^2 \mathrm{d}\rho\mathrm{d}\varphi \\ &= \frac{1}{3} E_\omega\{\text{phase grating}\} \end{aligned} \tag{3.52}$$

where Ω_0 represents the integral domain of the spectrum in zero order and $\mathcal{F}_\omega\{\text{phase grating}\}$ is the Fraunhofer spectrum of the QD phase grating (Eq. (3.46)).

To determine the working phase ω, we define a continuous function,

$$G(\omega) = \iint_{\Omega_0} \left|\mathcal{F}_\omega\{\text{phase grating}\}\right|^2 \mathrm{d}\rho\mathrm{d}\varphi - \frac{1}{3} E_\omega\{\text{phase grating}\} \tag{3.53}$$

on an interval [ω_1, ω_2] such that $G(\omega_1)G(\omega_2)<0$. Hence at least one algebraic root of function $G(\omega)$ should be bracketed within a subinterval of [ω_1, ω_2] according to the bisection algorithm. The iteration process can be described as the following flowchart,

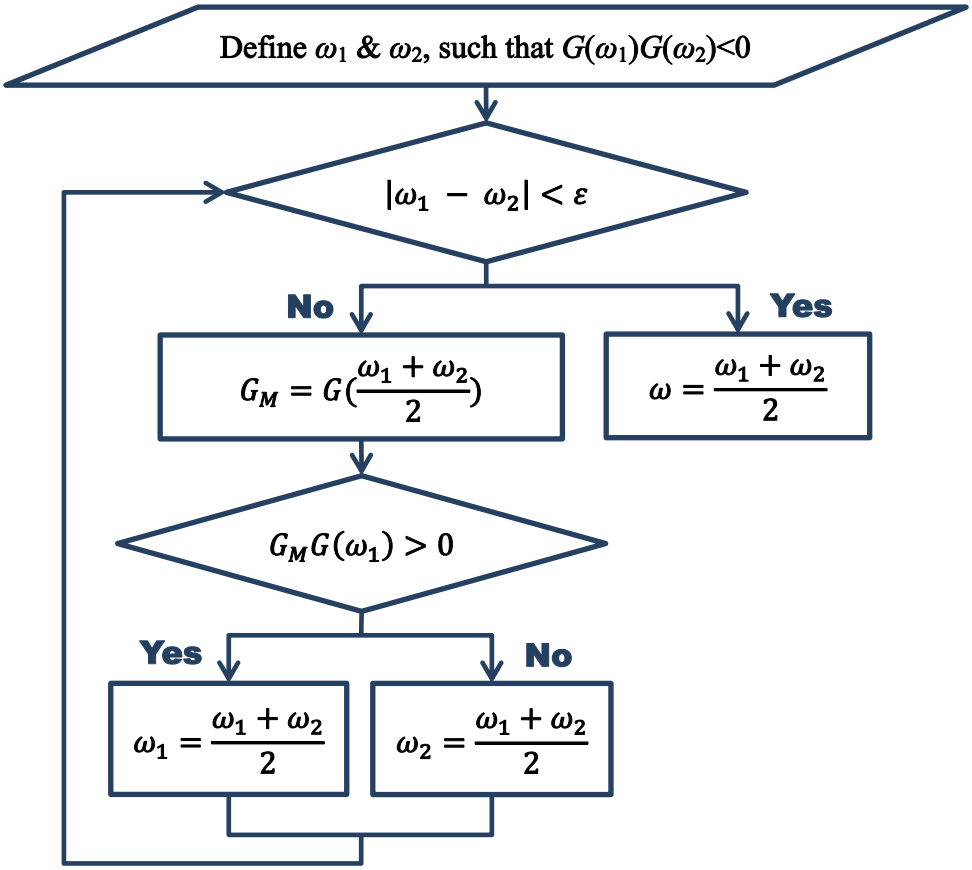

Fig. 3.6 Bisection method for searching the optimized working phase ω.

where $|\omega_1 - \omega_2| < \varepsilon$ implies an interval approaching that of an infinitesimal-sized interval.

It is very unlikely but possible that the initial interval $|\omega_1 - \omega_2|$ is sufficiently small, such that the root of the function $G(\omega)$, i.e. the working phase, can be calculated as the arithmetic mean value of ω_1 and ω_2. Otherwise, in each iteration the method bisects the interval and computes G_M, which is the function value at the midpoint $\frac{\omega_1 + \omega_2}{2}$. Then the method examines the sign of $G_M G(\omega_1)$, by doing so a new subinterval can be produced which is guaranteed to bracket a root. The result of one iteration is used as the

starting point for the next iteration. And as this continues, the interval between ω_1 and ω_2 will become increasingly smaller, converging on the root of the function. We note that the method may never find a function value being exactly zero due to the finite precision of sampling, though the precision in our case can reach up to 10^{-6}.

Based on the numerical Fourier spectrum attained by discrete uniform sampling algorithm demonstrated in subsection 3.3.1, bisection method is applied to find the optimized working phase of QD grating. As we have mentioned in preceding sections, a phase of 2.00777rad, which is calculated from a 1-D and period-fixed grating model, is currently used for design of QD grating (i.e. Fig. 2.5). Therefore, an initial interval of [1.9, 2.1], which is around 2.00777rad, is chosen for further optimization. For a certain QD grating (see Table 3.1 for parameters), an optimized phase of 1.99999rad is obtained after 18 iterations and the energy distribution of first 3 orders @2.00777rad is also calculated for comparison, as Table 3.2 shown.

Table 3.2 Bisection method for searching optimized phase of QD grating.

No. of Iteration	*Searching Phase*	*Normalized Intensity*		*Energy difference between 0^{th} & $\pm1^{st}$ orders*
		0^{th} order	*$\pm1^{st}$ order*	
2	1.95	0.357920578	0.321039711	0.036880868
6	1.996875	0.334857221	0.332571390	0.002285831
10	1.999804688	0.333424825	0.333287588	0.000137237
14	1.999987793	0.333335338	0.333332331	3.01E-06
18	**1.999994659**	**0.333331982**	**0.333334009**	**2.03E-06**
	2.00777	**0.329536266**	**0.335231867**	**-0.005695601**

From Table 3.2 we may see that, for a QD grating with moderate parameters (Table 3.1), the optimized phase is very close to 2.00777rad — which might also be the reason that the phase of 2.00777rad works well under some non-rigorous conditions. However, according to our modelling experience, the working phase may depend strongly on the curvature parameter(s) of QD grating, i.e. W_{20}. Consequently, the optimized phase of a considerable curved QD grating may be quite different with the value calculated by 1D

model. For future design of high-quality QD grating, obtaining a precise working point should be essential.

3.3.3 Numerical solution to the diffraction pattern

The discussion above refers to a complete algorithm for numerical computation of Fourier spectrum, as well as searching a working phase for optimized design of the 2D QD grating. However, of ultimate interest is the intensity rather than complex field strength. Therefore the normalized intensity of Fraunhofer diffraction pattern will be illustrated in this subsection.

Firstly let us consider the QD amplitude grating. According to Eq. (3.42) and the grating parameters introduced in Table 3.1, the Fourier spectrum of the 2D QD amplitude grating can be obtained using similar algorithm demonstrated in subsections above. Its 2D Fraunhofer diffraction pattern is illustrated in Fig. 3.7 (see the blue solid line).

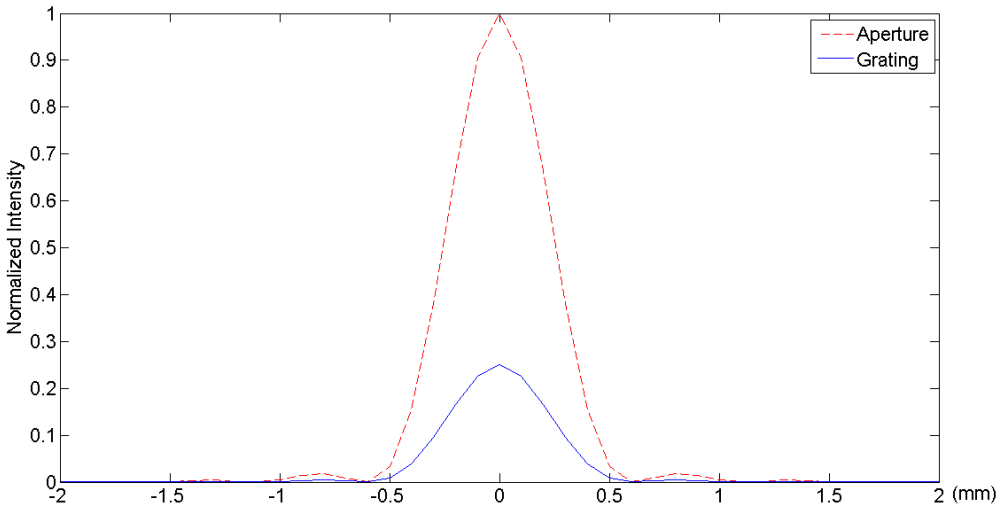

Fig. 3.7 Normalized intensity distributions of same profiled 2D QD amplitude grating and circular aperture.

In addition, as Fig. 3.7 shown, the Fraunhofer diffraction pattern of a circular aperture which has the same profile with that of 2D QD amplitude grating is also introduced. In comparison with their intensity distributions, we can find that the half widths of the two central peaks are identical, which indicates the feasibility of our 2D QD grating model in some extent. Further verifications will be demonstrated in section 3.4.

Similar considerations now apply to the 2D QD phase grating (see Eqs. (3.37) and (3.46) for the analytical Fraunhofer spectrum). Implementing the bisection method illustrated in subsection 3.3.2, the optimized working phase of the QD phase grating is found to be 1.99999rad based on the parameters shown in Table 3.1, hence the etch depth could be 368nm @532nm wavelength when the fused silica is applied as grating substrate. In Fig. 3.8, the normalized intensity distribution of optimal QD phase grating is displayed in the form of contour plot due to the big difference of intensity maxima among the spots, in which that of another 2D QD phase grating of the same design but with the phase of 2.00777rad (whence by Fig. 2.5) is also shown for comparison.

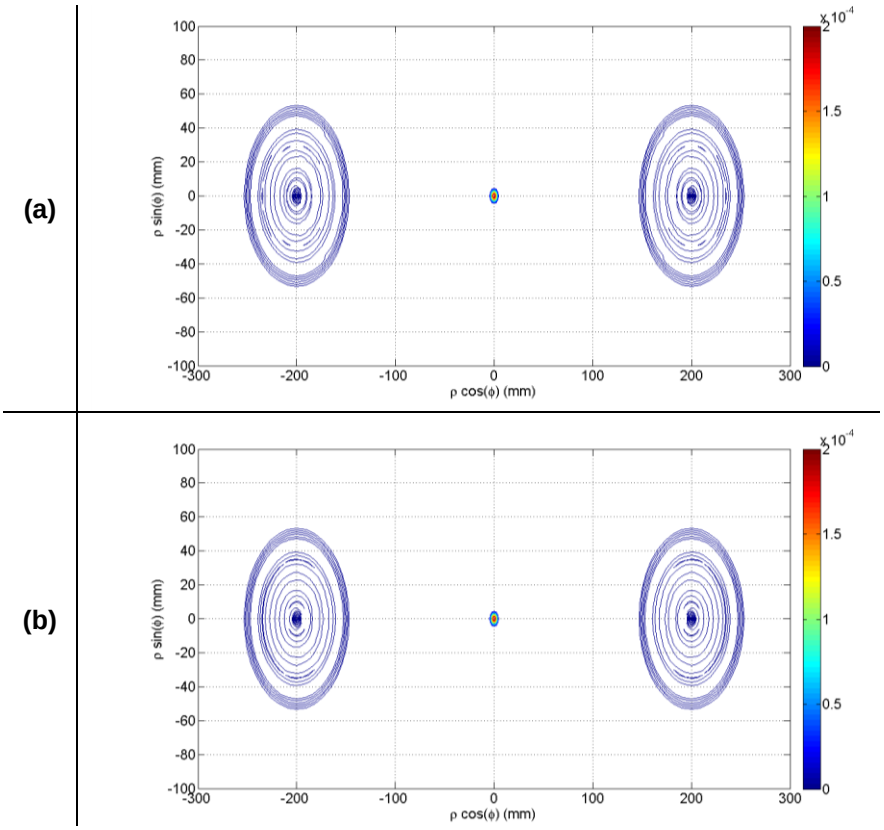

Fig. 3.8 Contour plot of normalized intensity for Fraunhofer diffraction pattern of 2D QD phase gratings with working phases of: (a) 1.99999rad; (b) 2.00777rad.

Although there is little difference between the two sets of contour lines displayed in Fig. 3.8, we have first demonstrated the Fraunhofer diffraction pattern of QD grating using a 2D analytical model, which approaches more elaborate grating design and may have important practical uses in the future. To explore the detailed energy distribution of each order, we plot the 3D diffraction pattern of zeroth and first orders separately for better observation (working phase of 1.99999rad only), as Fig. 3.9 shown.

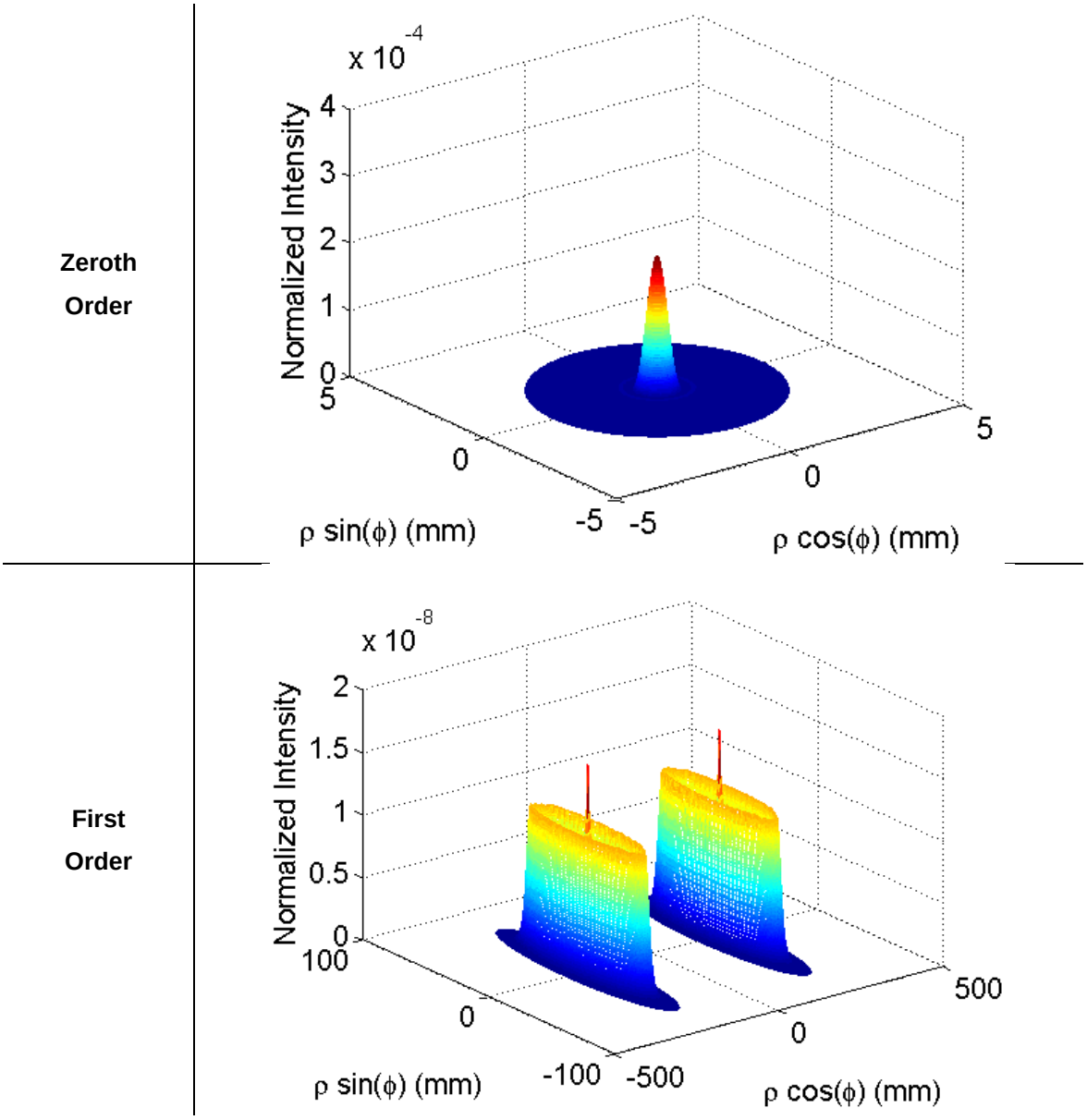

Fig. 3.9 3D diffraction pattern of 2D QD phase grating.

3.4 Verifications of the 2D QD grating theory and algorithm

To assess the validities and feasibilities of both my calculation and the numerical computation algorithm introduced in section 3.2 and 3.3, some verification tests, in which a few specially designed grating models are generated and the normalized intensity distribution of first three diffraction orders is illustrated, are applied in this section. As demonstrated before, the gratings are illuminated by a normally incident, unit-amplitude and monochromatic plane wave. Since only 2D phase gratings are applied in this section, we just simply label them 'grating' rather than constantly emphasizing the 'phase'.

3.4.1 Verification of the algorithm by straight-line and period-fixed grating

We have so far considered the 2D QD grating only, but our algorithm may easily be extended to other grating models. In order to check whether the algorithm and Matlab codes work well, 799 rectangular functions with equal height h and different widths w_j ($j = -349, -348 \ldots 448, 449$) in the form of arithmetic progression (say the common difference, w_j- w_{j-1}, is 25μm) are generated. Hence a series of equally-spaced straight slits are created by subtraction of adjacent rectangles and a phase grating could be obtained by assigning the working phase of 2.00777rad to the etched slit. Instead of normal method that generates a comb function and Fourier transforms it for spectrum, we now start off with the Fraunhofer diffraction spectra of these rectangular functions and then work out the energy distribution of the grating with similar principles described by Eqs. (3.41) and (3.42); the result is accordingly in comparison with general conclusion which could be found in any introductory optics text.

Under the condition of Fraunhofer approximation, it is well known that the diffraction spectrum of rectangular function can be approximated as Fourier transform of it, which is expressed as *sinc function* in rectangular (x-y) coordinates [4],

$$\mathcal{F}\left\{\text{rect}_{w_j,h}\right\} = \frac{e^{ikz} e^{i\frac{k}{2z}(x^2+y^2)}}{i\lambda z} w_j h \cdot \text{sinc}(\frac{w_j x}{\lambda z}) \cdot \text{sinc}(\frac{hy}{\lambda z}) \tag{3.54}$$

where λ is the incident wavelength of 532nm and $z = 10/\lambda$ the normal distance between aperture and diffraction image plane in this case.

Following Eq. (3.45), the Fourier transform of the odd- and even- numbered rectangular slits could be written as,

$$\begin{aligned} \mathcal{F}\left\{\text{odd-rectslit}\right\}_{799-2i-1} &= \text{e}^{i\omega} \cdot \left[\mathcal{F}\left\{rect\right\}_{799-2i,h} - \mathcal{F}\left\{rect\right\}_{799-2i-1,h} \right] \\ \mathcal{F}\left\{\text{even-rectslit}\right\}_{799-2i-2} &= \mathcal{F}\left\{rect\right\}_{799-2i-1,h} - \mathcal{F}\left\{rect\right\}_{799-2i-2,h} \end{aligned} \tag{3.55}$$

Similarly according to Eq. (3.46), the Fourier transform of this straight-line, period-fixed phase grating is,

$$\mathcal{F}\left\{\text{phase rectgrating}\right\} = \sum_{i=0}^{\text{Ceiling}\left[\frac{799}{2}-1\right]} \mathcal{F}\left\{\text{odd-rectslit}\right\}_{799-2i-1} + \sum_{i=0}^{\text{Ceiling}\left[\frac{799}{2}-1\right]} \mathcal{F}\left\{\text{even-rectslit}\right\}_{799-2i-2} \tag{3.56}$$

where $\text{Ceiling}\left[\frac{799}{2}-1\right]=399$ denotes the smallest integer greater than or equal to $\frac{799}{2}-1$.

The diffraction pattern is given by the coefficient square of Fourier spectrum Eq. (3.56) [4], as Fig. 3.10 shown.

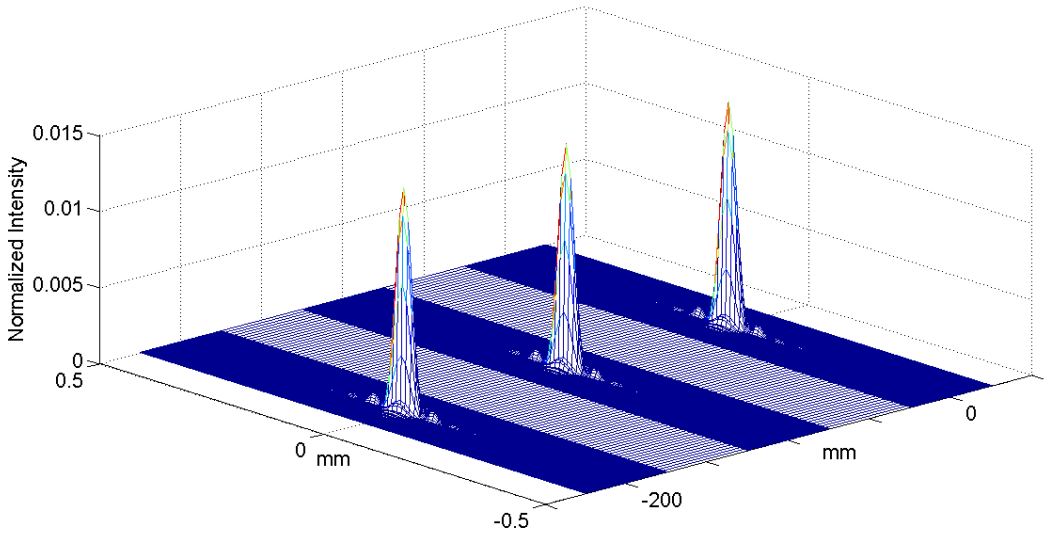

Fig. 3.10 Normalized intensity of Fraunhofer diffraction pattern of 2D straight-line grating at working phase of 2.00777rad.

Compared with the Fraunhofer diffraction pattern at rectangular aperture in *'Born and Wolf'* [1], we find that the energy distribution of the three orders in Fig. 3.10 matches very well with the theoretical value, which indicates that, at least, our algorithm is logically reasonable and in practice the Matlab codes have successfully modelled the 2D grating. For verifying both the theory and numerical computation of our 2D QD grating model, we will characterize a specific grating in next subsection.

3.4.2 Verification of the 2D QD grating model by quasi-straight-line QD grating

By now we have done a few simulation tests in preceding sections, for the quantitative verification of our calculation in section 3.2 as well as the comparison with pervious results. Here we set the value of W_{20} to 0.5λ to produce a quasi-straight-line QD grating (see Table 3.3 for basic parameters).

Table 3.3 Designed parameters of QD grating with very small curvature.

Parameter	*Value*
Central Period (d_0)	**50 μm**
Radius (R)	**10mm**
W_{20}	**0.5λ**
Wavelength (λ)	**532nm**
Number of slits (N)	**800**

Since the curvature of this QD grating is 'quasi-straight-line', its working phase is 2.00831rad, which is quite close to 2.00777rad the rough phase attained from a 1D and period-fixed QD grating model. The 3D and contour plots of Fraunhofer diffraction pattern are shown in Fig. 3.11 and Fig. 3.12, respectively.

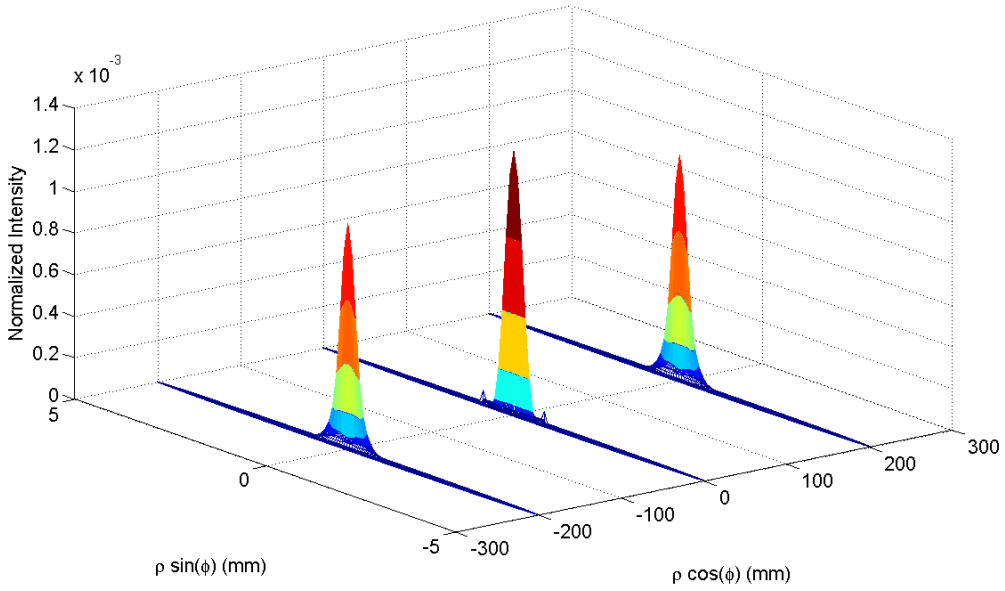

Fig. 3.11 3D Fraunhofer diffraction pattern of the quasi-straight-line 2D QD grating.

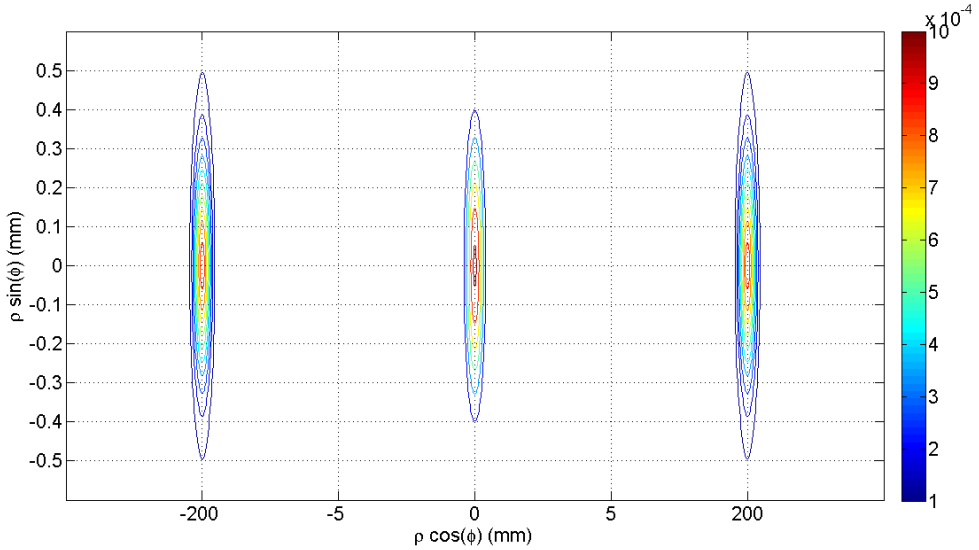

Fig. 3.12 Contour plot of normalized intensity for Fraunhofer diffraction pattern of the quasi-straight-line2D QD grating.

From Fig. 3.11 and Fig. 3.12 we see that the integrated intensity of first three orders is balanced with the working phase of 2.00831rad, which verifies both the 2D grating model as well as the numerical algorithm. Moreover, due to the central period of this quasi-straight-line 2D QD grating is equal to the period of the straight-line and period-fixed grating we discussed in last subsection, and the amounts of slits in both cases are identical, Fig. 3.10 may be recalled for comparison of the Fraunhofer patterns. Although these two cases seem apparently different, let us just qualitatively characterize the common points of them — the peaks of both diffraction patterns locate at the same position which are exactly the theoretical ones.

Based on the results of verifications, we may get a conclusion at this stage that the numerical computation algorithm works well thus our analytical model of 2D QD grating has been successfully established.

3.5 Summary

Although the physical principles underlying the quadratic curves of off-axis Fresnel zone plate have been substantially formulated by Blanchard and Greenaway [2, 3, 9-11], it is, in some cases, not straightforward for practical use. We have seen from section 2.2 that the 'working' phase (thus the etch depth) of present QD grating, which is a prime determinant for energy distribution of the first three diffraction orders, is obtained from a very rough 1D period-fixed (i.e. equally spaced) grating model.

A description of Fraunhofer diffraction at the 2D QD grating in terms of an elaborate analytical model is first systematically established. Based on scalar diffraction theories and discrete uniform sampling method, the detailed energy distribution of QD grating has been demonstrated in a simple and graphic manner. In our case, an optimal design of QD grating with high efficiency is the chief quantity of interest. Our 2D theoretical model ensures in mathematics that all the energy flow of incident light can be diffracted into first three diffraction orders, and an optimized working phase obtained by bisection method allows the integrated light intensity of each order to be balanced. A few simulation tests were also performed to verify the validities of our theory and algorithm.

Our mathematical model of 2D QD grating is designed not only for current use of obtaining an accurate working phase as fabrication guide, but also for versatile design and further explorations of both QD grating and 4D imaging system in the future. The work in this chapter is in collaboration with Dr. Yuewei Liu of School of Mathematics and Statistics, Lanzhou University.

3.6 References

[1] M. Born and E. Wolf, *Principles of optics*. Cambridge University Press, Cambridge, Corrected reprint of the 7th edition, (2001).

[2] P. M. Blanchard and A. H. Greenaway, *Simultaneous multiplane imaging with a distorted diffraction grating*. Applied Optics **38**(32), 6692-6699 (1999).

[3] A. H. Greenaway and P. M. Blanchard, *Three-dimensional imaging system*. in United States Patent No. 6,975,457 B1. Application No. 09/622,405, (QinetiQ Limited, London, 2005).

[4] J. W. Goodman, *Introduction to Fourier optics*. Roberts and Company Publishers, 3rd edition, (2005).

[5] Wikipedia, *Jacobi-anger_expansion*, http://en.wikipedia.org/wiki/Jacobi-anger_expansion, Access date: 9 March, 2015.

[6] NIST, *Online library of the National Institute of Standards and Technology (NIST)*, http://dlmf.nist.gov/10.22, Access date: 15 Feb, 2015.

[7] H. Hopkins, *The frequency response of a defocused optical system*. Proceedings of the Royal Society of London. Series A. Mathematical and Physical Sciences **231**(1184), 91-103 (1955).

[8] Wikipedia, *Root-finding algorithm*, http://en.wikipedia.org/wiki/Root-finding_algorithm, Access date: 16 March, 2015.

[9] P. M. Blanchard and A. H. Greenaway, *Multiplane imaging and wavefront sensing using distorted diffraction gratings*. Paper presented at Trends in Optics and Photonics. Diffractive Optics and Micro-Optics. Vol.41. Technical Digest. Postconference Edition, Quebec City, Canada:Opt. Soc. America. p. 250-252, 18-22 June (2000).

[10] P. M. Blanchard, D. J. Fisher, S. C. Woods and A. H. Greenaway, *Phase-diversity wave-front sensing with a distorted diffraction grating*. Applied Optics **39**(35), 6649-6655 (2000).

[11] P. M. Blanchard and A. H. Greenaway, *Broadband simultaneous multiplane imaging*. Optics Communications **183**(1), 29-36 (2000).

Chapter 4

Chromatic correction of QD grating based 4D MCMI system

Preface

From error budget demonstrated in Chapter 2, the chromatic smearing is regarded as the most severe aberration generated by QD grating. And for biological applications, there is always a very limited amount of light available for imaging and the object to be measured constantly changes, so that it is essential to explore a method of performing 4D imaging without the need of bandpass filter and complicated adjustment of optical system (i.e. the folded optical path [1]). To efficiently correct the chromatic smearing, we developed a combination system of QD grating and grism before [2-4]. A pair of grisms, whose separation can be varied, provide a collimated beam with a tuneable chromatic shear from a collimated polychromatic input. However, due to the mismatched optical parameters of grating-grism system, our previous imaging setup was not compatible with microscope and thus could be rarely utilized in actual stage of bioimaging applications. In this chapter the optimization of grism parameters and the customization of grism and its mount have been comprehensively considered, such that the optical system can be effectively improved and hence available for 4D multi-colour microscopy imaging (MCMI).

4.1 Background — chromatic properties of QD grating and grism

In preceding chapters we have investigated the principles of QD grating design, including the basic principles, the design of grating curvature (thus the mask plotting), the assessment of optical efficiency with respect to the grating profile, error budget, and of more practical importance, the 2D theoretical model for the guide of grating fabrication. However, due to the fact that the diffraction angle is wavelength dependent and the centre separation of the diffraction orders is dependent on the diffraction angle [5], for each wavelength that is input into the grating an image will be produced with a centre position determined by the wavelength, such that the images of nonzero diffraction orders may be chromatically smeared laterally if the dispersion is not

corrected as subsection 2.3.2.2 illustrated. Hence the QD grating based technique has to be narrow band to limit chromatic distortion in practice [6, 7], limiting the incident spectral bandwidth, restricting photon flux and hindering application to multiple-fluorophore life science imaging.

From the theoretical point of view (see Eqs. (2.44) and (2.45) for details), utilizing the inherent non-periodic chirps of QD grating, identical diffraction angles with respect to different wavelengths could be obtained, thus correcting the chromatic distortion. As demonstrated in Fig. 4.1, based on the chirped-period of QD grating, a well-designed optical system can produce collimated, chromatically displaced output, by which each colour 'sees' appropriate period of grating and therefore chromatic smearing can be corrected.

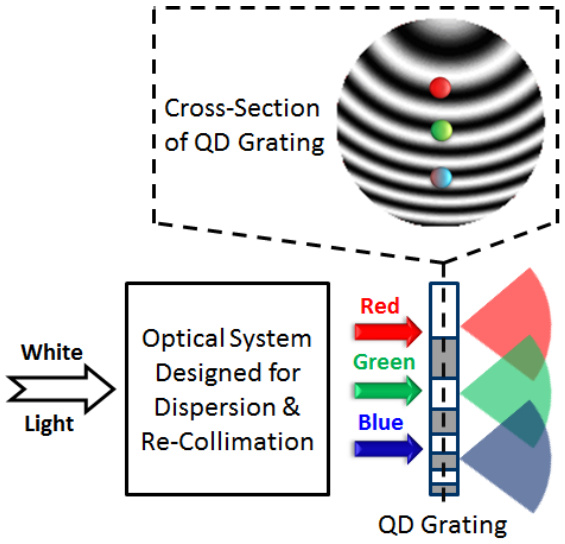

Fig. 4.1 Pre-dispersion and collimation of the incident light before the QD grating can correct the chromatic smearing.

Therefore one of the considerations for controlling the chromatically-induced lateral smearing is creating a collimated beam in which the spectral components are laterally displaced. Apart from the method we briefly introduced in subsection 2.3.2.2, which used a pair of blazed gratings and a folded optical path [1], we did demonstrate another correction scheme using a pair of grisms (a grating combined with a prism) [2-4]. Grisms of the sort discussed here were introduced by Traub [8] as a simple way to realize a (nearly) constant-dispersion spectrometer using a single grism to balance the oppositesense non-linearities of prism and grating dispersion. In order to describe the behaviour of the grism schematically, let the intensities I(x) be a function of focal-plane

spatial coordinate *x*, and the blue (B), green (G), and red (R) rays be defined so as to give equispaced wave numbers. As sketched in Fig. 4.2 [8], a prism and a grating produce crowding of the red and blue fringes respectively, whereas a grism disperses the spectrum at equal spatial intervals. Here the labels R, G and B identify intensity maxima in the red, green and blue regions of the channeled spectrum, respectively.

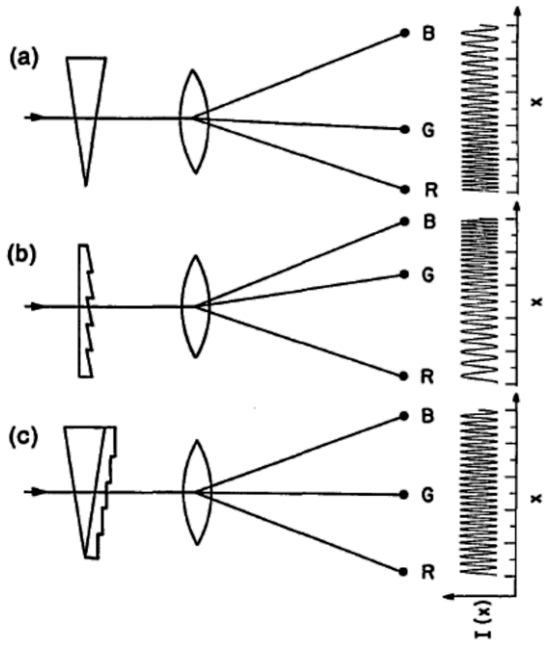

Fig. 4.2 Schematic diagram showing the appearance of spatially dispersed channeled spectrum from a: (a) prism, (b) grating, and (c) grism [8].

Grisms have subsequently been widely used in astronomy and in femtosecond laser systems for pulse stretching/compression [9-15]. Both reflective and transmissive grisms have been used, but not the use of a transmissive grism in which a selected wavelength can be undeviated – a possibility in the original suggestions by Traub and illustrated in the *Diffraction Gratings Handbook* [16]. It is this configuration, in which first-order diffraction of a selected wavelength occurs for an undeviated beam, that is exploited here to provide a simplified chromatic control system.

Ideally our grism should consist of a prism and a blazed transmission grating made from the same material (thus same refractive index) with the grating blaze angle equal to the wedge angle of the prism. But for primary tests, we just selected them from easily-available commercial off the shelf (COTS) components — a 18°8' wedge-angle prism fabricated from N-BK7 and a B270 transmission grating of 300 grooves/mm and a blaze angle of 17°30' (from Edmund Optics), giving a ‘straight-through’ wavelength

of 538.5nm. The grating is then cemented to one side of the prism and ideally the exterior faces of the grating facets should be parallel to the input face of the prism, whereas the cementing process seems not accurate enough such that the two grisms perform observable different jobs. These two grisms were mounted back to back in custom mounts within an assembly using opto-mechanical components (Thorlabs). To alleviate the unknown side-effect induced by the cementing error, we examined both grisms separately, then fixed the 'worse' performed grism yet moved the 'better' one for optical experiments illustrated in references [2-4]. Our custom mounts allow the input faces of the grisms to be rotated in the horizontal with respect to the optical axis with accuracy of ~2 degrees. The blazed surfaces of the grisms are quite fragile and represent a significant disadvantage of this design. The opto-mechanics allows for the grism separation to be varied, to within an accuracy of approximately ±1mm, over a range from 3 to 154mm, the lower figure selected to protect the fragile gratings whereas the higher one limited by the length of optical path as well as the size of grism mounts. Under these unstable conditions, though, the former results still appear to be promising that the grism pair successfully re-collimate the input beam with easily-varied chromatic shear by very careful adjustments, and thus verify the feasibility of the chromatic correction for our QD grating based broadband microscopy imaging system.

However, due to the lack of theoretical design, some optical parameters of our previous grating-grism system were mismatched. Accordingly the old imaging setup could only record one image of a single diffraction order, which was just applicable for chromatic correction tests rather than real microscopy imaging [2-4]. Moreover, the imaging system was incompatible with microscope because of various errors, i.e. inaccurate alignment of the long optical path (longer than 1 metre, see [4]) and the defects in the fabrication of grisms and their mounts. In this chapter a Mathematica ray-path model of grism is established and thus the parameters of grism could be theoretically optimized. With the well-customized grisms and their mounts, our 4D MCMI system can be successfully combined with microscope and considerable correction of chromatic smearing in both images of $\pm 1^{st}$ diffraction order could be simultaneously achieved.

4.2 Design and customization of grism and its mount

It has been seen in the previous sections, e.g. Fig. 2.12, that the images of the first order formed by the QD grating and 4*f* relay system are dispersed. A technique of dispersion

compensation using a pair of grisms could produce a wavelength dependent beam offset at the QD grating, however the initial design of grating-grism system reveals some significant disadvantages as introduced in section 4.1. The main question now arises how we optimize both the optical elements and the relay system to ensure our optical package of grating-grism combination be suited for attachment to a commercial microscope. Based on the practical experience, well designed/fabricated grisms and their mounts are of particular importance in building the 4D MCMI system.

4.2.1 Grism design and customization

Given that we have briefly obtained the chromatic properties of grism in section 4.1, in discussing the grism design and customization we shall take as our starting point the ray-path model, as Fig. 4.3 shown.

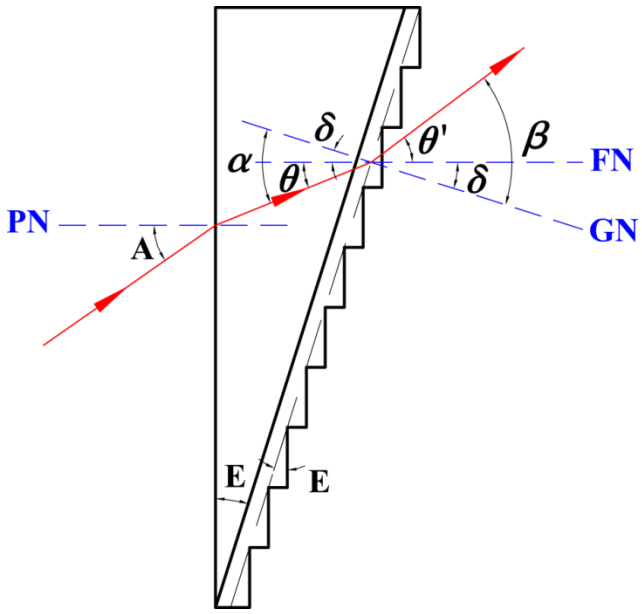

Fig. 4.3 Grism schematic showing ray paths from air to grism, and back to air.

In this case we still consider the cemented grism consisting of a wedge prism and a blazed grating rather than manufacturing a grating structure onto the hypotenuse face of a right-angle prism, in which the wedge angle of prism and the blazed angle of grating are identical and equal to *E*. The sign convention is that, measuring from the normal to the incident surface, counterclockwise angles are positive. Fig. 4.3 schematically describes that a ray indicated by the red arrow lines successively enters the prism at angle *A*, refracts, reaches to the grating at angle α, and finally diffracts into air at angle β (+1 order here), where the dashed blue lines represent the directions of the prism

normal (PN), grating normal of outer face (GN) and facet normal (FN). Here we assume that the interface of resin between prism and grating is sufficiently thin, and the refractive indices of the grism substrate and resin are nearly the same at our working wavelength. We also note that δ is the angle between GN and FN (thus equals to *E*) and the ray angles with respect to the facet are θ and θ', thus it is straightforward that,

$$\begin{aligned} \alpha &= \delta + \theta \\ \beta &= \delta + \theta' \end{aligned} \tag{4.1}$$

According to the basic grating equation Eq. (1.5) and *Snell's law* [17], the grating equation becomes,

$$m\lambda = d\left(n\sin\alpha - \sin\beta\right) \tag{4.2}$$

where *m* is the number of diffraction order, λ the incident wavelength, *d* the grating period, and *n* the refractive index of the grism substrate The positive orders diffract clockwise with respect to the zero order, whereas the negative orders diffract counterclockwise. From Eq. (4.2) we see that in the $m = 0$ diffraction order, for which $\sin\beta = n\sin\alpha$, the diffracted beam is deflected as if it were being refracted at the surface of a smooth plate, instead of being refracted on an individual facet which is given by the condition $\sin\left(\beta - \delta\right) = n\sin\left(\alpha - \delta\right)$ [8].

Following *Snell's law* [17] and Eq. (4.2), the diffraction angle β can be given by,

$$\beta = \arcsin\left(n\sin\left(\arcsin\left(\frac{\sin A}{n} \right) + \delta \right) - \frac{m\lambda}{d} \right) \tag{4.3}$$

From the practical point of view, we shall seriously consider the design parameters of grism and thus the feasibility of implementing the 4D MCMI. The disadvantages of our former grism lie practically in the faulty design of grism mount, different sizes/shapes of grating (25mm×25mm squared) and prism (1 inch round) and hence the fragile cemented structure, the poor precision of cementing which maks the prism outerface and the grating facet unparallel, and the unstability of the 'long' relay system [2-4]. Since some of these shortcomings can be overcome by customizing the grism, firstly we will discuss a set of possible design parameters.

In order to minimize the alignment error, we begin by considering that any element in the optical system should be well assembled with the commercial opto-mechanical components. For ease of manufacture and use, a squared size of 25mm×25mm for both wedge prism and blazed grating is preferred. Accordingly, with a lower cost, a Thorlabs' blazed grating of part number 'GT25-03' is selected, such that the parameters of prism can be customized on the basis of that of grating. The main characteristics of blazed grating and wedge prism are shown in Table 4.1.

Table 4.1 Characteristics of customized grating and prism.

Items	*Blazed Grating*	*Wedge Prism*
Substrate Material	**Schott B270**	
Refractive Index @532nm	**1.5261** [18]	
Size	**25mm×25mm** (tolerance of +0.0/-0.1mm for prism)	
Wedge/Blazed Angle	**17.5 °**(angular tolerance of ±30arcsec for prism)	
Surface Quality of Polished Surfaces	**60-40 Scratch-Dig**	
Thickness	**3mm** (tolerance of ±0.5mm)	**3mm** (thin edge of wedge)
Dimensional Tolerance	**±0.5mm**	**±0.15mm**
Specialized Parameters	Grooves per mm **300**	Surface Flatness @532nm **λ/10**

Aside from the configurations introduced in Table 4.1, further treatments are also applied to achieve higher optical efficiency as well as optimum performance, such as making >90% of diameter of the prism aperture be clear and employing the 350-700nm antireflection (AR) coating on polished surfaces of the prism.

To verify the custom parameters of grism listed in Table 4.1, a ray-path model based on Fig. 4.3 is established using Mathematica software, which indicates that the grism is able to give an un-deviated wavelength of 527.3nm. In order to assess the performance from the point of visual sense, a ray-tracing model done by Zemax software is also performed and the results are in full accord with that of the Mathematica model, demonstrating that the grism pair can produce a collimated, chromatically displaced

output as Fig. 4.4 shown. The footprint of the beams at the output surface of the second grism is shown in Fig. 4.5, in which the blue, green and red colours indicate the wavelengths of 450nm, 532nm and 610nm, respectively. Furthermore, an optical efficiency in excess of nearly 70% with the undeviated beam could be achieved in experiment.

Fig. 4.4 A 'straight through' optical layout using a pair of grisms.

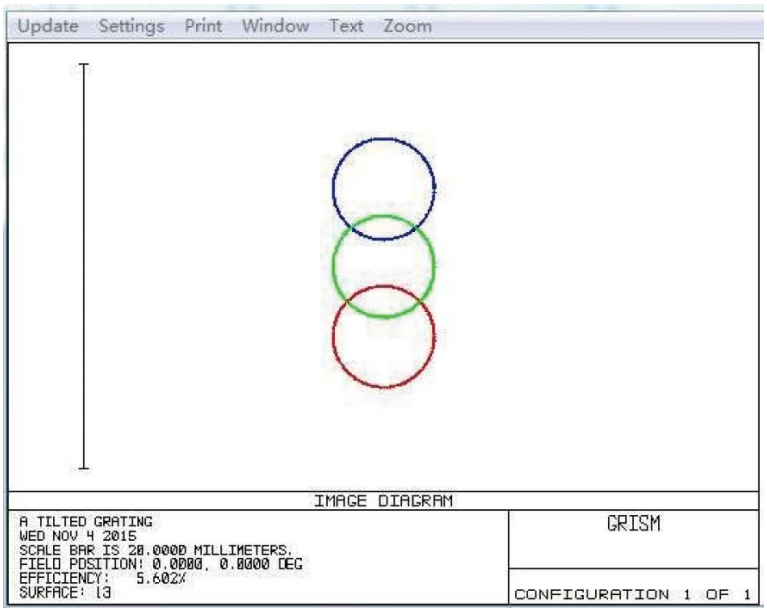

Fig. 4.5 Zemax footprint diagram for the output beam of grism pair.

The Zemax simulation is done by Dr. Zhengkun Liu of National Synchrotron Radiation Laboratory, University of Science and Technology of China.

4.2.2 Custom grism mount

As discussed above, in an attempt to align the multi-degree-of-freedom grisms system, a new design of the sufficiently rigid grism mounting is proposed instead of picking up the commercial off the shelf (COTS) opto-mechanical mounts. Due to the mutual excitation of different degrees of freedom, in the mechanical considerations of designing and making such a mount, we shall mainly be concerned with the motion(s)

of relatively higher alignment sensitivity. And in our case, the custom mounts should allow a precise, stable and easy-to-use alignment of grism thus an anticipated positioning of the multi-colour beam can be manually tuned. Taking the alignment sensitivity, stability, complexity, as well as our experimental experiences [2-4] into account, we present a design that the rotation of grism in the vertical direction with respect to the optical axis is finely adjusted using a lockable 360° rotation plate, whereas the horizontal rotation is nonadjustable to ensure the outer surfaces of grisms are perpendicular to the optical axis (as Fig. 4.4 shown). Another point to consider when building the 4D imaging system is making the custom mounts to be compatible with Thorlabs' opto-mechanical components, i.e. 30/60mm cage mounts and standard assembly rods/posts, such that the flexibility and stability of our compact optical relay system could be achieved.

Now we look further at the characteristics of the custom grism mount. According to the basic design idea that the mount should securely hold the grism whilst providing 360° of continuous rotation around the optical axis, we propose that the grism mount can be classified into 3 mechanically interconnected parts: holding mount, rotation plate and rack, which does not come with any adjuster knob for effective use in confined spaces. The centration of these parts is a bit critical (the concentricity is less than ±0.02mm) to minimize the system error(s), and all the parts are fabricated from black anodized aluminium to reduce unwanted reflections. The mechanical diagram of the custom mount (neglecting the threaded holes distributed around the rotation plate in the top-view and part of front-view for clarity), which indicates the three parts in different colours, is demonstrated in Fig. 4.6. In order to outline the main functions of the grism mount, only very typical dimensions are marked and the photos of the mount with front and back views (with the grism and a Throlabs' post mounted) are also attached at the bottom right of the diagram. Please note that some dashed/centre lines appear like thin solid ones in the mechanical drawing due to the limitations of line styles (and thus the display) of AutoCAD software.

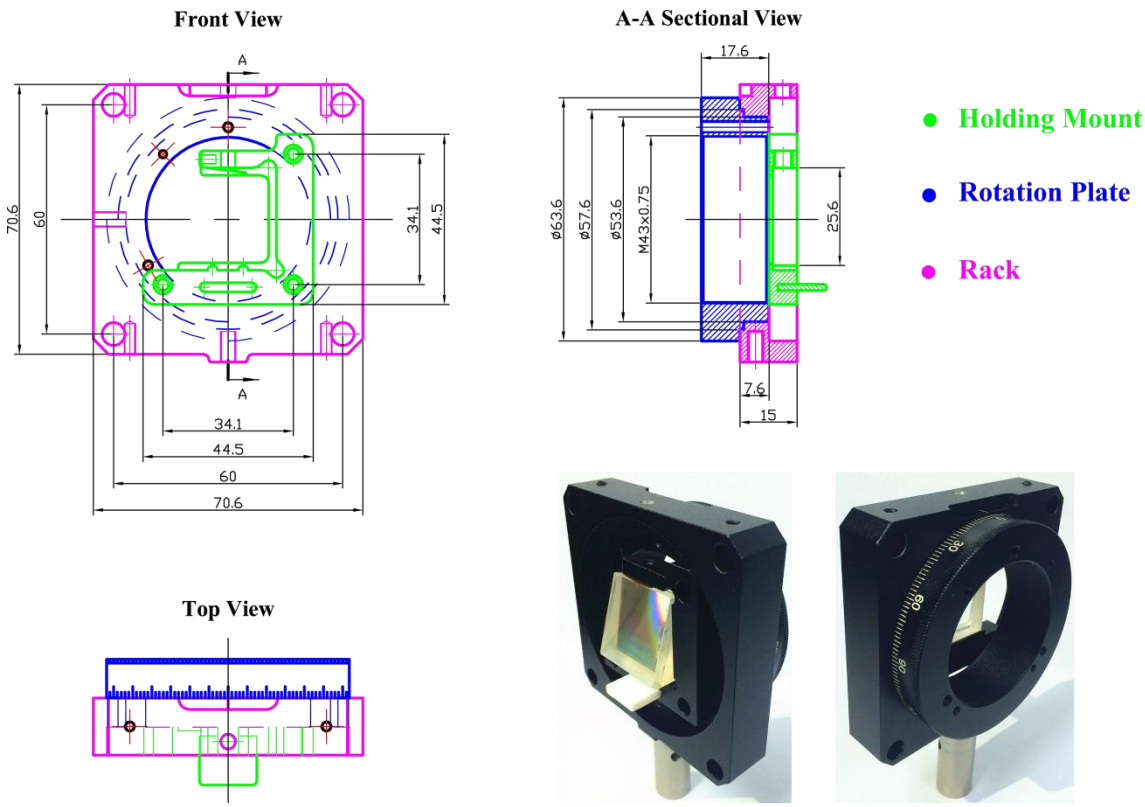

Fig. 4.6 Mechanical diagram and photos of grism mount.

To concisely introduce the design of the grism mount without tremendous details, only a schematic draft rather than the 'strict' mechanical assembly drawing is illustrated. Further descriptions of the three main parts are following:

The holding mount is uniquely designed for our grism which offers fixed optic height of 25mm, adjustable width of up to 36mm and sufficient depth of 6.4mm, such that the grism could be mounted in various orientations. With a nylon-tipped M2.5 setscrew and a flexure clamp, the grism is stably held in the mount where the setscrew presses the flexure clamp against the edge of the grism to create a secure area of contact. This holding mount is then fixed on the rotation plate that engages three mounting screws in the counterbores at the top right corner and bottom corners, whilst the fourth (top left) corner is cleared for operation within the mount. To securely protect the grism, two little sticks (length of 6mm and diameter of 2mm) are laid at the bottom of the grism within the mount for pressure buffering, and a protection bar with length of 14.9mm, width of 12.8mm and thickness of 2.4mm is inserted into the outer surface of the mount for protecting the fragile grisms from collision when they are very close to each other. Both the sticks and the protection bar are made from Teflon. This holding mount

should also be mechanically compatible with 25mm tall rectangular optics which is at least 3mm thick.

The rotation plate is a compact platform that comes with an annular dial and evenly distributed internally threaded holes, thus allowing us to easily fix the removable holding mount at three points on the back of it by using M3 mounting screws. It provides 360 ° coarse rotation and is labelled every 30 ° with 2 ° graduations on dial, while the smooth rotation mechanism can be manually operated to any position and locked by a M4 locking capscrew once the desired position is reached. The large annular dial with the inner diameter of 53.6mm provides the maximum aperture available for use within a cage system. The annual dial is also internally threaded and a few small internally threaded holes are distributed on the dial plate, thereby other mounted optics might be applied.

The rack mounts the rotation plate into it by a special technology called ‘grind assembly’, which is a type of interference fits and the last step of procedure is purely handmade to minimize the roundness and concentricity errors, as well as ensure the firm and smooth adjustment. Subsequently the holding mount is also embedded into the large aperture (63.6mm in diameter) of it via rotation plate so that the grism may be protected in this inner space from any misoperation during the alignment. With a bottom-located M4 tapped mounting hole and four Φ6 through-holes in the corners, the rack is compatible with Thorlabs standard TR series posts, ER series rods and 60mm cage system. The side-located M4 counterbore enables the rotation plate to be locked by a setscrew which is made of a composite material of nylon and polyvinyl chloride (PVC) for stably locking and protecting the rotation plate against scratching. The top through-hole enables a M2.5 hex key to go through and fix the grism within the mount.

From the above discussion on the significant design criteria of our custom grism mount, it is evident that the manually-actuated mount is convenient and low-cost, and its slim overall profile makes it ideal for use with compact optical assemblies. Furthermore, there is great flexibility in these designs to provide other potential motions, i.e. the rotation of the mount in the horizontal direction with respect to the optical axis can be achieved when it is attached on a Thorlabs’ rotation platform. Although the alignment tolerances are presently difficult to achieve and maintain, the custom mount

works sufficiently well for our initial attempts and further optimization might be developed if high precision alignment is required.

YF acknowledges Mr. Qiang Zhang and Mr. Shengli Lu of Beijing Shinehe Technology Co. Ltd. for the advice of mechanical design and the fabrication of grism mounts.

4.3 Chromatic imaging tests of grism pair

We propose to use a pair of grisms for correcting the chromatic smear induced by the QD grating, consequently quantifying and controlling the lateral shear produced by grisms is significant (see Fig. 4.1 and Fig. 4.4). The Mathematica and ray-tracing models illustrated in subsection 4.2.1 reveal some characteristics of grisms. However, due to the likely effect of both the fabrication errors of grisms and the optical system errors, experimentally assessing the chromatic shear using a polychrome input beam should be of practical importance. In this section a series of tests are conducted to find the relation between the chromatic smear and the grism separation, and the experimental results will be compared with the theoretical conclusions for further consideration.

4.3.1 Experimental setup

Consider the case that the grisms are mounted back to back (see Fig. 4.4) in custom mounts within an assembly using Thorlabs' opto-mechanical components, as shown schematically in Fig. 4.7.

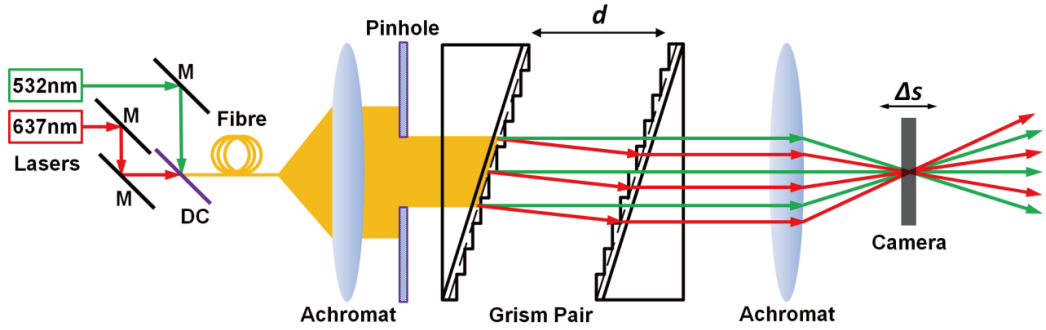

Fig. 4.7 Schematic of polychromatic ray paths of the grism-achromat combination.

Two lasers, of wavelengths 532nm and 637nm (both are calibrated by spectrometer), are coupled successively through a few neutral density (ND) filters, 3 mirrors (M), a dichroic mirror (DC) and a Newport singlemode fibre coupling kit #9131-M (ND filters

and Newport #9131-M are not shown in Fig. 4.7), and feed through an optical fibre (Thorlabs P1-488PM fibre, available in wavelength ranges from 460nm to 700nm) to provide a compact polychromatic source. The light from this fibre is evenly collimated by an achromat with focal length of 60mm and an approximately 3mm diameter beam can be obtained when a pinhole is implemented. Then the collimated beam is refocused by a second achromat (focal length 250mm) chosen to give well-sampled images with the 6.5μm pixels (Andor Zyla 4.2 sCMOS), and the separation between the two achromats is 250mm to offer adequate space for varying the grism separation. A schematic of the grism configuration is also illustrated in Fig. 4.7, and in our experiments a Zolix optical rail allows for the grism separation to be varied smoothly, to within an accuracy of approximately ±1mm, over a range from 2mm to 212mm between the inner faces of the grisms, the lower figure selected to protect the fragile blazed gratings from contacting against each other at close proximity and damaging the surfaces whereas the higher figure is approaching the practical marginal value due to the limited numerical aperture of the optical relay system. The sCMOS camera is mounted on a Thorlabs' manual translation stage for moving back and forth along the direction of optical axis.

4.3.2 Chromatic image experiments

As discussed above, the grism pair proposed here will be applied in tests for the easily-varied chromatic dispersion. Building an optical system as Fig. 4.7 shown, a pair of identical, back to back grisms is used to produce a collimated beam with chromatic shear from a collimated polychrome input, hence the lateral shear between the polychrome components in the output beam is controlled by varying the separation between the grisms. Images with both lasers incident can be recorded as a function of camera position as the camera is translated ±10mm either side from the 'best focus' image plane for variety of grism separations. The ND filters are adjusted so that both laser lines are matched in intensity and, in combination, do not saturate the camera.

In order to systematically explore how the chromatic dispersion changes as the grisms moving backwards and forwards, we firstly fix the grism separation, translate the camera through the 'best focus' image plane and record the laser spots. Then this process is repeated with a set of grism separations, as Fig. 4.8 demonstrated.

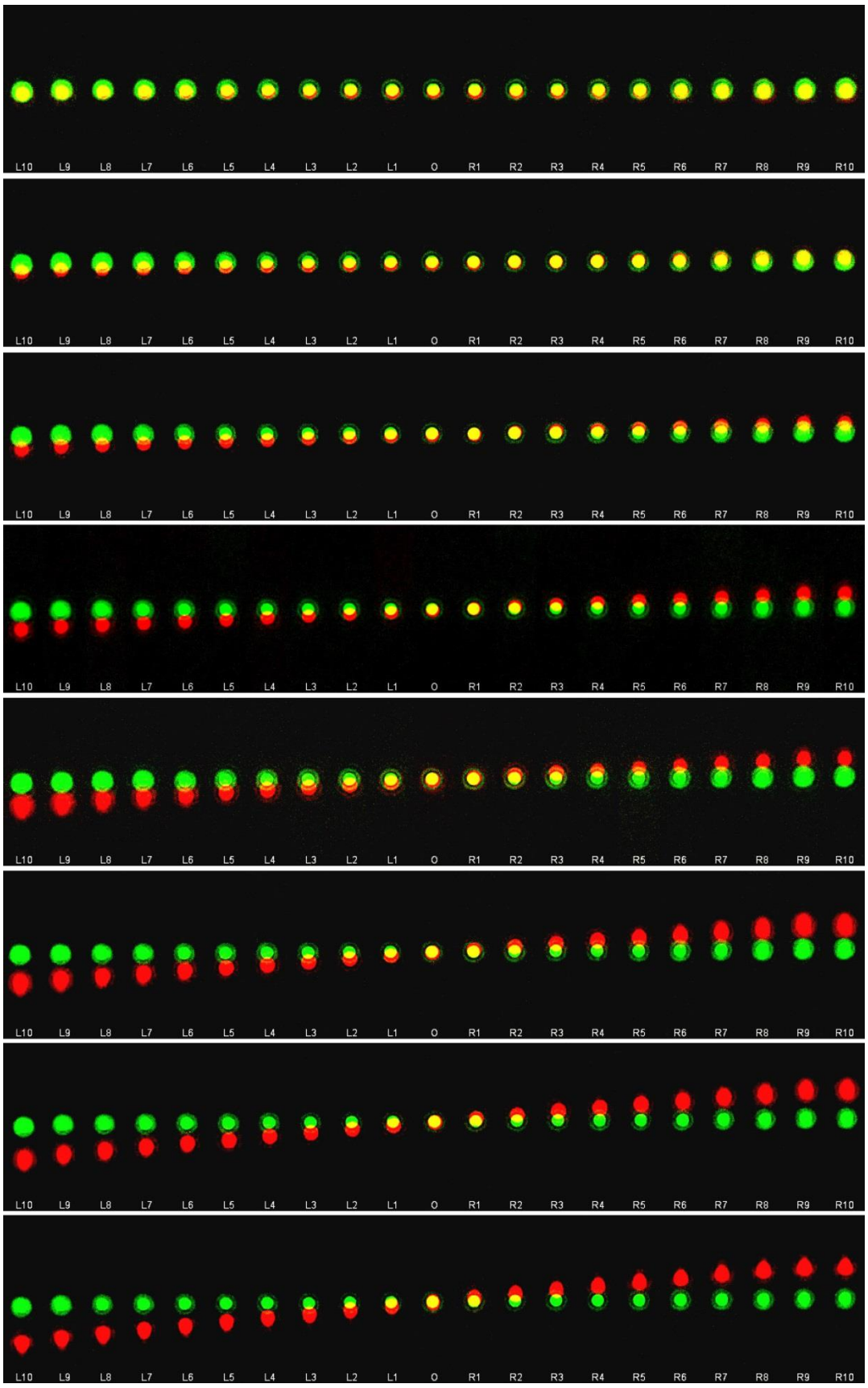

Fig. 4.8 Each false-colour montage showing the separation of the image of the fibre source in each laser line as a function of camera distance from 'best focus'. The grism separations from top to bottom are 2mm, 32mm, 62mm, 92mm, 122mm, 152mm, 182mm and 212mm, respectively.

where the labels on the bottom of each montage indicate the positions of camera plane — 'O' marks the 'best focus', 'L'/'R' represents left/right side of the camera from 'O', and the numbers indicate the distance between 'O' and camera plane (in mm). For example, 'L3' means that the camera plane is 3mm away from 'best focus' on the left side. It can be seen from Fig. 4.8 that there is a clear shift of the 637nm spot relative to the 532nm spot, whereas the 532nm spot remains largely fixed as it is very close to the designed un-deviated wavelength (~527nm) of the grism pair.

To quantitatively analyse the relation between chromatic smear and grism separation, the position (geometric centre) of each spot in Fig. 4.8 has been measured, thus the lateral spot separation between the two lasers can be calculated and plotted as a function of camera position, as shown in Fig. 4.9. Since the longitudinal displacements of the two spots at each camera position, which may be caused by alignment error of optical system, is very little (~1 pixel), the spot separations demonstrated in Fig. 4.9 only refers to the lateral displacements rather than *Euclidean distances*.

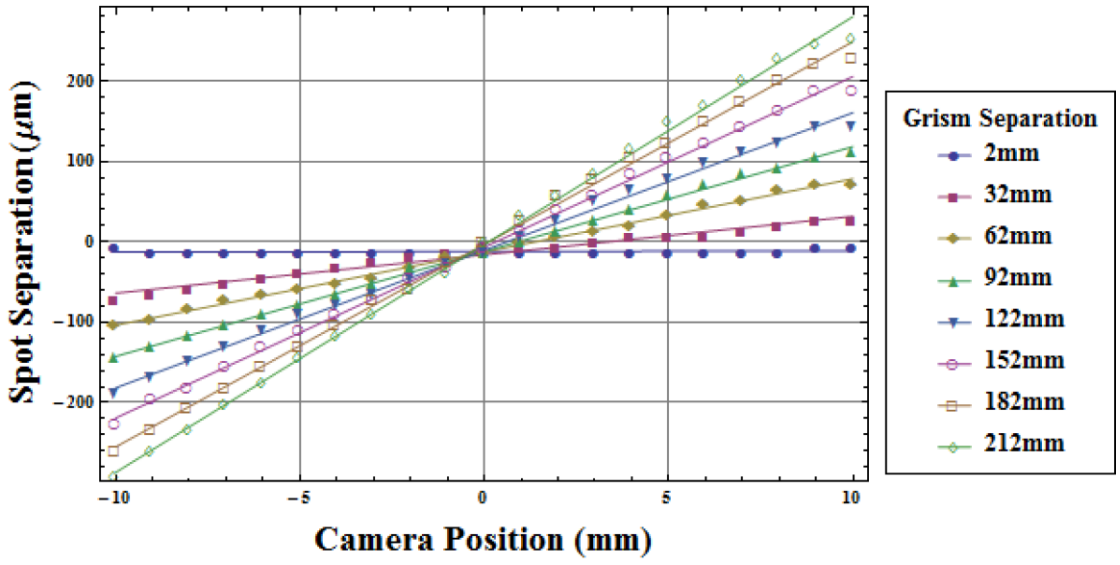

Fig. 4.9 The image separation of the polychromatic lasers as a fuction of camera position for various grism separations, using data in Fig. 4.8.

By repeating the measurements as a function of grism separation, the angle of arrival of chromatic components can be estimated and, using the focal length of the imaging lens, the spatial chromatic shear produced by the grism separation can be deduced. Fig. 4.10 shows that 0.0338mm shear between the laser beams per millimeter separation can

be obtained, which is equivalent to 322μm shear per nanometer bandpass per millimeter of grism separation.

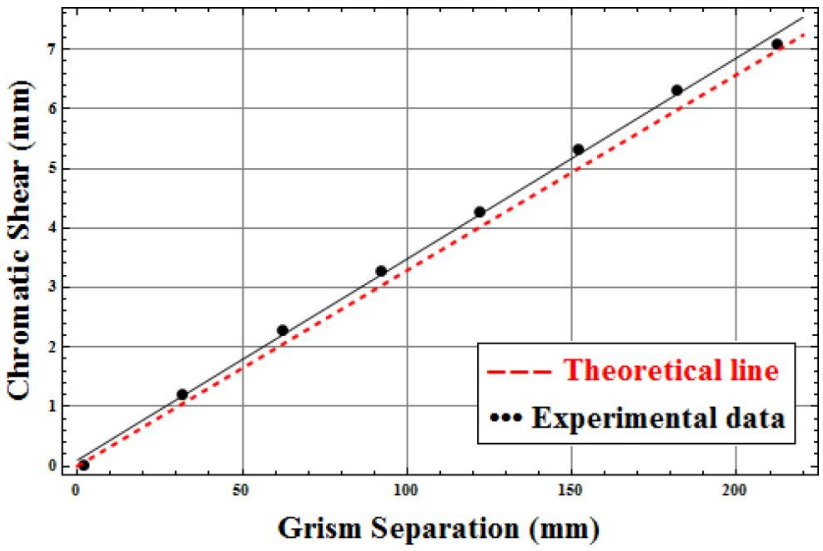

Fig. 4.10 The spatial chromatic shear produced by varying grism separation and deduced from Fig. 4.9 using the focal length of the second achromat.

It is convenient to compare this experimental data with the principle value deduced from the mathematical model illustrated in subsection 4.2.1. As Fig. 4.10 shown, we find that the difference between the slopes of experimental fit line (black solid) and theoretical line (red dashed) is only 0.9‰, which indicates the well-designed and fabricated grisms and the well-adjusted optical relay system, and from practical point of view, the potential for chromatic tuning using an on-axis grism pair.

4.4 4D imaging tests of grism and QD grating combination

As illustrated in section 2.1.2, 4D imaging using a QD grating is based on the simultaneous focus of multiple object planes on a single image plane using a simple, on axis optical setup. The QD grating imparts a different focusing power in each diffraction order, with a linear dependence of focal length on incident wavelength. However, the QD grating introduces a natural chromatic smearing in the non-zero orders. In our previous work narrow-band filters, ~10nm, have been used to reduce this effect to a few camera pixels. Unfortunately, this still induces some chromatic smearing and significantly reduces available photon flux, thus restricting practical biological applications. However, by definition the period of QD grating is linearly chirped along one axis, and that chirp can be used to our advantage. By pre-dispersing the polychrome input beam using the grism pair, each incident wavelength is positioned

within the chirped zone plate to 'see' the same structure of QD grating measured in wavelength units. This pre-dispersion thus equalises the angle of diffraction for each wavelength, giving non smeared, 'white light' images in all diffraction orders (see Fig. 4.1).

4.4.1 Experimental setup

To test the grism correction in QD grating based 4D imaging we mounted the grism pair between two 250mm achromatic lenses, as shown in Fig. 4.11. A continuum laser (Fianium supercontinuum light source SC450-PP-HE, operating wavelength ranges from approx. 450nm to >1750nm) fed through a single mode optical fibre (Thorlabs P1-488PM) was utilized instead of dual lasers for qualitatively describing the wide-range chromatic correction capability of grism system. The achromats, spaced 200mm apart, operated as a unit magnification relay system with an effective focal length of ~208mm. When the QD grating was placed 208mm from the second principal plane (~42mm from the second achromat) of the compound imaging system equal magnification images were obtained in each diffraction order, providing simultaneous multi-plane imaging due to the order dependent focusing power introduced by the QD grating [1, 6, 19]. Because of the diffraction generated by straight edges of slit, we still used a pinhole as aperture stop and an approximately 3mm diameter beam was obtained. Note that only the spacing between the two grisms is relevant, not their absolute position between the achromat pair.

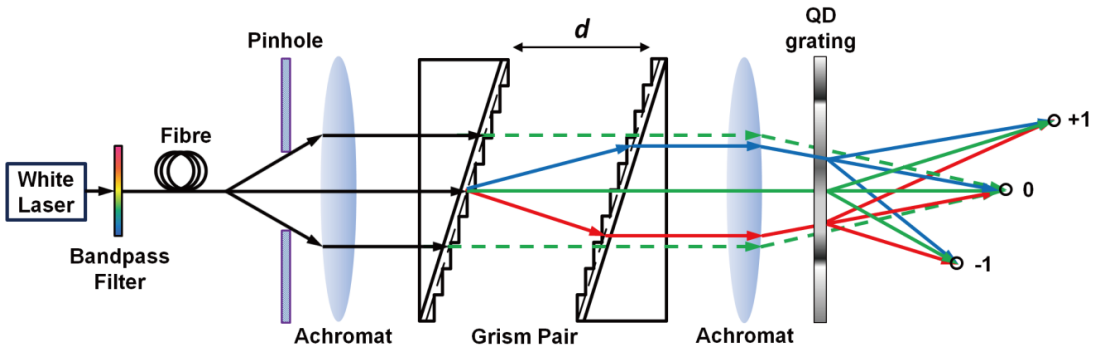

Fig. 4.11 Schematic of the grism system used to correct chromatic blur in a 4D imaging system using a QD grating.

The 3 foci shown on the right of Fig. 4.11 illustrate the position of focus of the single fibre source in each diffraction order and when the single source position is fixed. On a single, flat camera plane each diffraction order is focussed on a different specimen plane

and the 3 foci are recorded simultaneously. In our measurements the QD grating has a nominal axial period of 50μm, a curvature W_{20} of 50 waves and radius 10mm, thus has ±1880mm focal lengths in the first diffraction orders at 532nm wavelength.

Before conducting the chromatic correction experiment illustrated by Fig. 4.11 (here we call it 'rainbow test'), a few tests with the dual lasers system (532nm & 637nm) are performed as section 4.3 described for simply calibrating this imaging system. Following our Mathmatica model of grism-grating combination system, a chromatic shear of 37.6μm per nm of bandpass is required across the QD grating in order to equalize the angle of dispersion across the optical bandpass. For the 105nm bandpass between the dual lasers used, the total chromatic shear required between the two beams is thus 3.95mm. This is the shear required at the QD grating, allowing for the beam convergence to the camera, this corresponds to 4.74mm of shear before the final lens. Thus a grism spacing of 140mm was chosen to correspond to this shear. Again as previously described, we changed the image distance (thus moving the camera along the optical axis) to observe the chromatic dispersion between the two laser spots. The images of first three diffraction orders (-1st, 0th and +1st) were recorded at the image distances of 407mm, 417mm and 427mm separately, with and without using the grism system. Since images of the 3 orders should be snapped on a single camera plane in real microscopy imaging, we cropped the focused image of each order and re-combined these 3 images together as Fig. 4.12 shown, from which we see that the chromatic smear can be obviously corrected when the grisms are introduced. Here the total integrated images intensity has been equalised in each colour band.

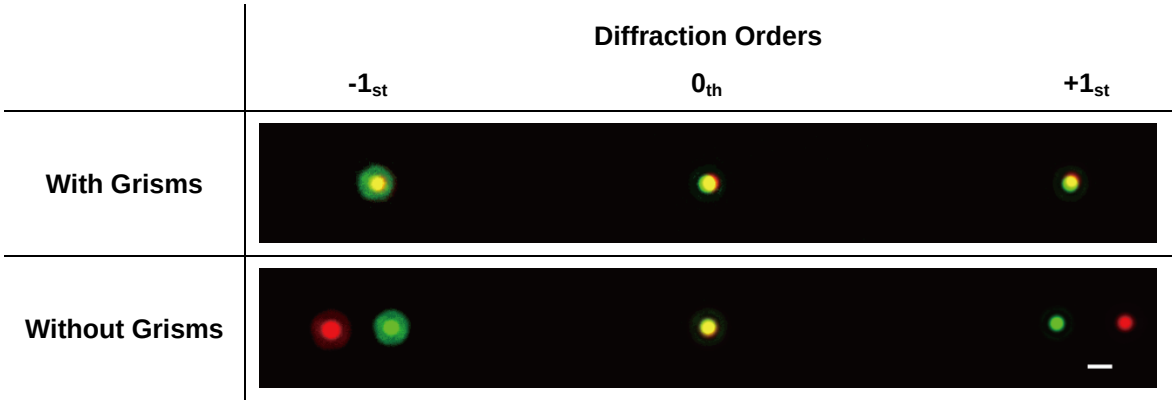

Fig. 4.12 False colour images snapped at varied image distances, with and without grisms correction. Scale bar: 1mm.

Now we turn our attention to a more practical case: imaging multiple object planes onto a single image plane. Since a single polychromatic source was used in these experiments, we just needed to scan the source position to record the 4D foci in the different diffraction orders whereas keeping all the other optical parameters constant. Again the images of the first 3 orders were focused successively and recorded with and without grism correction. Fig. 4.13 demonstrates the chromatic correction of all the 3 diffraction orders on a single camera plane — the object distances are 440mm (-1st order), 417mm (0th order) and 394mm (+1st order), respectively.

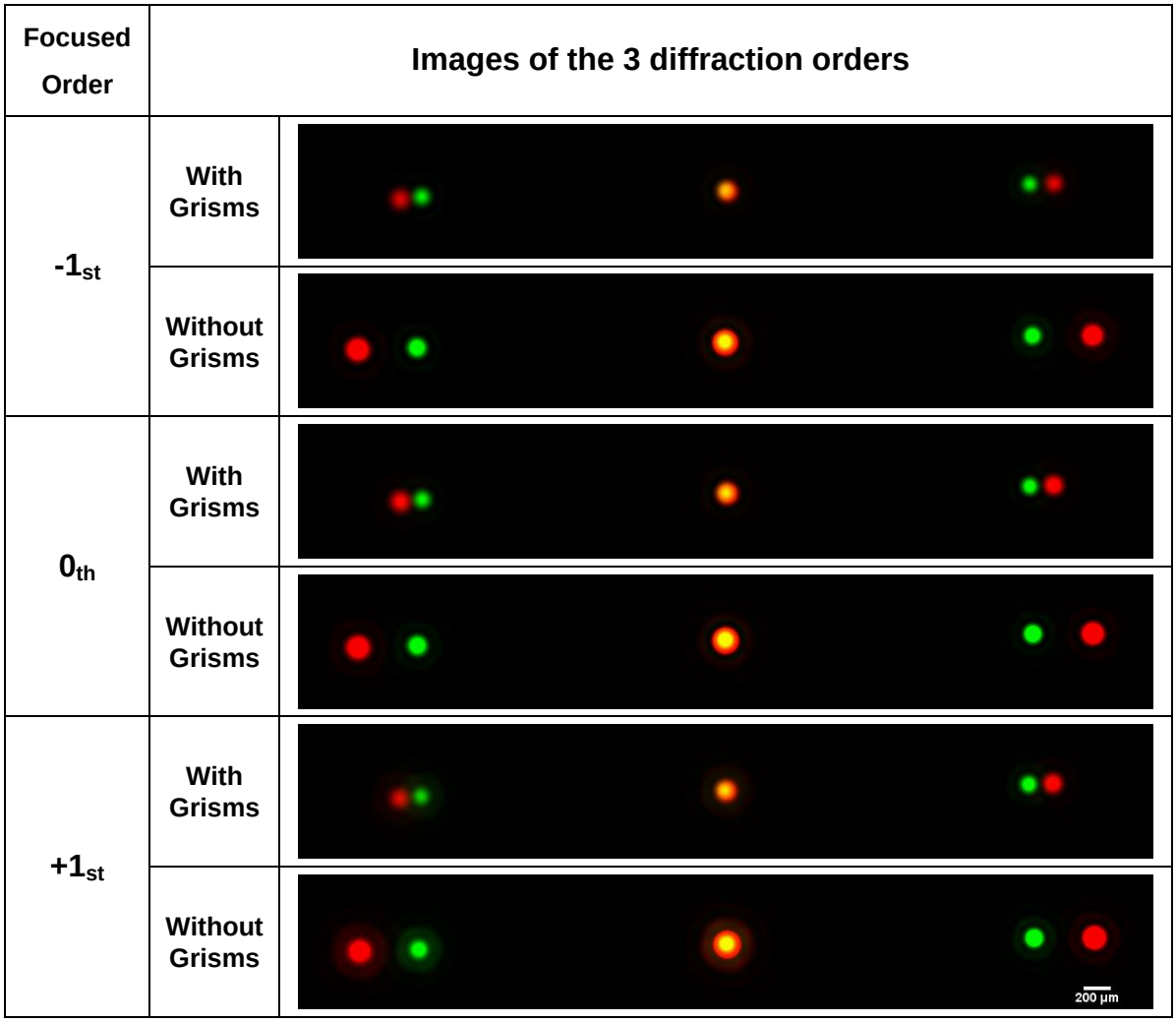

Fig. 4.13 False colour images snapped at varied object distances, with and without grisms correction.

Comparison of top and bottom images of each order in Fig. 4.13 shows that the chromatic smearing of first orders is reduced by a factor of ~2.5, rather than 'complete' correction as expected. For further exploring the chromatic correction capability of grism system, the colour band will be expanded to white light range (440nm~660nm).

4.4.2 Yan's rainbow

Due to the inherent dispersion property of grating, the incident white light diffracted into non-zero orders can be splitted into its constituent spectral colours, thus a series of colour bands which look like rainbows are generated. In the following experiment, a high power fibre continuum source (Fianium SC450-PP-HE) filtered by a set of 20nm bandpass filters (Thorlabs) with central wavelengths from 450nm to 650nm in 20nm steps were implemented. Since one of the main experimental phenomena is the colour of rainbow, I label it following my name — *Yan's rainbow*, which is supposed to specify the multi-colour images introduced by the QD grating with/without grism correction (see Fig. 4.14).

For precise comparison, we maintained the optical setup as previously demonstrated (see subsection 4.4.1, i.e. grism separation of 140mm), and varied the object distance to explore the chromatic correction extent of grism system using white light. Since the image quality is dominated by a residual λ dependence of the focal length of the QD grating when broadband light was implemented [1], for demonstrating the true range of the chromatic correction an appropriate focal length of first diffraction order might be selected carefully. It had been found that, for the QD grating we chose (a nominal axial period of 50μm, a curvature W_{20} of 50 waves and radius of 10mm), the focal lengths of first diffraction orders were as large as ±1880mm at 532nm wavelength, which indicated that we did not need to reposition the light source at each bandwidth to compensate for the QD grating induced focal dependence [2] as the focusing power at each wavelength may vary little in a reasonable small range of object distances (a few millimeters in this case). Therefore the system was only focused for the un-deviated/central wavelength of ~532nm in the first 3 diffraction orders respectively (thus the object distances of -1st, 0th and +1th orders are 440mm, 417mm and 394mm, respectively), with and without grism correction. Each greyscale image captured by the sCMOS camera (Andor Zyla 4.2) was then normalized for equal total photon flux at each waveband using ImageJ software, and falsely coloured using Mathematica software by means of calculating the RGB value of each central wavelength, normalizing each image for compatibility with RGB, creating coloured images using R, G and B scalers, and compositing a coloured image of a single wavelength. Finally the images of all the 11 wavebands were combined together and thus formed the colour of rainbow, as Fig. 4.14 shown.

Focused Order		Images of the 3 diffraction orders
-1_{st}	With Grisms	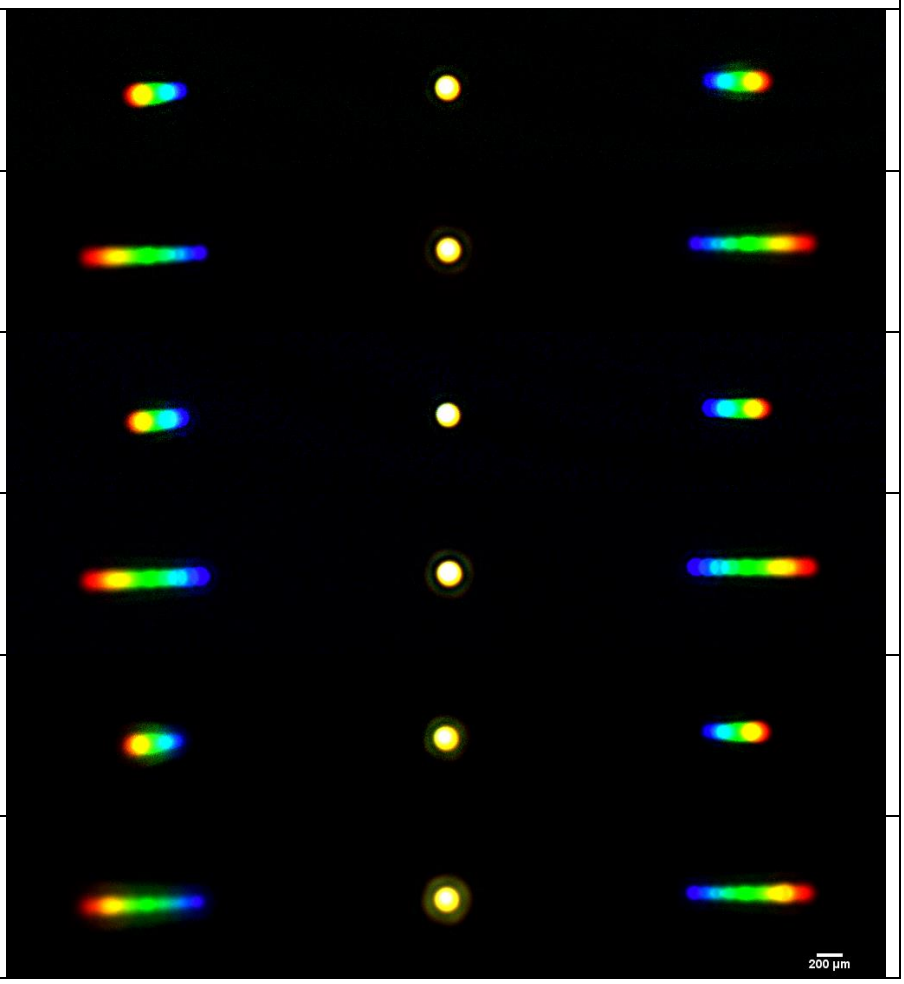
	Without Grisms	
0_{th}	With Grisms	
	Without Grisms	
$+1_{st}$	With Grisms	
	Without Grisms	

Fig. 4.14 Yan's rainbow.

Yan's rainbow demonstrates the successful use of the grism pair for chromatic correction of the QD grating. It is evident that the chromatic smearing of first orders is effectively improved by the grisms but not enough eliminated as expected, whereas the 0th order image is unaffected by both the QD grating and the grisms (but excluding the photon flux) as it inherently has no chromatic distortion. Due to the well performed grisms and their mounts (Fig. 4.10), the reasonable accuracy of optical alignment (~1mm) and high repeatability of the experimental results, the residual chromatic smearing of first orders may be attributed to the fault(s) of our Mathematical model of grism-grating combination system (Mathematica codes are not shown in this dissertation) — accordingly an inaccurate grism separation may be attained. We have been trying all our best to revise/optimize the theoretical model and, at the same time, the biological applications may not be hindered as the entire visible spectrum is always

not needed in most of the imaging processes and the rainbow experiment can be exploited for calibration under certain condition(s).

Let us now take a simulation test in fluorescence microscopy for example. We simulated the performance of the grism correction to fluorophore imaging by modifying the bandpass filtered white light (i.e. rainbow experiment for certain bandwidth) and simply summing a series of images spanning the fluorophore bandwidth (from 480nm to 600nm), with an appropriate weighting to mimic the fluorophore spectrum. Importantly, the limiting bandwidth of most fluorophores and the fluorophore spectral profile, combined with the grism correction, effectively removed the image blurring due to the λ dependence of the focal length of the QD grating. As an illustration we have chosen to model eGFP fluorophore, which is widely used in cell biology. The optical system was focused and aligned for the filter that best matched the peak fluorophore wavelength of 520nm. With the source position fixed for the fluorophore (here only 0th order image was adjusted in focus), a series of narrow band images were then recorded using a set of spectral filters covering the fluorophore emission spectrum. The spots corresponding to the individual filters are clearly visible. To process the images, the total flux for each filter is first normalized to the total flux at the peak wavelength and then weighted to simulate the fluorophore spectrum by the appropriate factor [2]. The composite 'fluorophore' images for the simulated eGFP fluorophore, with and without grism in place, are shown in Fig. 4.15.

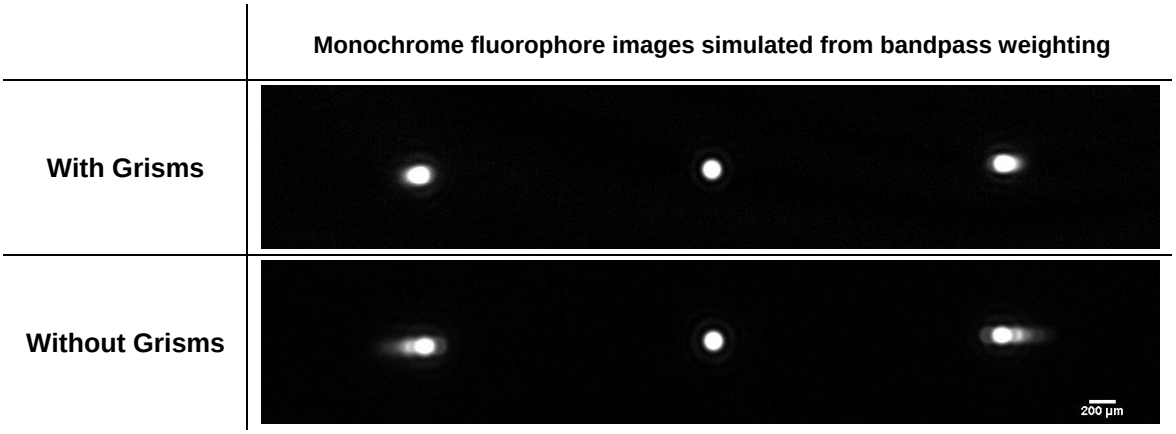

Fig. 4.15 Simulation of chromatic correction applied to eGFP fluorophore imaging.

Once again chromatic smearing is effectively improved for such a broad bandwidth of 120nm, although minor imprecision occurs in the red wavebands (top image in Fig.

4.15). It is reasonable to conclude that this optical system could be straightforwardly applied to measure some dynamic biological procedures which are not sensitive to the shape of objects, such as single particle tracking for analysing the diffusion of cells [20]. Or for reconstructing the exact 4D images of cells, the results of rainbow experiment, which are obtained in the same condition with biological imaging (i.e. same waveband and photon energy distribution), may be taken as reference so that the distortion of first order images can be corrected by post-image processing technique(s).

By now we have successfully developed a chromatic correction scheme using a pair of grisms for QD grating based 4D MCMI system, which, for the first time, achieves chromatically-corrected, high-efficiency, easy-to-use, and simultaneously imaging of first three diffraction orders.

4.5 Discussion

The simple control using a grism pair permits the correction of chromatic smearing in QD grating based 4D MCMI system and improves control of the axial profile of a focussed spot in multi-photon experiments. Although this grating-grism system had been presented earlier [2-4], it only corrected the chromatic smearing for a single diffraction order each time and, the optical system was extremely unstable and far too difficult to align, which hindered its application in microscopy imaging. Similarly to the grism design we did before, our grisms are also drawn to give an un-deviated wavelength in the mid visible where many biologically-useful fluorophores emit. This grism pair is used in tests to achieve a collimated output beam firstly and we can assess the chromatic shear produced as a function of the grism separation by measuring the angle at which two different laser wavelengths are brought to focus as a function of the grism separation. We then demonstrate correction of dispersion in 4D imaging of a compact polychromatic source using QD grating and the measured performance of our grisms is also compared with the theoretical value calculated by ray-path model. It seems that the chromatic smearing can be effectively improved for a reasonable broad bandwidth of ~80nm, yet further investigation of the theoretical model of grating-grism system is still essential.

The two sets of tests presented in sections 4.3 and 4.4, demonstrate the ease with which grisms of this design can be incorporated into complex optical systems in order to achieve a variable chromatic shear on an input beam without changing the

convergence properties of the beam. This is verified by considering, for the 4D imaging system, that the position of the in-focus images in different colour, is entirely consistent with the expected shift in focus evaluated from the chromatic variation of the QD grating focal length.

The chromatic focus control used to evaluate the chromatic shear as a function of grism separation can also be used to achieve control of the 4D field distribution at focus. The chromatic corrections achieved here can be effected with blazed gratings that deviate the beam [1], but such systems are difficult and expensive to maintain in alignment, whereas the system described uses a simple sliding mechanism and thus provides a significantly more practical solution.

For the long term, work will focus on optimizing both the structure of grism and the relay design of optical system. Most importantly, to build a practical mathematical model of grism-grating combination system, more complex consideration would be involved, i.e. deviation from linearity in the grism dispersion, mis-placing the optical component(s), spherical aberration, and further, chromatic correction of 9-plane 4D imaging, the details of which may be published in the near future.

4.6 References

[1] P. M. Blanchard and A. H. Greenaway, *Broadband simultaneous multiplane imaging*. Optics Communications **183**(1), 29-36 (2000).

[2] Y. Feng, P. A. Dalgarno, D. Lee, Y. Yang, R. R. Thomson and A. H. Greenaway, *Chromatically-corrected, high-efficiency, multi-colour, multi-plane 3D imaging*. Optics Express **20**(18), 20705-20714 (2012).

[3] Y. Feng, P. A. Dalgarno, D. Lee, A. H. Greenaway, Y. Yang and R. R. Thomson, *Optical system*. in UK Intellectual Property Office. UK Patent Application No. GB2504188-A, (Marks & Clerk LLP Edinburgh Office, United Kingdom, 2013).

[4] Y. Feng, *Optimization of phase gratings with applications to 3D microscopy imaging*, A dissertation for the degree of Doctor of Philosophy, Precision Instruments and Machinery, University of Science and Technology of China, Hefei, China (2013).

[5] M. Born and E. Wolf, *Principles of optics*. Cambridge University Press, Cambridge, Corrected reprint of the 7th edition, (2001).

[6] P. M. Blanchard and A. H. Greenaway, *Simultaneous multiplane imaging with a distorted diffraction grating*. Applied Optics **38**(32), 6692-6699 (1999).

[7] Y. Feng, L. Scholz, D. Lee, H. Dalgarno, D. Foo, L. Yang, W. Lu and A. Greenaway, *Multi-mode microscopy using diffractive optical elements*. Engineering Review **31**(2), 133-139 (2011).

[8] W. A. Traub, *Constant-dispersion grism spectrometer for channeled spectra*. Journal of the Optical Society of America A **7**(9), 1779-1791 (1990).

[9] S. Kane and J. Squier, *Grism-pair stretcher–compressor system for simultaneous second-and third-order dispersion compensation in chirped-pulse amplification*. Journal of the Optical Society of America B **14**(3), 661-665 (1997).
[10] K. Glazebrook, *LDSS++ commissioning report*. AAO Newsletter **87**, 11-15 (1998).
[11] G. J. Hill, M. J. Wolf, J. R. Tufts and E. C. Smith, *Volume phase holographic (VPH) grisms for infrared and optical spectrographs*. Paper presented at Astronomical Telescopes and Instrumentation, International Society for Optics and Photonics (2003).
[12] E. A. Gibson, D. M. Gaudiosi, H. C. Kapteyn, R. Jimenez, S. Kane, R. Huff, C. Durfee and J. Squier, *Efficient reflection grisms for pulse compression and dispersion compensation of femtosecond pulses*. Optics Letters **31**(22), 3363-3365 (2006).
[13] K. Nakajima, N. Ebizuka, M. Iye and K. Kodate, *Optimal fabrication of volume phase holographic grism with high efficiency and high dispersion, and its applications for astronomical observation*. Paper presented at Astronomical Telescopes and Instrumentation: Synergies Between Ground and Space, International Society for Optics and Photonics (2008).
[14] T. H. Dou, R. Tautz, X. Gu, G. Marcus, T. Feurer, F. Krausz and L. Veisz, *Dispersion control with reflection grisms of an ultra-broadband spectrum approaching a full octave*. Optics Express **18**(26), 27900-27909 (2010).
[15] N. Ebizuka, K. S. Kawabata, K. Oka, A. Yamada, M. Kashiwagi, K. Kodate, T. Hattori, N. Kashikawa and M. Iye, *Grisms developed for FOCAS*. Publications - Astronomical Society of Japan **63**(Special Issue: Exploring the Universe with the Subaru Telescope: From Galaxies to the Solar System), S613-S622 (2011).
[16] C. A. Palmer, E. G. Loewen and R. Thermo, *Diffraction grating handbook*. Newport Corporation Springfield, OH, 6th edition, (2005).
[17] E. Hecht, *Optics*. Pearson Education, Addison Wesley, San Francisco, 4th edition (International edition), (2002).
[18] RefractiveIndex, http://refractiveindex.info/, Access date: 19 Jan., 2015.
[19] S. Djidel, J. K. Gansel, H. I. Campbell and A. H. Greenaway, *High-speed, 3-dimensional, telecentric imaging*. Optics Express **14**(18), 8269-8277 (2006).
[20] A. Kusumi, ., Y. Sako, . and M. Yamamoto, . *Confined lateral diffusion of membrane receptors as studied by single particle tracking (nanovid microscopy). Effects of calcium-induced differentiation in cultured epithelial cells*. Biophysical journal **65**(5), 2021–2040 (1993).

Chapter 5

Initial bioimaging tests of 4D MCMI system

Preface

In this chapter, for practical use, some considerations of the combination of 4D MCMI system, commercial microscope and standard cameras are proposed. Then a few initial bioimaging tests have been performed, but we only concentrate on the optical performance rather than the bioprocess for now. Further optimization of the whole imaging system is still in progress to improve the stability of optical relay as well as implement the 4D MCMI technique for real biological research.

5.1 Introduction

In modern optical bioimaging, the photons can now routinely be detected by microscope imaging techniques through absorption, emission (fluorescence), scattering, or combinations using labelled systems [1, 2]. Most optical imaging technologies are applied to two-dimensional cellular context, which is defined by hard and flat surfaces, i.e. coverslips. Take the most common tools for example: biological imaging is traditionally dominated by wide-field imaging techniques, which illuminate the entire thickness of the specimen and capture the full field of view in a single exposure thus cellular information is obtained from only a single focal plane. Since the observation of three-dimensional biological specimens has been an increasing need for basic biological research as well as clinical diagnosis and therapy, it is vital to extend these techniques into the third dimension, ideally with a multi-spectral capability, so that dynamic interactions between two or more components can be studied in whole living cells. A variety of methods have been proposed, in which confocal fluorescence microscopy [3] has become a standard tool for 3D biological imaging by means of optical sectioning. Unfortunately, the limited temporal resolution is one of the significant drawbacks of conventional microscopy, especially when fast dynamical processes are required to be followed. Even worse, the spatial and temporal resolutions are mutually opposed to one

another, and the temporal resolution is always sacrificed for seeing fine structural details.

We have demonstrated a simple, on axis 4D MCMI technology that delivers real-time 3D imaging over cellular volumes, as described in preceding chapters. Our technique utilizes a QD grating, in the form of an off axis-Fresnel zone plate, to image multiple object planes simultaneously on a single image plane [4], which has been used in all wide-field imaging modes, e.g. bright-field, fluorescence, phase-contrast etc. It is compatible both with particle localization and tracking and with full-field, 3D, deconvolution-based specimen reconstructions from z-stacks. Z-plane separations of multi-focal images obtained using the QD grating based system can be varied from arbitrarily small to many microns (see Eq. (2.18)). For full-field imaging, Nyquist z-plane separations allows for volumetric data to be gathered up to 9 times faster, through the simultaneous acquisition of multiple, in-focus specimen planes. Alternatively, by utilizing the defocussed information contained within multiple specimen planes, single particles can be tracked and localized to sub 10nm axial accuracies through full cell (10μm) volumes using 9-plane and modest plane separations. Due to the need to limit chromatically-induced lateral smearing, a pair of grisms has been applied to create a collimated beam in which the spectral components are laterally displaced, as demonstrated in Chapter 4.

In this chapter, our QD grating and grisms based 4D MCMI system will be implemented to the practical bioimaging tests.

5.2 Practical considerations of the 4D MCMI system

We have seen from preceding chapters that the QD grating and grisms combination system may be utilized as key optical elements for 4D MCMI. Moreover, for practical use, there are still a few issues to consider and most of them involve a trade-off of some sort, i.e. defining a proper physical separation of the images on the camera to make the best use of the sensor chip, investigating the axial blurring induced by the varied wavelength-dependent focal lengths of non-zero diffraction orders, making the whole optical length as short as possible, and so on. Before performing the real bioimaging experiment, we will try to solve some of these problems in this section.

5.2.1 The physical separation of the multi-plane images on the camera

Due to the physical size of the camera sensor chip, we need to arrange the multi-plane (2~9) images to fit onto this chip as well as make the best use of it. Recalling Fig. 2.3 we find that the physical separation of the images on the camera only depends on a simple trigonometry determined by the diffraction angle. Based on our case of telecentric imaging (1:1 magnification of the optical system), we will consider a practical 3-plane imaging example using the real/typical parameters to calculate the image separation at the camera, and also assess the efficiency of this setup in terms of how much of the available chip it makes use of.

As mentioned before, our camera is a 2048×2048 array of 6.5μm square pixels (Andor Zyla 4.2 sCMOS), therefore the chip is $13.3 \times 13.3 mm^2$. At normal incidence, when the effective focal length of the combined achromats system is 208mm (both achromats have a focal length of 250mm and the separation between them is 200mm), the central wavelength is 525nm and the central period of QD grating is 30μm, the diffraction angle of first orders is about 1°, accordingly a centre separation of 3.64mm between the 3 images (0^{th} and $\pm 1^{st}$ orders) is achieved which should be the maximum width of each image without overlapping. Thus 3×3.64mm = 10.92mm (~82%) of the camera chip width will be occupied by these images, which presents a well-designed optical system. Moreover, since the image delivered by the microscope is very large in diameter, the images of first three diffraction orders at the camera will therefore inevitably overlap. Thus a variable slit is utilized to fit all three images on the camera side by side without overlapping as well as make the largest possible field of view in each image — the images are only just touching or the gap between them is reasonably small.

5.2.2 As compact optical path as possible

The QD grating and grisms used on their own could form no real images in the negative orders so that the selection of achromats and the design of optical path are of practical importance. In real bioimaging experiment, there are trade-offs to be made, such as how much of the camera chip is filled, the central period of QD grating, the focal length of the achromats, the overall length of the optical path and so on. Let us recall the case in last section for example: we would halve the amount of the camera if the period of the QD grating was doubled (i.e. 30μm). Surely we could increase the camera usage with a large period grating by choosing achromat with a longer focal length, but this

would then mean making the whole system longer. Since our optical system provides both telecentric imaging (thus 4*f* system) and chromatic correction, the length of the unfolded beam-path is about 4x the effective focal length of the achromats combination.

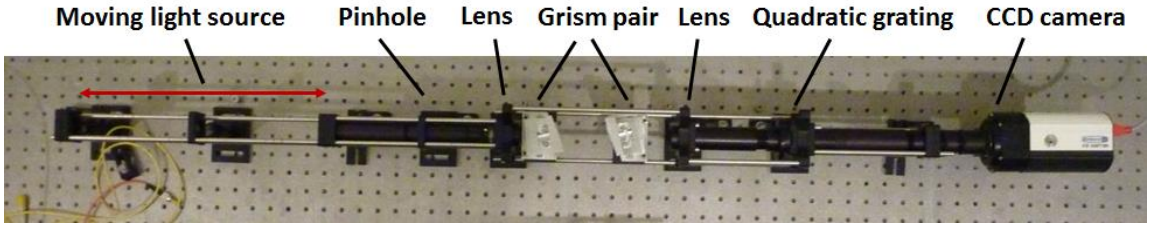

Fig. 5.1 The long optical path of QD grating and grisms based 4D imaging system we developed before [5].

Fig. 5.1 shows our previous optical design of the QD grating and grisms based 4D imaging system, which has the overall optical length of ~1.3m. Due to the long optical path, the optical system was quite unstable and thus the alignment was constantly needed, which restricted its application in the practical imaging work. Actually our preceding relay design cannot be applied to the 4D MCMI at all, although the initial optical tests worked well for chromatic correction of a single diffraction order [5-7]. As far as I could concern, to attach the optical system on microscope, the stability (thus the shorter optical path) is of the highest priority for optimization.

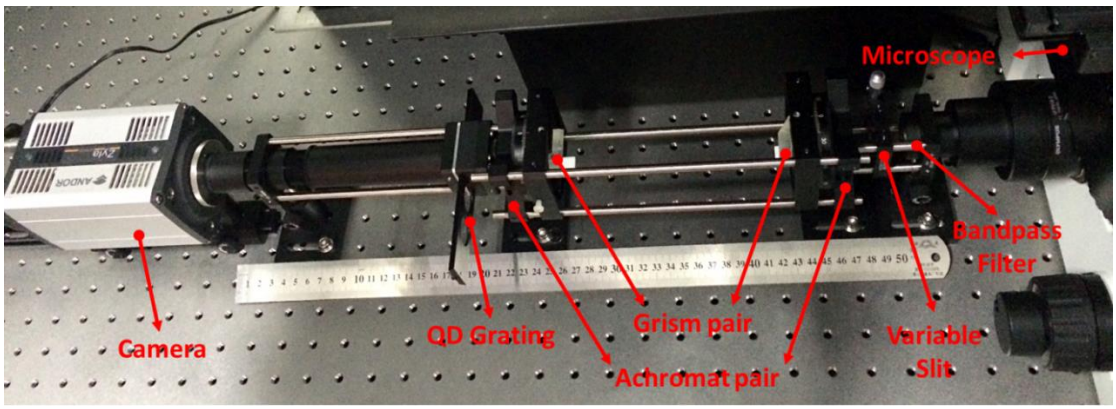

Fig. 5.2 Establishment of the QD grating and grisms based 4D MCMI system.

We are currently working towards optimizing this system. It is shown in Fig. 5.2 that our recent relay system can be attached between the microscope and camera because the overall optical path is shorten to only ~50cm, which is 2.6-fold shorter than that of previous design shown in Fig. 5.1. However, there is a compromise between the optical length and chromatic correction effect (see details in section 5.4), so that further

optimization is still required, especially the plotting design of QD grating and the selection of achromat(s). For the case that the optical length/space is very limited, we may shorten the overall length by folding the optical path between the QD grating and the camera without complicating the optical alignment.

5.2.3 Axial/Focus resolution

We have described the lateral smearing of the images induced by the wavelength dependence of the diffraction angle in subsection 2.3.2.2, and the chromatic correction using a pair of grisms has been demonstrated in Chapter 4. To fully assess the effect of bandpass on image quality, we now consider a further wavelength dependent property: the focal length of non-zero diffraction orders.

Based on the principle of QD grating illustrated in section 2.1.1, we may deduce that the distortion of the grooves adds a constant detour phase at all wavelengths, rather than a constant path length as in the case of a perfect lens, which causes the focal length of the QD grating to vary with wavelength and thus each non-zero diffraction order to image a different object plane at every wavelength. Accordingly the axial smearing occurs and the wavelength dependent focal lengths will also lead to slight magnification variations. However, unlike the lateral smearing effect, the axial smearing cannot easily be corrected and will therefore in some applications, where focus resolution is critical, a narrow bandpass filter can be used to limit the bandwidth.

Here we would like to briefly quantify this axial effect in mathematical way. It has been known that the standard coefficient of defocus W_{20} represents the constant path length added to every wavelength and can be replaced by the term $n\lambda$ where n is the number of waves of defocus introduced in the +1 diffraction order. Therefore Eq. (2.16) could be written as,

$$f_m(\lambda) = \frac{R^2}{2mn\lambda} \tag{5.1}$$

Given that the multi-plane imaging is typically achieved by combining a QD grating with achromat(s), the effective focal length of this combination will also vary as $f_m(\lambda)$ varies, which produces the axial smearing. The object distance (z) imaged in the 0^{th} order is assumed to be constant since it only depends on the achromat(s), whereas at a given wavelength the plane imaged in the m^{th} order can be calculated by,

$$d_m(\lambda) \approx -2m\left(\frac{z}{R}\right)^2 n\lambda \tag{5.2}$$

where we assume that $2mzW_{20} << R^2$. Whence, on partial differentiation we find that the spread of object planes images (Δd_m) for a given bandpass $\Delta\lambda$ could be characterized by,

$$\Delta d_m \approx \frac{\Delta\lambda}{\bar{\lambda}} d_m(\bar{\lambda}) \tag{5.3}$$

where $\bar{\lambda}$ is the mean wavelength.

According to the *Rayleigh criterion* [8, 9], *the depth of focus* (*DOF*) [8] is equivalent to a defocus error of $\lambda/4$ (i.e. $n = 1/4$). And Δd_m can be expressed as a function of DOF of the imaging system to assess the broadband image quality of the system. Hence, by substituting $n = 1/4$ into Eq. (5.2) we find that at the mean wavelength,

$$\text{DOF} \approx \left(\frac{z}{R}\right)^2 \frac{\bar{\lambda}}{2} \tag{5.4}$$

Consequently the chromatic spread of the object planes Δd_m, as a function of DOF, can be expressed as,

$$\frac{\Delta d_m}{\text{DOF}} = \frac{4mn\Delta\lambda}{\bar{\lambda}} \tag{5.5}$$

If $\Delta d_m / \text{DOF} < 1$ no degradation of the image will be seen since this is equivalent to a grating with $\Delta\lambda < \bar{\lambda}/(4n)$ for $m = 1$. Thus the positions of the in-focus image planes in 4D MCMI will change slightly.

5.3 4D MCMI tests of fluorophore

One of the principal applications for 4D MCMI should be fluorescence microscopy imaging, allowing access to the full bandwidth of the fluorophore. A simulation of chromatic correction for imaging fluorophore has been demonstrated in section 4.4 and here, in practice, we will apply the optical system to the real fluorophore microscopy imaging tests.

5.3.1 Preparation of fluorophore sample

Preparing samples for QD grating and grisms based fluorescence microscopy demands cleanliness and an appropriate thickness of the sample, which ensure a clear imaging background and adequate space for z-plane separations respectively. Therefore a very clean and flat coverslip, and a transparent carrier medium which could be evenly mixed with fluorescent beads and quickly get solidified to form a desired thickness are the key points to sample preparation.

The coverslips (BRAND, 470820), which should be standardly cleaned based on the previously reported procedure [10], were treated with acetone and 1M NaOH solution successively. Each treatment was performed in an ultrasonicator for half hour, followed by thoroughly rinsing with deionized water for several times (>2, sonicate when necessary). These clean coverslips were then dried with nitrogen. As to the carrier material, Polyvinyl Acetate (PVA, 81381 Sigma-Aldrich) was chosen due to its good viscosity and optical properties [11]. 30% PVA aqueous solution was prepared using standard method [12] by dissolving the powder in water heated to about 100 ℃ under stirring. Next the 1:10 diluted suspension of fluorescence microspheres (Invitrogen, F8827, 2 μm, 505/515) was mixed with PVA solution with a ratio of 1:10, along with repeated sonicate, 70 ℃ water bath and vortex mixture which allowed few beads clustering and sufficient mixing of beads and PVA solution. Finally the well-dispersed fluorescent beads with PVA solution were gently dipped onto the cleaned coverslips (~100 μl per sample, spin coating would be applied if an accurate thickness was required) and left in the 45 ℃ oven for a few minutes for drying. With a quick check by microscope, we saw that the fluorescence microspheres were monodispersed and quasi-stochastic uniformly immobilized in PVA gel. The samples were kept in dark place to avoid photolysis (although it rarely happened) for further experiments.

YF acknowledges Dr. Jianli Liu and Mr. Hefei Ruan of Institue of Chemistry, Chinese Academy of Sciences, for the assistance of sample preparation.

5.3.2 Optical setup

Imaging experiments were carried out on an Olympus IX73 microscope setup (100x oil-immersion objective) that was configured to simultaneously image 3 object planes on to a single image plane with chromatic correction (similar with Fig. 4.11). This was achieved by placing the QD grating at Fourier plane of lens system, but the absolute

positions of grisms are not strictly defined. Based on the optical parameters applied in section 4.4, the relay design of this 4D MCMI system is demonstrated in Fig. 5.3, where the fluorophore sample was excited by a laser source with wavelength 473nm and a bandpass filter (Thorlabs, FB550-40) was also implemented to generate a certain spectrum for accurate calculation of grism separation, see Fig. 5.4 for details.. Again in this case the separation between the object planes (Δz) is 2.3μm. Note that after the grism only the on-axis rays (solid) are shown and the green broken lines illustrates the ray paths and position of focus (0^{th} order) if no grisms are used.

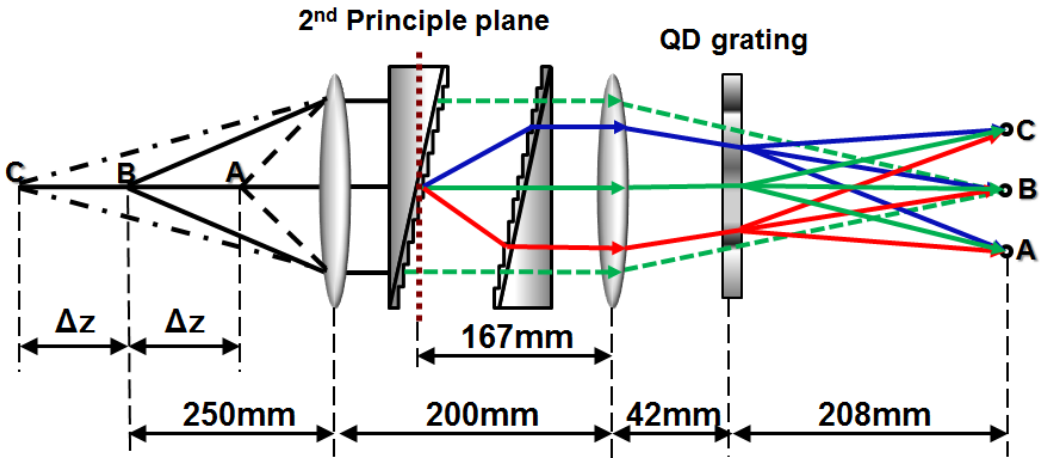

Fig. 5.3 Schematic of the relay design of 4D MCMI system.

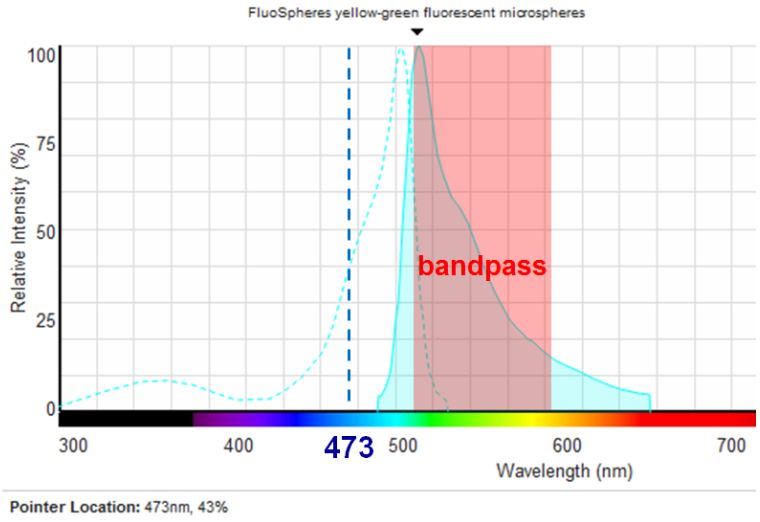

Fig. 5.4 Spectra of fluorescent microspheres [13].

In Fig. 5.4, the dashed and solid green lines represent the excitation and emission plots, respectively.

5.3.3 4D MCMI tests of fluorescence microspheres

The images were captured by the sCMOS camera (Andor Zyla 4.2) with the exposure time of 50ms and then were processed by the software Fiji-ImageJ [14]. The images of the first three orders before and after chromatic correction have been shown in Fig. 5.5.

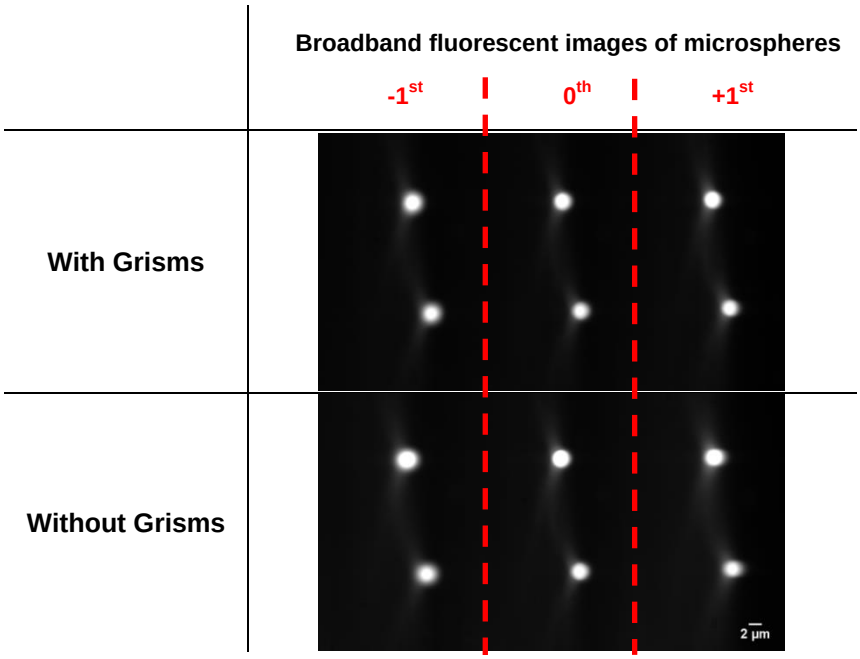

Fig. 5.5 4D multi-colour images of fluorescence microspheres with/without grism correction.

From Fig. 5.5 we see that the chromatic smearing of first diffraction orders has been effectively corrected using grism pairs. The simultaneous use of multiple fluorophores to facilitate studies of the interactions between cellular components is important in many biological studies and the results obtained permit us to assess the use of the system described for 4D MCMI. Using a dual QD grating system (each etched for a different wavelength), a single grism pair and a dichroic mirror between the QD grating and camera, allows one to form multifocus images simultaneously on two separate monochrome cameras. If the dichroic directs emission from a short wavelength emission fluorophore to one camera and the other camera sees a long wavelength fluorophore, these fluorophores can both be imaged separately but simultaneously in 3D on the two cameras. A third fluorophore at a central wavelength can be chosen such that the light from this fluorophore is detected in 3D on both cameras. The coincident images on the two cameras are clearly due to the mid-wavelength fluorophore and, once these coincidences have been established, the remaining images on each camera can be assigned to the appropriate long or short wavelength fluorophore. Since each

fluorophore is thus imaged simultaneously in 3D, it is possible to study dynamic interactions between three different cellular components in 3D with accurate chromatic correction.

5.4 4D MCMI tests of cells engulfing fluorescent beads

As demonstrated in last section, we have successfully recorded the 4D multi-colour images of fluorescent beads on the coverslip. Here we apply this optical set to a sophisticated biological system — cells engulfing fluorescent beads.

5.4.1 Cell culture and uptake fluorescent beads

MCF-7 cells were cultured in DMEM (Hyclone, U.S.A.) containing 10% fetal bovine serum (Hyclone, U.S.A.) in a humidified 5% CO_2 atmosphere at 37℃. Cells growing in a 35mm glass-bottom dish (Shengyou Biotechnology) were incubated with fluorescent beads (10μM, Invitrogen, F8813, 500nm, 505/515) for 5h and washed with PBS buffer to remove the non-internalized nanoparticles. Then the cells were fixed with 4% paraformaldehyde for 30min at 4℃. The cells were rinsed several times with PBS buffer and incubated in fresh medium, and then imaged by our optical system.

5.4.2 Optical setup

To demonstrate, bright field imaging is applied to capture the structure of MCF-7 cells, whereas the beads are observed from the fluorescence imaging channel. The optical setup keeps almost the same with that of the fluorescent beads imaging as illustrated in Fig. 5.3 (except replacing a QD grating with a smaller central period and a bandpass filter), . For clarity, here we recall some key parameters of the optical design, as shown in Table 5.1.

Table 5.1 Key parameters of 4D MCMI of MCF-7 cells.

Parameter	*Value*
Radius of QD grating (R)	**10mm**
Central Period of QD grating (d_0)	**30μm**
Defocus (W_{20})	**50λ**
Central wavelength (λ)	**525nm**
Wavelength range ($\Delta\lambda$)	**78nm**
Magnification of objective (M)	**100x**
Pixel size of camera (Andor Zyla 4.2 sCMOS)	**6.5μm**
Size of camera chip (Andor Zyla 4.2 sCMOS)	**13.3×13.3mm^2**
Focal length of achromatic lens (f)	**250mm**
Separation between achromats	**200mm**
Effective focal length of lens pair (f_{eff})	**208mm**
Separation between object planes (Δz)	**2.3μm**
Focal length of QD grating_ $\pm1^{st}$ order @ 525nm (f_g)	**±1905mm**
Grism separation (d)	**152mm**

Note that the wavelength range ($\Delta\lambda$) of 78nm is achieved by a bandpass filter (Thorlabs, MF525-39); see Fig. 5.4 for the spectra of fluorescent microspheres. Besides the issues we have discussed in previous sections, some trade-offs among the parameters above have been made to minimise the overall length of the optical path. In principle the chromatic smearing induced by the waveband of 78nm should be corrected when the grism separation is 176mm. However, due to the size of optical mounts, the maximum grism separation can only be 152mm. As discussed in section 5.2.2, achieving a compact optical path is of the highest priority. Therefore the effect of chromatic correction has been compromised in this case.

5.4.3 Results and problems

Both the bright field and fluorescence multi-plane images of MCF-7 cells engulfing fluorescent beads were recorded, which was illuminated/excited by 520nm LED and 473nm laser through objective, respectively.

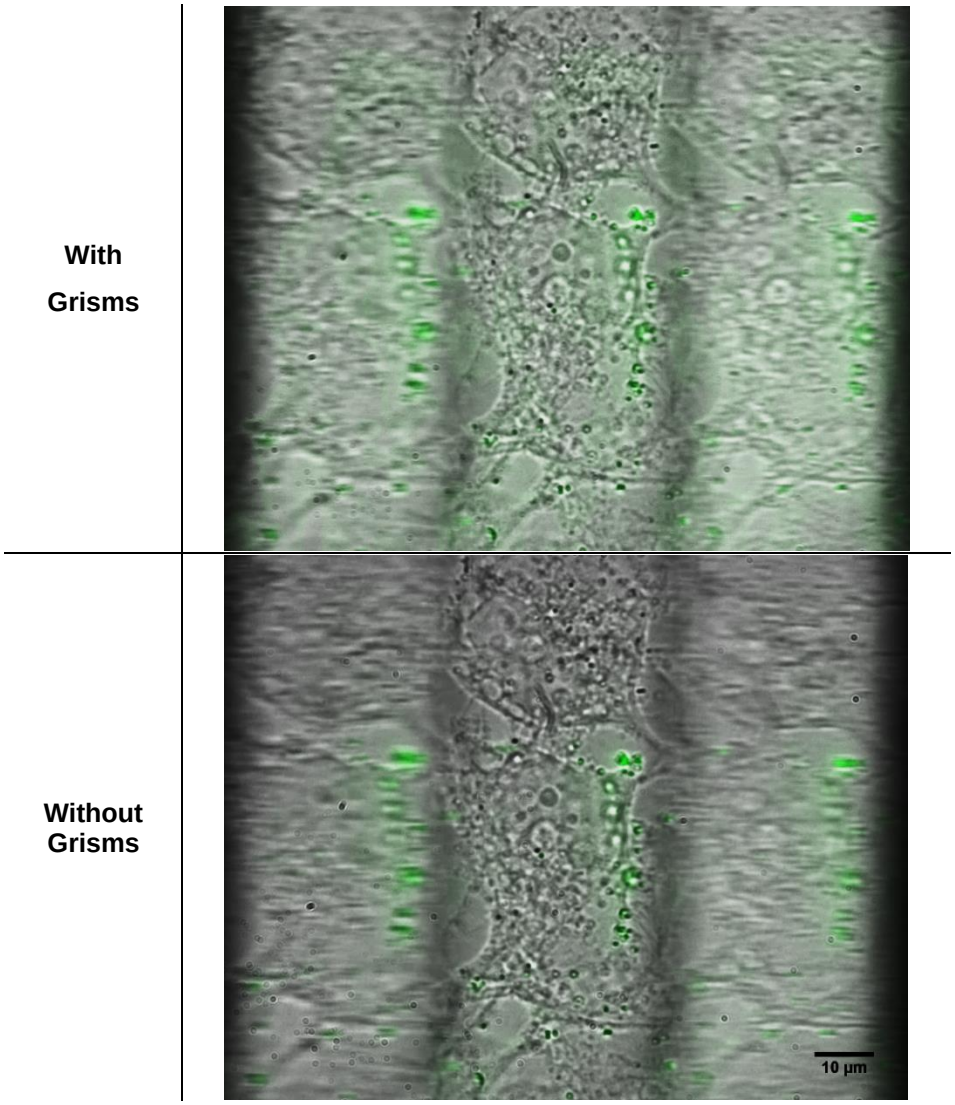

Fig. 5.6 Composite images of bright field and fluorescence multi-plane imaging of MCF-7 cells engulfing fluorescent beads, with and without grism correction.

Fig. 5.6 shows the composite images of MCF-7 cells with and without chromatic correction, in which the green dots are the fluorescent beads. From both the bright field and fluorescence multi-plane images we see that the image quality has been improved when grisms are implemented. The results are so positive that the chromatic smearing should be further minimized if the theoretical grism separation of 176mm was applied — in principle only 67nm bandwidth of smearing could be corrected using the current grism separation of 152mm.

Another problem in Fig. 5.6 is that the images of non-zero orders seem not in focus. It might be because that the separation between object planes (Δz = 2.3μm) is larger than the axial size of the cell. To obtain guidance for further optical design, we tried a few cells for bioimaging tests and one of which looked a bit clear, as the bright field and fluorescence multi-plane imaging of HeLa cells shown in Fig. 5.7 (the optical parameters were exactly same with that shown in Table 5.1). Here the biosample preparation is similar with the process illustrated in section 5.4.1.

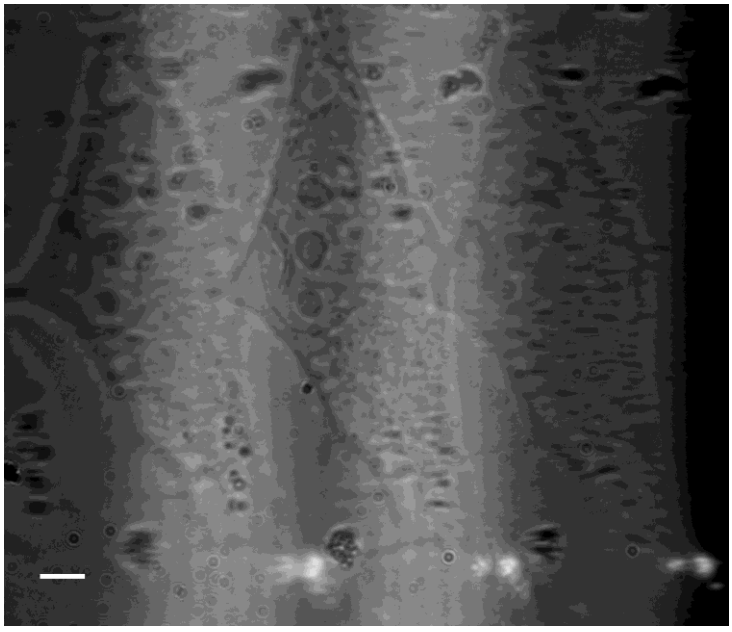

Fig. 5.7 Multi-plane images of HeLa cells engulfing fluorescent beads. Scale bar: 5μm.

From Fig. 5.7 we can see clearly the profile of both the whole cell and some organelles in multiple object planes, especially the cell nuclei. But unfortunately these cells did not uptake the fluorescent beads successfully (see the bright dots at the right bottom of each image).

After quite a few imperfect bioimaging tests, we have been trying all our best to optimize the optical relay system, especially minimising the size of grism mounts. And the bright field imaging of HeLa cells without fluorescent beads was performed again, by optimizing the grism separation to the theoretical value of 176mm rather than the earlier value of 152mm (other parameters were same with that shown in Table 5.1). As demonstrated in Fig. 5.8, the three images appear to be significant different and the shape/size of cell in non-zero order images look undistorted and well in-focus.

Therefore at this stage we would say that these initial bioimaging experiments have been the solid proof of our optical principles and thus our imaging technique.

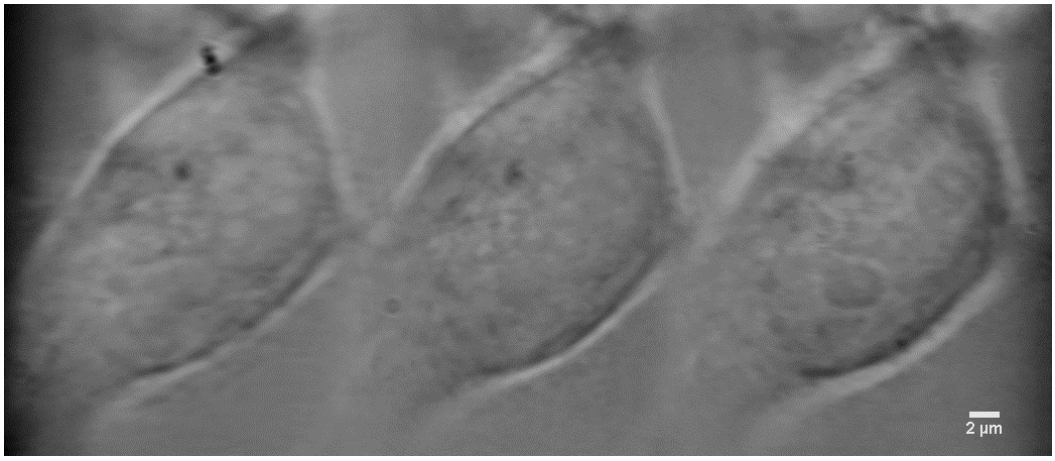

Fig. 5.8 Bright field 4D images of of HeLa cells. The separation between each in-focus image plane (Δz) is 2.3µm and the bandwidth is 525±39nm.

We have been concentrating on improving the performance of 4D MCMI system and will explore a 'balance' of all the parameters, including the plotting parameters of QD grating, new design of grism and its mount and, of course, the overall optical path. At the same time, we are also working to optimize the 4D MCMI technique for real biological applications.

YF acknowledges Dr. Jianli Liu of Institue of Chemistry, Chinese Academy of Sciences, for the biosample preparation.

5.5 Current and future work

We are fortunate to have collaborations and interactions with several biology research groups and thus quite a few promising biological systems are of the potential applications. Two of the hottest topics are the investigation of Transforming growth factor-β (TGF-β) II containing vesicles [15], as well as the TGF-β receptor endocytic trafficking [16].

TGF β is a member of the structurally related growth factor family, which plays key roles in regulating a wide range of biological responses such as cell proliferation, differentiation, motility and apoptosis [17, 18]. Disregulation of their signal transduction is related to several human diseases such as cancer and tissue fibrosis [19,

20]. TGF-β signalling is initiated by ligand binding to receptors (type I and type II). TGF-β type II receptor (TβRII) is the primary receptor for ligand binding. Generally, TβRII molecules are synthesized in endoplasmic reticulum (ER) [21, 22], most of them get highly phosphorylated, then 90% of the receptors undergo further modifications in the Golgi apparatus before being transported to the cell surface [23, 24], but little cognition about transport process can be obtained at this stage. Most of TβRII-containing vesicles (TCVs) were experiencing post-Golgi transportation and only a few were internalized from the plasma membrane through endocytosis [15]. Therefore, it is still unclear how these two processes are related at present, and there might be something we could explore using our 4D MCMI system.

We previously applied total internal reflection fluorescence microscopy (TIRFM) [25] and quasi-TIRFM alternately imaging modes to investigate the intracellular transport of GFP-tagged TβRII after its biosynthesis from trans Golgi network (TGN) to the cell surface [26]. In TIRFM mode, the incident angle of the excitation light (θ_e) is equal or larger than the critical angle (θ_c), and an evanescent field was produced at the interface between the glass substrate and cell medium. This evanescent field with a penetration depth of less than 160nm from the plasma membrane was used for fluorescence excitation. Only TβRII-GFP molecules on or close to the plasma membrane were imaged. However, Quasi-TIRFM, one variant of TIRFM, extends the probing depth to the cytoplasm. In this mode, θ_e is smaller than θ_c, but much larger than that in the normal epi-mode (where $\theta_e = 0$), intracellular TβRII-GFP molecules which are more than 160nm away from the membrane could be detected with adequate imaging contrast. Through shifting between TIRF and quasi-TIRF, the process of TCVs transporting from TGN to the cell surface were captured respectively [15]. However, it would be much more convenient to monitor the relative distribution of TCVs both in the cytoplasm and regions close to the cell membrane at the same time by 4D microscopy.

Endocytosis and intracellular sorting of TGF-β receptors play an important role in TGF-β signalling [27]. Previous studies have shown that internalization of TGF-β receptors at the plasma membrane is mainly mediated by two independent endocytic pathways, clathrin- and caveolae-mediated endocytosis [28, 29]. These indirect conclusions based on TGF-β receptors colocalized with related proteins in clathrin- and caveolae-mediated endocytosis pathways [30, 31]. We have recently found that the

clathrin- and caveolae-mediated endocytic pathways can converge during TGF-β receptor endocytic trafficking in the cytoplasm by using a combined approach of live-cell fluorescence microscopy, electron microscopy and biochemical methods. By tracking the intracellular dynamics of fluorescently-labeled TGF-β type I receptor (TβRI), we found that after mediating TβRI internalization, certain clathrin-coated vesicles and caveolar vesicles are fused underneath the plasma membrane, forming a novel type of caveolin-1 and clathrin double-positive vesicles. Under the regulation of Rab5, the fused vesicles are targeted to early endosomes and thus deliver the internalized TβRI to the caveolin-1 and EEA1 double-positive early endosomes (caveolin-1-positive early endosomes). We further found that the caveolin-1-positive early endosomes are positive for Smad3/SARA, Rab11 and Smad7/Smurf2, and may act as a multifunctional device for TGF-β signaling and TGF-β receptor recycling and degradation, although deeper investigation would be required to explore whether the caveolin-1-positive early endosome is a multifunctional organelle for the other internalized receptors. Consequently, these findings uncover a novel scenario of endocytosis, which is the direct fusion of clathrin-coated and caveolae vesicles during TGF-β receptor endocytic trafficking [16]. However, given that both the detailed dynamics of each protein in the membrane of early endosomes and the role of clathrin and caveolae in TGF-β receptor endocytosis are still unclear, we are endeavouring to establish a 4D MCMI system to directly monitor the TGF-β receptor internalization via either clathrin or caveolae.

YF acknowledges Dr. Jianli Liu of Institue of Chemistry, Chinese Academy of Sciences, for the manuscript preparation of this section.

5.6 References

[1] Y. Jiang, C. Zhu, L. Ling, L. Wan, X. Fang and C. Bai, *Specific aptamer-protein interaction studied by atomic force microscopy*. Analytical Chemistry **75**(9), 2112-2116 (2003).

[2] X. S. Xie and J. K. Trautman, *Optical studies of single molecules at room temperature*. Annual Review of Physical Chemistry **49**, 441-480 (1998).

[3] J. B. Pawley, *Handbook of biological confocal microscopy*. Springer US, New York, (2006).

[4] P. M. Blanchard and A. H. Greenaway, *Simultaneous multiplane imaging with a distorted diffraction grating*. Applied Optics **38**(32), 6692-6699 (1999).

[5] Y. Feng, *Optimization of phase gratings with applications to 3D microscopy imaging*, A dissertation for the degree of Doctor of Philosophy, Precision Instruments and Machinery, University of Science and Technology of China, Hefei, China (2013).

[6] Y. Feng, P. A. Dalgarno, D. Lee, Y. Yang, R. R. Thomson and A. H. Greenaway, *Chromatically-corrected, high-efficiency, multi-colour, multi-plane 3D imaging*. Optics Express **20**(18), 20705-20714 (2012).

[7] Y. Feng, P. A. Dalgarno, D. Lee, A. H. Greenaway, Y. Yang and R. R. Thomson, *Optical system*. in UK Intellectual Property Office. UK Patent Application No. GB2504188-A, (Marks & Clerk LLP Edinburgh Office, United Kingdom, 2013).

[8] M. Born and E. Wolf, *Principles of optics*. Cambridge University Press, Cambridge, Corrected reprint of the 7th edition, (2001).

[9] E. Hecht, *Optics*. Pearson Education, Addison Wesley, San Francisco, 4th edition (International edition), (2002).

[10] J. Yu, *Multifunctional imaging system based on super-resolution fluorescence microscopy*, A dissertation for the degree of Doctor of Philosophy, Institue of Chemistry, University of Chinese Academy of Sciences, Beijing, China (2015).

[11] R. Luchowski, Z. Gryczynski, Z. Földes-Papp, A. Chang, J. Borejdo, P. Sarkar and I. Gryczynski, *Polarized fluorescent nanospheres*. Optics Express **18**(5), 4289-4299 (2010).

[12] R. Luchowski, P. Sarkar, S. Bharill, G. Laczko, J. Borejdo, Z. Gryczynski and I. Gryczynski, *Fluorescence polarization standard for near infrared spectroscopy and microscopy*. Applied Optics **47**(33), 6257-6265 (2008).

[13] ThermoFisher, https://www.thermofisher.com/cn/zh/home/life-science/cell-analysis/labeling-chemistry/fluorescence-spectraviewer.html?ICID=svtool&UID=8811h2o, Access date: 02 November, 2015.

[14] M. D. Abramoff, P. J. Magelhaes and S. J. Ram, *Image Processing with ImageJ*. Biophotonics Intl **11**(5-6), 36-42 (2003).

[15] W. Luo, T. Xia, X. Li, Y. G. Chen and X. Fang, *Visualization of the post‐Golgi vesicle‐mediated transportation of TGF‐β receptor II by quasi‐TIRFM*. Journal of Biophotonics **7**(10), 788-798 (2014).

[16] K. He, X. Yan, N. Li, S. Dang, L. Xu, B. Zhao, Z. Li, Z. Lv, X. Fang and Y. Zhang, *Internalization of the TGF-β type I receptor into caveolin-1 and EEA1 double-positive early endosomes*. Cell Research **25**(6), (2015).

[17] K. Jong Seok, L. Cheng and D. Rik, *New regulatory mechanisms of TGF-beta receptor function*. Trends in Cell Biology **19**(8), 385-394 (2009).

[18] Y.-G. Chen, *Endocytic regulation of TGF-β signaling*. Cell Research **19**(1), 58-70 (2009).

[19] J. Massagué, *TGFbeta in Cancer*. Cell **134**(2), 215-230 (2008).

[20] I. Hiroaki and M. Kohei, *TGFbeta signalling: a complex web in cancer progression*. Nature Reviews Cancer **10**(6), 415-424 (2010).

[21] H. Y. Lin, X. F. Wang, E. Ng-Eaton, R. A. Weinberg and H. F. Lodish, *Expression cloning of the TGF-beta type II receptor, a functional transmembrane serine/threonine kinase*. Cell **68**(4), 775-785 (1992).

[22] K. Luo, . and H. F. Lodish, *Positive and negative regulation of type II TGF‐β receptor signal transduction by autophosphorylation on multiple serine residues*. Embo Journal **16**(8), 1970-1981 (1997).

[23] K. M. Koli and C. L. Arteaga, *Processing of the transforming growth factor beta type I and II receptors. Biosynthesis and ligand-induced regulation*. Journal of Biological Chemistry **272**(10), 6423-6427 (1997).

[24] R. G. Wells, H. Yankelev, H. Y. Lin and H. F. Lodish, *Biosynthesis of the Type I and Type II TGF-β Receptors*. Journal of Biological Chemistry **272**, 11444-11451 (1997).

[25] Y. Sako and S. Minoghchi, T, *Single-molecule imaging of EGFR signalling on the surface of living cells*. Nature Cell Biology **2**(3), 168-172 (2000).
[26] W. Zhang, Y. Jiang, Q. Wang, X. Ma, Z. Xiao, W. Zuo, X. Fang and Y. G. Chen, *Single-molecule imaging reveals transforming growth factor-β-induced type II receptor dimerization*. Proceedings of the National Academy of Sciences **106**(37), 15679-15683 (2009).
[27] A. Rubén Claudio and W. Beverly, *Endocytosis of membrane receptors: two pathways are better than one*. Proceedings of the National Academy of Sciences of the United States of America **102**(8), 2679-2680 (2005).
[28] H. Mitchell, A. Choudhury, R. E. Pagano and E. B. Leof, *Ligand-dependent and -independent transforming growth factor-beta receptor recycling regulated by clathrin-mediated endocytosis and Rab11*. Molecular Biology of the Cell **15**(9), : 4166–4178. (2004).
[29] H. Susan, C. Anil and C. Silvia, *TGF beta receptor internalization into EEA1-enriched early endosomes: role in signaling to Smad2*. Journal of Cell Biology **158**(7), 1239–1249 (2002).
[30] C. E. Runyan, S. H William and P. Anne-Christine, *The role of internalization in transforming growth factor beta1-induced Smad2 association with Smad anchor for receptor activation (SARA) and Smad2-dependent signaling in human mesangial cells*. Journal of Biological Chemistry **280**(9), 8300-8308 (2005).
[31] R. A. Anders, S. L. Arline, J. J. Doré and E. B. Leof, *Distinct endocytic responses of heteromeric and homomeric transforming growth factor beta receptors*. Molecular Biology of the Cell **8**(11), 2133-2143 (1997).

Chapter 6

Conclusions and future work

This dissertation is mainly constructed in three sections that tackle in turn the mathematical modelling of 2D QD grating, chromatic correction using a pair of grisms and bioimaging tests, offering a complete view of the current research state of QD grating and grisms based 4D MCMI technique.

The motivation for this work is to design a high temporal resolution microscopy imaging technique with which two to nine focal planes can be imaged simultaneously. This is achieved by the combination of key optical elements QD grating [1] and grisms [2, 3] and by attaching this imaging setup to a commercial microscope for biological applications. To fully develop the effectiveness of this approach to 4D imaging in biological systems and further applied to 4D particle localization, a series of optimizations have been performed including establishing the 2D mathematical model of QD grating for optimizing the light efficiency [4] and the working phase, and a specially designed chromatic correction module using a combination of customized prism and blazed grating (thus grism). Some initial bioimaging experiments have proved that this novel imaging technology works well and is capable of recording the biological process, especially the fast changing objects in living cells.

One of the prime reasons for developing our imaging system was to implement a simple chromatic correction that would allow us to make effective use of the full fluorophore bandwidth and, for that reason, the optical efficiency of the grism system is of significant interest. For application in 4D live-cell microscopy of fluorescently-tagged live cells, where the sources are intrinsically faint and the photon flux may be limited by the inherent photophysics (bleaching, blinking and cyto-toxicity), achieving the highest total optical throughput is very important. High optical efficiency is further crucial in our application, where the need to re-collimate the dispersed beam dictates the use of two identical grisms. With the experimental measurement using power meter (Thorlabs) the optical efficiency of ~70% is achievable with the grisms used here,

which provides substantial overall flux gains. Without chromatic correction 4D imaging is restricted to, typically, a 10nm collection bandpass, whereas with grism correction the full fluorophore range can be accessed, giving a significant increase in collected flux levels.

In conclusion we have demonstrated the use of a simple, linear, grism (grating and prism) pair to remove chromatic smearing in QD grating based 4D imaging application without compromising image quality. With the addition of two relay lenses, the imaging system can easily be appended to the camera port of many commercial microscopes. The initial bioimaging experiments demonstrate that the 4D MCMI system is practicable to perform simultaneous imaging of living cells.

Future modifications can easily optimize performance and operation. The present mathematical model of our 2D QD grating has included only the basic principles of analytical model and numerical computation of 2D QD grating. Both the theory and algorithm can be extended to more complicated cases, i.e. crossed QD grating for 9-plane imaging and combination of QD grating and lens/grisms system. In more considerations, the chromatic aberration is one of the most remarkable and useful properties of QD grating, so that the evaluation of the dispersion of both single and crossed QD phase gratings will also be investigated. Further explorations are still in process and an adequate discussion may be published later.

As to the chromatic correction, in a custom system the grism pair can be optimized for ideal on axis throughout at a chosen wavelength, typically the central of the input bandwidth. In practical terms the angular controls required within the grism system are independent of grism separation and can be locked when the system is constructed. The grism separations can be easily controlled by a simple motor driven translation in future systems. The grism orientation used in all of these experiments and designs was such that the prism faces were outermost in the grism pair. Reversing this arrangement so that the blazed grating are outermost offers further control possibilities, in that the interior prism faces in such an arrangement provide some additional chromatic control through the refraction of all but the un-deviated wavelength. A ray-tracing study shows that this arrangement offers slightly better linearity in the dispersion. A further possibility is the use of two grisms of slightly-different design, rather than a pair of (nominally) identical grisms back to back as described here. Such an arrangement

would permit the images on the camera to be separated chromatically, for example if different colour fluorophores are required.

6.1 References

[1] P. M. Blanchard and A. H. Greenaway, *Simultaneous multiplane imaging with a distorted diffraction grating*. Applied Optics **38**(32), 6692-6699 (1999).

[2] Y. Feng, P. A. Dalgarno, D. Lee, A. H. Greenaway, Y. Yang and R. R. Thomson, *Optical system*. in UK Intellectual Property Office. UK Patent Application No. GB2504188-A, (Marks & Clerk LLP Edinburgh Office, United Kingdom, 2013).

[3] Y. Feng, P. A. Dalgarno, D. Lee, Y. Yang, R. R. Thomson and A. H. Greenaway, *Chromatically-corrected, high-efficiency, multi-colour, multi-plane 3D imaging*. Optics Express **20**(18), 20705-20714 (2012).

[4] Y. Feng, *Optimization of phase gratings with applications to 3D microscopy imaging*, A dissertation for the degree of Doctor of Philosophy, Precision Instruments and Machinery, University of Science and Technology of China, Hefei, China (2013).